SECURITY CLASSIFICATION OF THIS PAGE

REPORT DOCUMENTATION

AD-A240 731

Approved
OMB No. 0704-0188

DTIC ELECTE SEP 25 1991 S D

1a. REPORT SECURITY CLASSIFICATION
Unclassified

1b.

2a. SECURITY CLASSIFICATION AUTHORITY
N/A

3. DISTRIBUTION/AVAILABILITY OF REPORT
This document has been approved for public release and sale; its distribution is unlimited.

2b. DECLASSIFICATION/DOWNGRADING SCHEDULE
N/A

4. PERFORMING ORGANIZATION REPORT NUMBER(S)
CRY002 A

5. MONITORING ORGANIZATION REPORT NUMBER(S)

6a. NAME OF PERFORMING ORGANIZATION
Crystallume

6b. OFFICE SYMBOL (If applicable)

7a. NAME OF MONITORING ORGANIZATION
Naval Research Laboratories

6c. ADDRESS (City, State, and ZIP Code)
125 Constitution Drive
Menlo Park, CA 94025

7b. ADDRESS (City, State, and ZIP Code)
4555 Overlook Avenue, SW
Washington D.C. 20375-5000

8a. NAME OF FUNDING/SPONSORING ORGANIZATION
DCASMA

8b. OFFICE SYMBOL (If applicable)

9. PROCUREMENT INSTRUMENT IDENTIFICATION NUMBER

8c. ADDRESS (City, State, and ZIP Code)
1250 Bayhill Drive
San Bruno, CA 94066-3077

10. SOURCE OF FUNDING NUMBERS

PROGRAM ELEMENT NO.	PROJECT NO.	TASK NO	WORK UNIT ACCESSION NO.

11. TITLE (Include Security Classification)
Diamond Membranes for X-ray Lithography Masks

12. PERSONAL AUTHOR(S)
William Phillips

13a. TYPE OF REPORT	13b. TIME COVERED	14. DATE OF REPORT (Year, Month, Day)	15. PAGE COUNT
Final Report	FROM _____ TO _____	7/30/91	90

16. SUPPLEMENTARY NOTATION

17. COSATI CODES			18. SUBJECT TERMS (Continue on reverse if necessary and identify by block number)
FIELD	GROUP	SUB-GROUP	

19. ABSTRACT (Continue on reverse if necessary and identify by block number)

In Phase 2 of this program we improved and refined the microwave plasma process for fabricating diamond membranes for X-ray lithography masks. Nucleation procedures were developed to eliminate uncertainty in membrane growth initial conditions. Deposition uniformity improvements were made which allowed us to produce 36 mm membrane diameters routinely. Process conditions affecting tensile stress, grain size and optical properties were explored and high quality membranes obtained reproducibly. Conditions having the potential to produce significant improvements in membrane characterisitics were identified for future investigation. Membranes produced in this program were characterized in terms of Raman spectrum, grain size, optical absorption, tensile stress, and X-ray absorption. X-ray damage studies were performed which indicated that an accumulated dose of 20 MJ/cm^3, the limit of the test, would not injure the membranes.

91-08017

20. DISTRIBUTION/AVAILABILITY OF ABSTRACT	21. ABSTRACT SECURITY CLASSIFICATION	
☐ UNCLASSIFIED/UNLIMITED ☐ SAME AS RPT ☐ DTIC USERS		
22a. NAME OF RESPONSIBLE INDIVIDUAL	22b. TELEPHONE (Include Area Code)	22c. OFFICE SYMBOL

DD Form 1473, JUN 86 Previous editions are obsolete. SECURITY CLASSIFICATION OF THIS PAGE

Phase II Final Report

Diamond Membranes for X-Ray Lithography Masks

Contract # N0001-89-C2256

Original contains color plates: All DTIC reproductions will be in black and white

July 18, 1991

Statement A and no proprietary information
per telecon James Butler
NRL/Code 6174
Washington, DC 20375-5000
NWW 9/24/91

Crystallume
125 Constitution Drive
Menlo Park, California 94025
(415) 324 9681

PHASE II FINAL REPORT
CONTRACT # N00014-89-C-2256
DIAMOND MEMBRANES FOR X-RAY LITHOGRAPHY MASKS

TABLE OF CONTENTS

1.0 PROGRAM OVERVIEW

1.1 INTRODUCTION

This report covers work performed in Phase 2 of a three phase DARPA-sponsored program to develop diamond membranes for use as x-ray lithography masks. The first phase of the program started in September 1989. X-ray lithography and diamond membrane technology have both developed considerably in the subsequent interval. The demands of x-ray lithography as a commercial process have been clarified, and simultaneously basic protocols for producing diamond membranes meeting the requirements of x-ray masks have been established. Crystallume is now in Phase 3 of the program, during which we hope to bring the development of diamond membranes meeting the needs of x-ray lithography close to completion.

Phase 2 of this program began in March 1990 and ran for nine months. This report describes the experimental work performed during Phase 2, and discusses the remaining questions that have to be addressed in order to establish diamond films as the material of choice for x-ray lithography masks. Before we begin, we will briefly summarize the main accomplishments of the Phase 1 program.

1.2 WHERE THINGS STOOD AT THE END OF PHASE 1:

By the end of Phase 1 it was clear that diamond films could be grown on silicon substrates in a state of tension. The two stage nucleation/growth approach was developed allowing these two processes to be optimized independently. It was demonstrated that the absorption and scattering properties of the films could be controlled by manipulation of the process conditions. Membranes 30 mm in diameter could be fabricated.

The problems remaining to be solved at the end of Phase 1 were as follows:

- Film growth was not reproducible. Seemingly identical process conditions did not produce films with the same characteristics.

• The films were not of uniform thickness or color. They were thicker, darker and more highly scattering in the center than at the edges.

• Scattering and optical absorption were unacceptably high.

• Membrane diameter of 30 mm was too small for mask configurations of interest.

• The goals of Phase 2 were developed to carry on from this point and to develop characterization of the membranes. These goals are enumerated below:

1.3 PHASE II GOALS

The stated goals of the Phase II program were to:

1. Examine deposition chemistry and techniques tp achieve uniform films over a 30 mm membrane diameter.

2. Modify process parameters to enhance surface smoothness and optical transparency.

3. Fabricate 30 mm membranes and attempt to fabricate 50 mm membranes.

4. Perform measurements of stress, optical transmission, surface roughness, X-ray transmission. Obtain and X-ray absorption map of a membrane.

5. Evaluate absorber compatibility.

1.4 PHASE 2 APPROACH

At the beginning of Phase 2 the approach we followed consisted of explorations of process conditions, gas mixture, seeding technique, and their effect on membrane characteristics. This work permitted us to sharpen our focus on those variables that could be controlled reliably and seemed to have the most influence on the important membrane characteristics.

In the second half of Phase 2 we were able to concentrate our resources on the most important and controllable process variables and systematically explore their effect on the membranes.

2.0 MEMBRANE GROWTH AND FABRICATION

2.1 SEEDING

The growth of CVD diamond films on a substrate occurs in two stages. At first individual nuclei form and grow larger on the substrate surface. Eventually the nuclei coalesce so that the substrate surface is no longer exposed, and the film continues to accrue thickness by deposition of diamond on diamond until growth is ended. We found in Phase I that there are many benefits to using different reactor conditions for the nucleation and growth portions of this cycle. Conditions encouraging a high density of nucleation on the substrate surface can be used in the initial stage while the substrate surface is exposed. High nucleation density sets the stage for subsequent film growth with small grain size. Nucleation conditions have to be discontinued once the surface is completely covered with diamond because they lead to films that are not particularly useful for x-ray lithography membranes. Conditions encouraging formation of films with optimal parameters should instead be used for subsequent growth. A major portion of the work in Phase 2 was devoted to defining these parameters and optimizing the conditions of the growth phase.

The nucleation of diamond films on silicon usually requires seeding the silicon wafer before growth is started. This step is a necessity in microwave deposition because nucleation of diamond won't take place without it. Seeding is most often accomplished by scratching or polishing the wafer with diamond abrasive. Early in the program the favored technique was to apply diamond abrasive slurry to a soft paper lap, and move the wafer around on the lap in the classic figure eight polishing motion. Under other circumstances this action would produce polishing, but the as-received silicon wafers have a nearly perfect polish to begin with, and this polish is degraded by the diamond abrasive in the seeding procedure.

Other diamond researchers have utilized different seeding techniques. To determine if a change of technique would produce different or better results in the final film, we evaluated several alternative seeding approaches. We designed a simple experimental procedure to facilitate comparisons among different approaches:

a. Testing procedure. Our testing procedure was to prepare two Si wafers for comparison by two different seeding methods. The wafers were then cleaved into half circles. Mating halves from each wafer were mounted side by side in the reactor, and a diamond nucleation layer (to be defined in the next section) was grown on the two halves simultaneously. The halves were then examined to determine the differences that could be attributed to the different seeding approaches. In most cases one method of seeding would produce a clear and reproducible increase in growth rate over the other. The increased growth rate corresponded to higher nucleation density as determined by SEMs of the wafers. This procedure was utilized to evaluate four different approaches to seeding, and to evaluate different operator lapping techniques.

b. Air brush experiments. We attempted to seed silicon wafers by applying diamond particles to the surface with an air brush. Nominal 0.1 mm diamond abrasive was suspended in isopropyl alcohol or acetone and sprayed onto the wafers. We tried to obtain the densest possible monolayer of particles. Figure 1 shows the resulting seeded surface in a typical case, produced after much practice. Films grown on airbrushed wafers such as this were clearly coarser grained than conventionally seeded films. It was not necessary to utilize our comparison approach to see this. We were not able to improve our airbrushing skills to the point where these wafers had optical quality comparable to conventional wafers and so the approach was discontinued.

c. Wet vs. dry polishing. An often used technique for seeding Si wafers is to rub them with a cotton ball or Q-tip loaded with diamond abrasive. We observed that it was difficult to get uniform coverage of the wafer with this technique so we made a modification. We polished wafers on a soft dry lap that was loaded with abrasive, a procedure that seemed equivalent to the cotton ball approach. Significant differences were noted between wet lapped and dry lapped seeding. These differences are illustrated in Figures 2 and 3. Figure 2 shows two half wafers prepared by wet and dry lapping after one hour of growth under nucleation conditions. Figure 3 shows SEM photos of these films. It appears from these photographs that the dry lapping procedure leads to somewhat greater nucleation density and somewhat faster initial film growth than wet lapping.

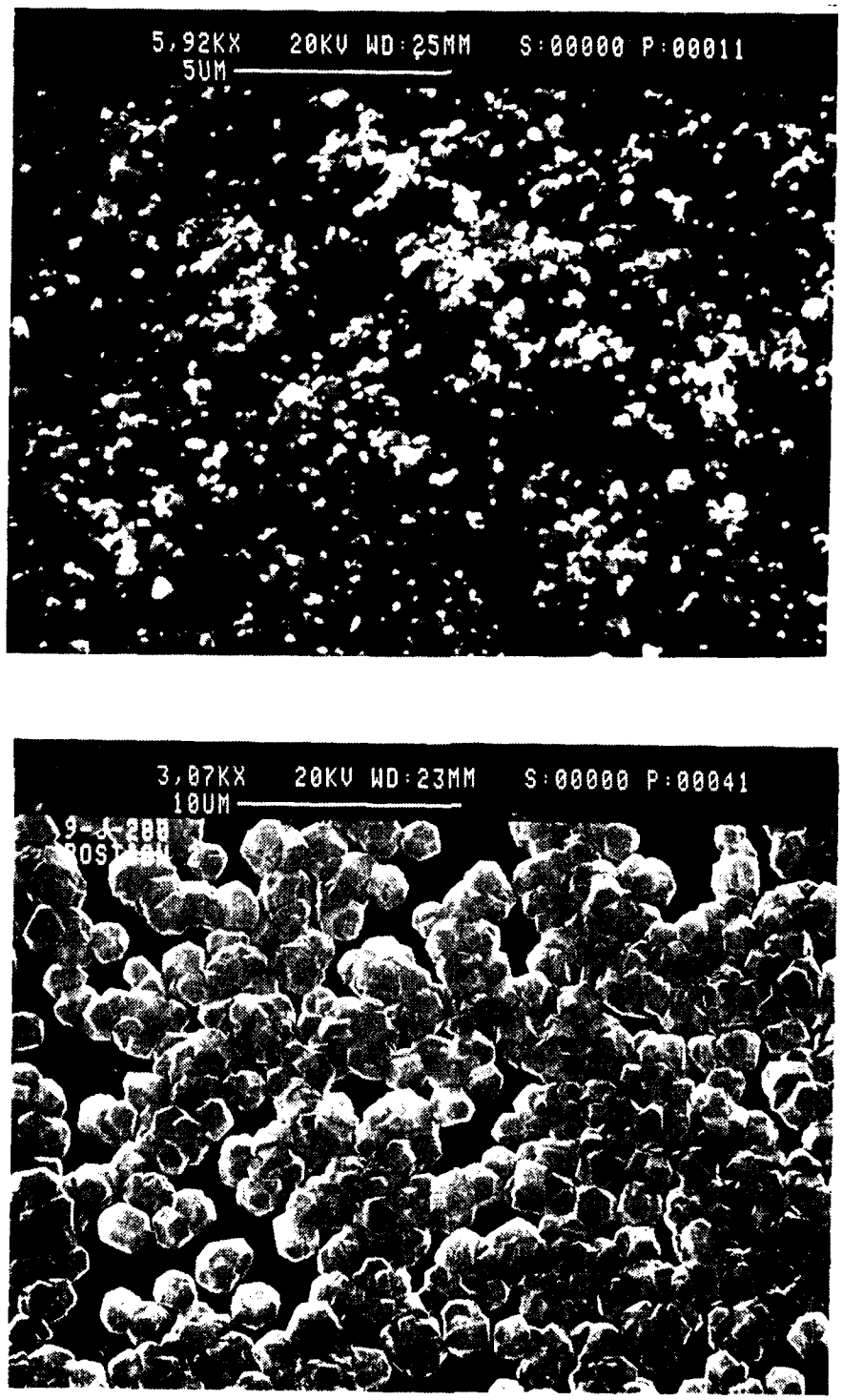

Figure 1 SEM's showing 0.1 µm diamond grit air-brushed on a silicon wafer(above), and then grown on for fourteen hours at 1.0 percent methane concentration

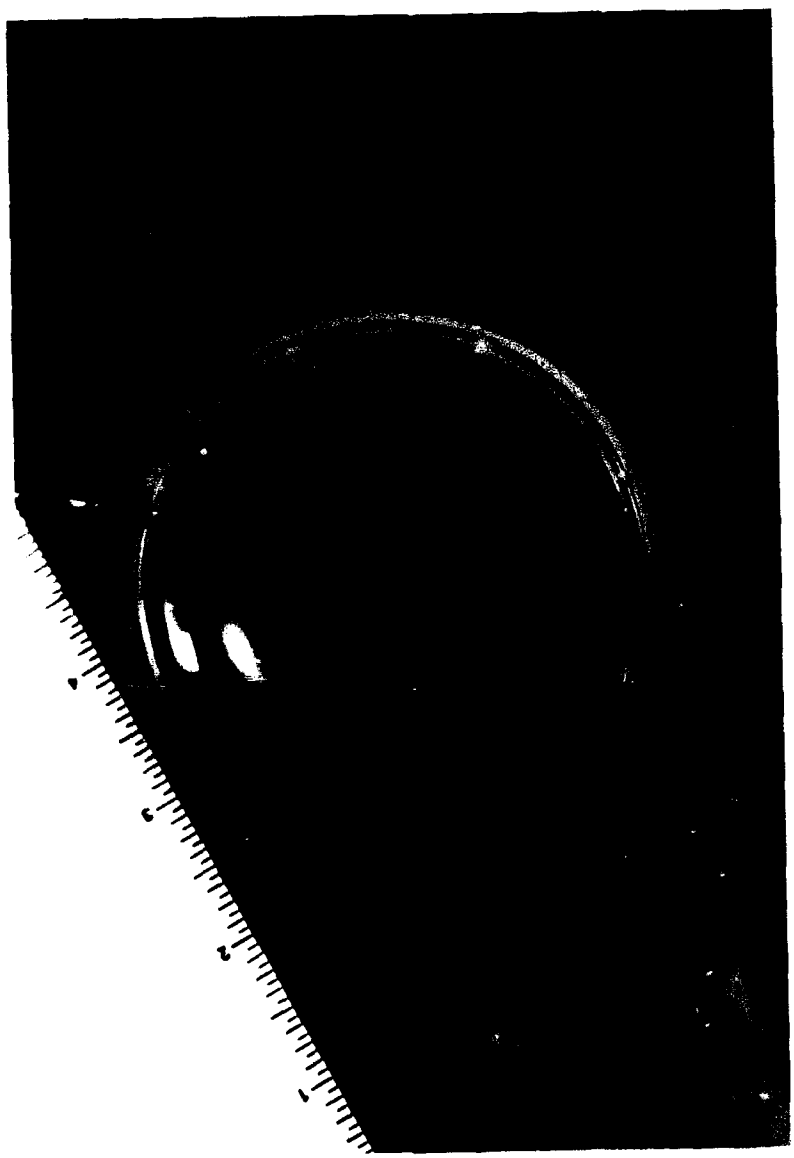

Figure 2 Photograph showing two half wafers seeded by different techniques but grown side by side. The half wafer showing less growth was scratched with wet 0.1 μm diamond powder. The other was scratched with dry 0.1 μm diamond powder imbedded in a cloth lap.

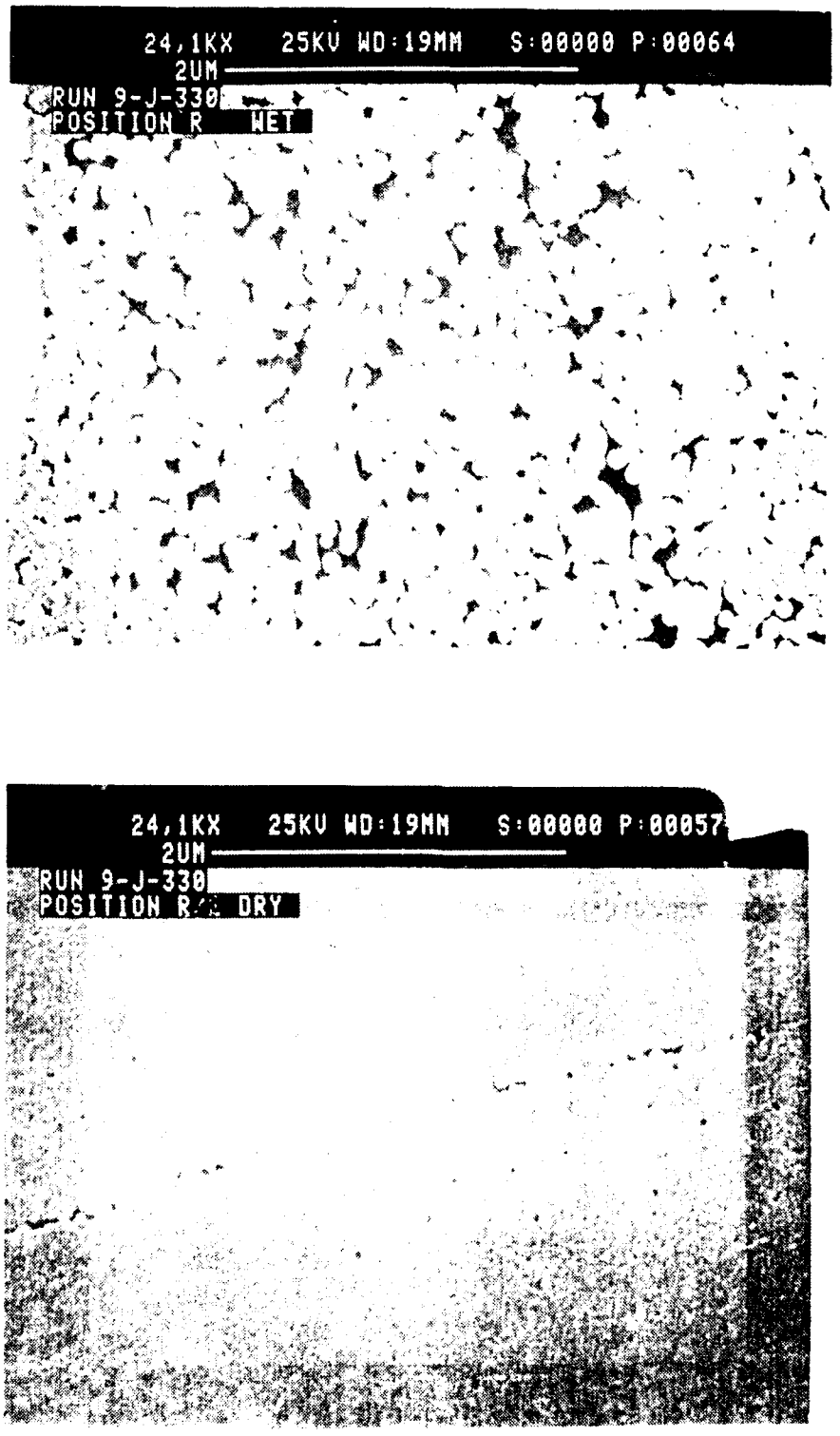

Figrue 3 SEM photographs comparing the edge regions of the two half wafers shown in figure 2.

d. Lapping technique. Similar experiments were performed to determine the effects of the length of time the polishing was carried out. It was found that there was little change in nucleation density between one minute and ten minutes of lapping. Lapping times in excess of ten minutes seemed to diminish nucleation density and growth rate. It is more difficult to get uniform coverage of the wafer with dry lapping than with wet lapping. The use of a soft cloth lap in place of the paper lap was found to make it easier to get uniform wafer coverage.

e. DC nucleation. Diamond films can be nucleated and grown in the DC reactors without seeding. The films so produced have uniform thickness and grain size across most of the wafer. Crystallume manufactures products utilizing 0.4 mm thick DC-grown films. This is approximately the film thickness at the end of the first growth stage in the microwave reactors. We investigated the usefulness of these films to serve as the equivalent of first stage growth. The grain was found to be is coarser than that of lapped wafers at the same thickness, and the grain size of completed films is somewhat larger than those produced by hand lapping.

The one notable advantage of these films is that they are more uniform in thickness than microwave films. This is attributable to the fact that the first 0.4 mm is flatter to begin with.

f. Conclusions and standard procedure. Based on the experiments above, we standardized on dry lapping for 2 - 3 minutes on a cloth lap as the procedure to seed wafers for diamond film growth. These conditions represent a broad optimum of nucleation density, and also minimize the possibility of systematic error due to changes in seeding technique.

2.2 MEMBRANE GROWTH

a. Reactor configuration. Most of the work reported here was performed in a microwave reactor like the one used in Phase 1 of this program. Figure 5 shows a schematic representation of this reactor. Additional work was performed in an Astex Model 17 reactor at the Astex facility in Massachusetts. We also made use of Crystallume's DC reactors, described in the Phase 1 final report, to produce nucleation layers as described in the previous section. In this section we will describe work performed in Crystallume microwave reactors.

b. Temperature profile control. All the work made use of 3 inch 100-oriented silicon wafers, nominally 20 mils thick. These wafers were supported on a rotating graphite stage. The wafer receives heat from the plasma and so its temperature is determined to a great extent by thermal losses due to radiation and conduction to the stage. The temperature of the wafers during Phase 1 and at the beginning of Phase 2 was visibly hotter in the center of the wafers than at the edges. It was thought that this was the explanation for the thickness, grain structure, and color nonuniformity of many of the membranes. The temperature profile was improved (i.e. flattened) by moving the plasma away from the center of the wafer, to a position about halfway between the center and the outer edge of the wafer.. This resulted in increased uniformity of thickness and grain structure of the membranes. Additional flattening was accomplished by using a specially designed wafer stage described below.

c. Wafer stage. Additional flattening of the temperature profile was achieved by changing the design of the wafer stage. New stages were fabricated from high purity graphite with the cross section shown in Figure 6. The thick central hub conducts heat away from the center of the wafer faster than the thin material at the outside of the wafer, with the overall result that the temperature profile is flattened compared with a solid disk-shaped stage.

The improvements in the temperature profile produced by these changes had the effect of flattening the thickness profile of the membranes, allowing us to increase their diameter from 30 mm to 36 mm with no loss of yield.

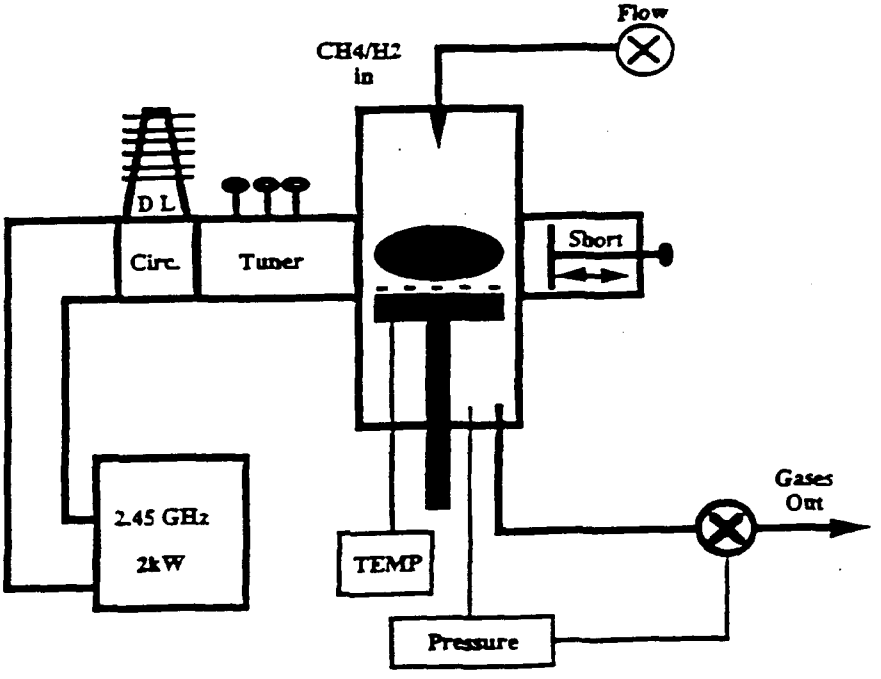

Figure 5 *Schematic drawing of the Crystallume microwave plasma deposition system.*

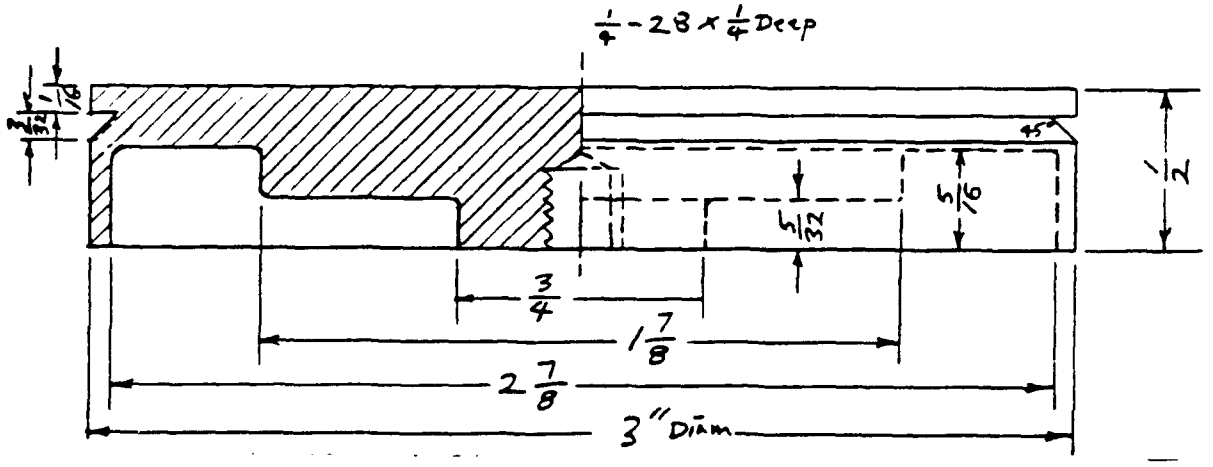

Figure 6 Drawing of the substrate stage utilized to control the temperature profile of the wafers during depositions.

d. Substrate temperature measurement. The temperature of the wafers was monitored by two means. A sheathed thermocouple was inserted through the center support structure and into the stage, and the surface temperature was read with an optical pyrometer. Both of these methods had difficulties. The thermocouple's reading corresponds to the temperature at a point removed from the silicon wafer and in a steep temperature gradient. Under the best circumstances it is only an approximation to the temperature of the substrate. In addition it's run to run reproducibility depends on the ability to assemble the system the same way each time, particularly with regard to the thermal contact between the wafer and the stage. For these reasons the thermocouple has to be considered to have an unknown systematic error attached to it as well as a run to run random error.

In principal the optical pyrometer should provide direct temperature indications of the wafer surface, eliminating difficulties associated with the thermocouple. In fact the pyrometer is constrained by the geometry of the reactor to view the wafer surface at a low angle, through a small aperture, through the quartz chamber walls, and possibly through the plasma. This produces uncertainty in proper aiming of the pyrometer, and the possibility that large errors could be made. Measurements made with the pyrometer pointed halfway between the edge and the center of the wafer gave the most reproducible results. The indicated temperatures were typically about 25 C higher than thermocouple readings. This provides an indication of the systematic thermocouple error.

The pyrometer measurements were so variable that they were only performed as a sanity check on the thermocouple. The thermocouple, in spite of its systematic and run to run errors, is the prime source of temperature information for the wafer during film growth. Temperature measurements were further validated by noting the microwave power and by visual estimates based on wafer color.

e. Deposition Parameters. The deposition parameters that can be controlled easily in the microwave reactor used in Phase 2 are chamber pressure, microwave power, gas composition, gas flow rate, and reactor configuration. These parameters determine the temperature of the wafer and the characteristics of the diamond film.

During the course of Phase 2 we experimented primarily with changes in the first three parameters, pressure, power and gas composition. The gas flow rates were kept constant, and only small changes were made in the reactor physical configuration. The latter consisted primarily of addition or

subtraction of insulation around the edge of or under the wafer stage in an effort to control the temperature of the wafer independently of the microwave power. Only small changes in temperature could be produced this way for any set of process conditions.

The range over which the pressure can be changed is also limited. At a given microwave power level, the pressure must stay above a particular value to suppress plasma instabilities. The most frequent instability was the appearance of a plasmoid on the clips holding the wafer to the stage. If the clips are eliminated the next type of instability to occur is the plasma ball jumping to the wall of the chamber.

Lowering the pressure has another undesired effect: it causes the wafer temperature to fall, because of reduced heat transfer from the plasma to the wafer.

These interactions taken together determine a parameter space in which the reactor can be operated and over which the diamond film deposition conditions can be varied. This parameter space is shown in Figure 7. The box encloses the region in which most of the wafers were grown.

Figure 8 shows another representation of the experimental parameter space. On this figure we also show the positions of several wafers grown at Astex in a Model 17 reactor. Much lower pressures can be utilized in the Astex reactor because it has an independent heater for the wafer stage. We will say more about these wafers in a later section.

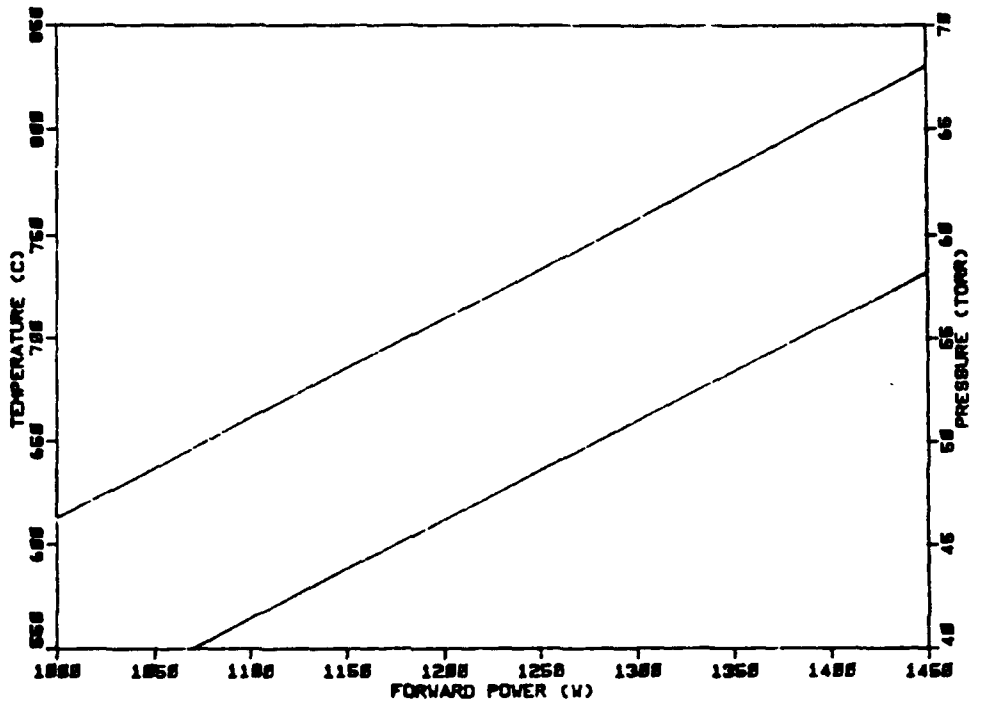

Figure 7: Approximate boundaries of the parameter space utilized for membrane depositions in the Crystallume reactors.

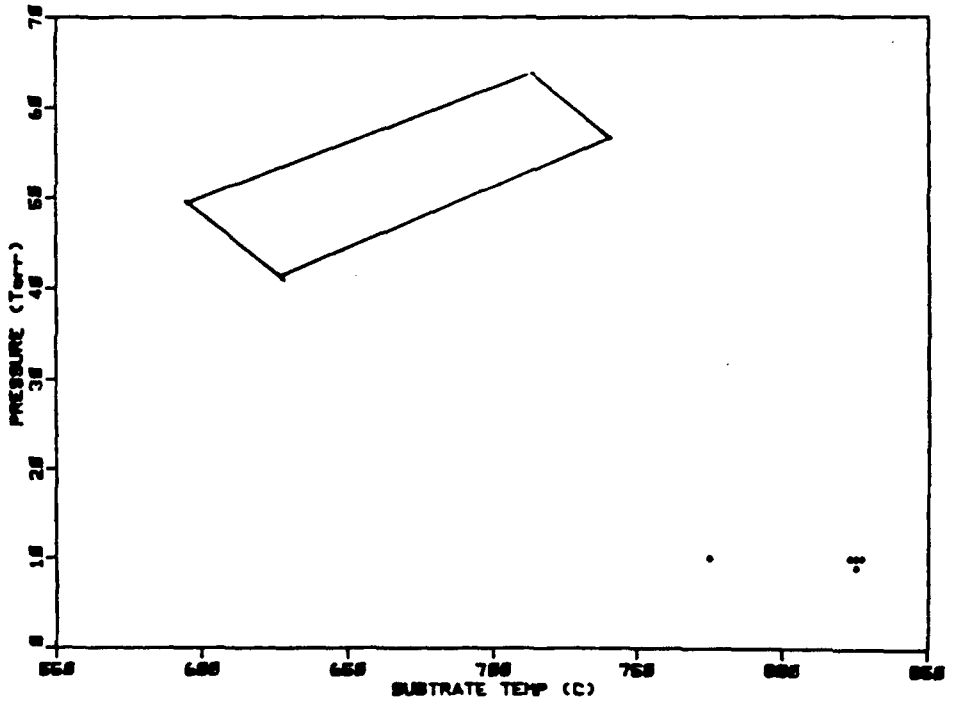

Figure 8 Temperature-pressure range of interest for membrane growth. The portion studied with the Crystallume reactors is enclosed in the solid lines. The points represent membranes grown for Phase 2 at 10 torr in an Astex reactor.

2.3 DEPOSITION PROTOCOL

Diamond depositions were carried out on wafers that had been seeded as described in Section 2.1f. The wafers were mounted to the holder with molybdenum clips. Diamond films were then grown in two stages, a nucleation stage and a growth stage.

a. Nucleation stage: It had been established in Phase 1 of this program that an initial one hour of growth in a mixture of 91% hydrogen, 9% methane produced a high nucleation density base on which to grow the bulk of the membrane. During Phase 2 we tried higher methane concentrations in the nucleation stage, finding that a 12 percent methane concentration produced finer grain films, but at the expense of a higher incidence of pinholes, or point defects in the membranes. Most of these defects appear to arise from material nucleating and falling off the counter electrode. Accordingly we standardized on a one hour nucleation stage as follows:

Hydrogen flow	10 sccm
Methane flow	100 sccm
Methane conc.	9.09 %

b. Growth stage: Following the nucleation stage the growth stage was initiated by changing the gas flow to a higher overall flow rate and to lower methane concentration. In some instances the power was changed in order to establish a different wafer temperature. The most often used gas conditions were 150 sccm hydrogen, 1.1 sccm methane, giving 0.73 percent methane in hydrogen. The methane concentrations utilized in the second half of Phase 2 are shown in Table 1:

Number of Membranes	Hydrogen Flow	Methane Flow	Methane %
8	150	.5	.33
1	150	.75	.5
2	150	1.0	.66
45	150	1.1	.73
6	150	2.0	1.33
1	150	2.5	1.66
2	150	3.0	2.0
1	150	3.5	2.3

Table 1. Gas flows used for membrane growth.

c. Membrane growth in Astex reactor: A total of seven membranes were grown at the Astex facility. These were grown on wafers seeded at Crystallume as described in Section 2.1f. A nucleation stage lasting 1/2 hour was utilized prior to growth.

2.4 MASKING AND ETCHING

After the diamond deposition on a silicon wafer is completed and SEM photographs are taken, it is etched to form a membrane, typically 36 mm diameter. This is accomplished by masking the back side of the wafer appropriately and immersing it in acid etch.

a. Masking with wax: Acid resistant black wax with a softening point of 80-90 C is used to form the mask. The diamond side is left unwaxed except for the bare spots formed by the clips that hold it in the reactor. In order to melt the wax on the silicon side it is necessary to warm the sample to a temperature of 100-120°C. Then the wax is painted on using a marked circle as a guide. After waxing is completed a cooling down period is necessary before submerging the sample into the etching solution.

b. Masking with tape: Teflon tape can also be used to protect the silicon in the etching process. A roll of four inch wide Type 5480 Teflon tape as purchased from 3M. The procedure was to cover the back of the wafer with the tape and then cut the necessary circle using a simple self-centering guide. We found a number of difficulties masking with tape. First, the etching solution sometimes undercut the tape, causing damage to the back side of the wafer. Second, it was difficult to remove the tape after etching because of the poor solvent penetration under the tape. Finally, the adhesive-solvent mixture left a residue on the membrane that was difficult to remove. The tape method was finally abandoned in favor of the black wax procedure.

c. Etching: Silicon is soluble in a mixture of nitric (HNO_3), hydrofluoric acid (HF), and acetic acid (CH_3COOH). The ratio that gives the best results is 2:1:1, giving an etch rate of approximately 4 mm/ minute, which is dependent on the solution temperature. Stronger solutions produce a higher etch rate but also raise the danger that the etch solution will exceed the softening temperature of the wax. After etching is competed the wax is removed by submerging the wafer in TCA.

3.0 MEMBRANE CHARACTERIZATION

In this section we will discuss the characteristics of the membranes produced during Phase 2 as they relate to the process conditions. The following membrane characteristics will be discussed:

3.1 THICKNESS AND GROWTH RATE

a. Thickness determination. The surest way to determine the thickness of membranes is by viewing an edge in the SEM after a membrane is broken, as shown in Figure 9. The thickness of intact films can be estimated by counting the Fizeau rings visible in reflected light (see Figure 2), assuming that a monotonic thickness variation from zero to the maximum exists on the substrate, and that all of the fringes are visible so they can all be counted. A set of fringes can usually be found near the clips holding the wafer to the stage, extending from the bare substrate under the clip to the concentric circular fringes near the center of the wafer. Assuming a wavelength of 500 nm and a refractive index of 2.4 for the diamond film, the film thickness increment between adjacent fringes is 1.04 mm, a convenient value for estimation purposes. This method has two weaknesses. The first is the ease with which fringes can be missed, leading to under-estimation of film thickness. The second is the uncertainty of the refractive index, which can range between 2.2 and 2.5 according to ellipsometric measurements.

A more reliable nondestructive thickness determination can be made from the progression of constructive and destructive interferences in the absorption spectrum of a membrane (See Fig. 10). This method eliminates the uncertainty of counting Fizeau rings, but not of the refractive index. The thickness d is obtained from the difference between the wavenumber of two successive transmittance peaks from the relation

$$(1) \qquad 1/d = 2n(1/\lambda_2 - 1/\lambda_1)$$

where n is the refractive index of the membrane.

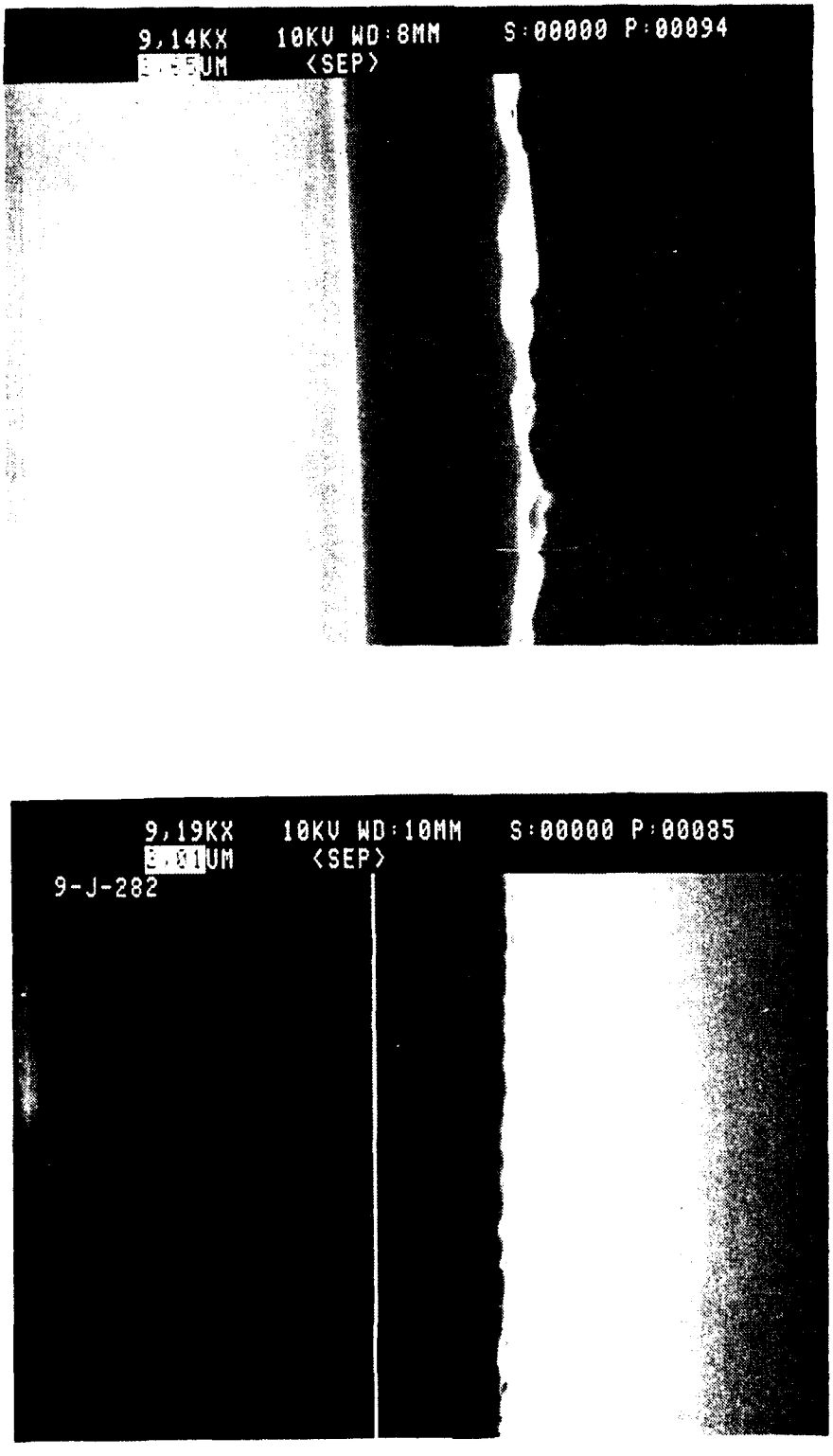

Figure 9 SEM photograph of the fractured edges of two membranes. These provide an indication of the film morphology and facilitate a precise thickness determination.

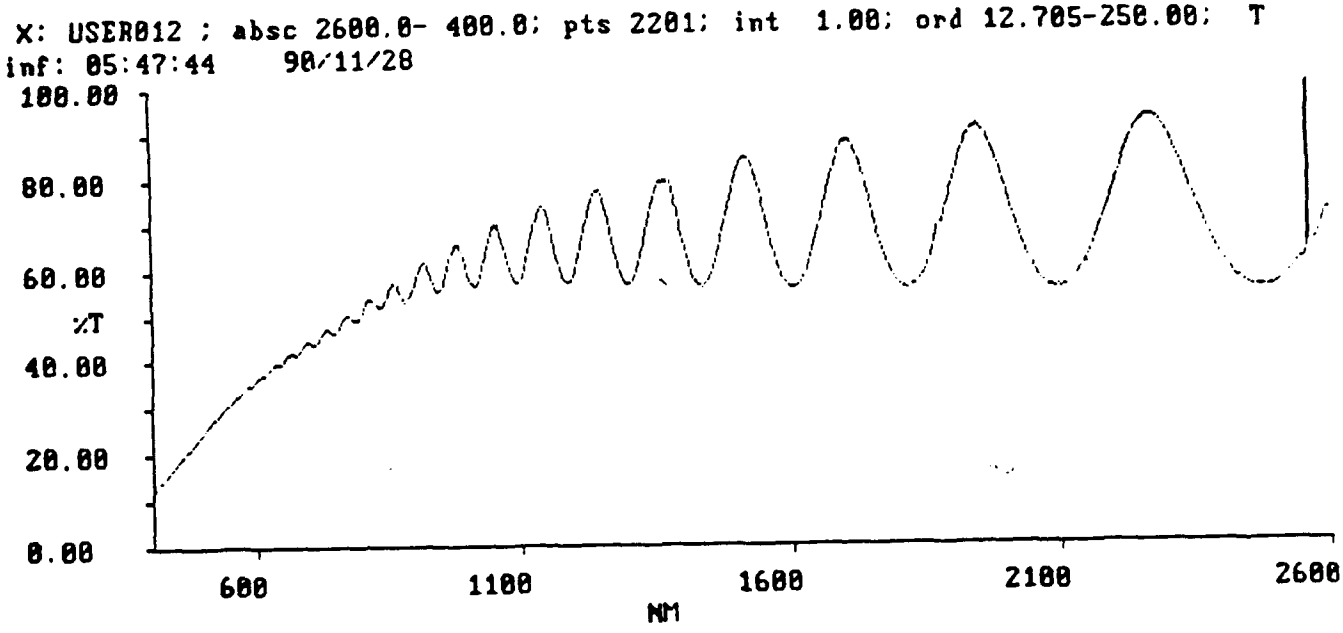

Figure 10 Typical visible - IR transmission curve for membranes produced in this program . The oscillations make possible a determination of thickness to within the accuracy that the refractive index is known.

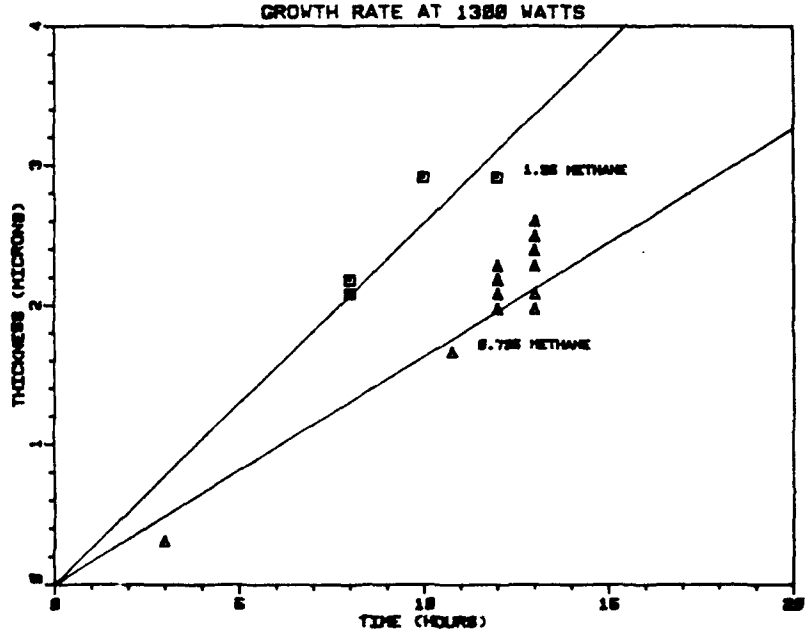

Figure 11 Experimental determinations of growth rate for two different methane concentrations.

b. Growth rate. Growth rate data are summarized in Figure 11, in which measured wafer thickness is plotted against growth time for membranes grown under two different methane concentrations. Because of the imprecision of the thickness determinations of intact membranes, we have ignored the difference in in growth rate between the nucleation stage and the growth stage.

3.2 TENSILE STRESS

At the beginning of Phase 2 the conditions needed to produce membranes in tension were not known. As Phase 2 unfolded it became evident that the films with the best optical quality were often in compression, whereas the membranes in tension often had higher scattering. After the systematic assembly of data about each membrane, including consistent (if inaccurate) substrate temperature estimation, it became clear that, at least under the specific process conditions we used, higher substrate temperatures under otherwise identical process conditions lead to tensioned membranes, while lower substrate temperatures lead to compressive membranes. The point is illustrated in Figure 12, in which the labelled points showing membranes in tension are clustered at the higher temperatures. Figure 12 will be discussed further in the following section.

Quantitative determination of the tensile stress was made by means of bulge tests, performed by Nanostructures, Inc. (Their report is attached as Appendix A.) Briefly, this method consists of applying pressure to one side of the membrane and measuring the deflection (amount of bulge) as a function of pressure. This data can be fit to an expression involving the bi-axial modulus $E/(1-\nu)$, where E is Young's modulus and ν is Poisson's ratio, and σ_0, the residual tensile stress of the membrane. Table 2 shows the values obtained from membranes grown in Phase 2.

Sample	Average Thickness	Tensile Stress x109 dyn/cm2	Bi-axial Modulus x1012 dyn/cm2
A243	2.6	1.6	8.2
349	3.2	2.4	11.0
368	2.5	0.38	9.3
396	2.2	0.57	11.0

Table 2: Membrane stress and bi-axial modulus

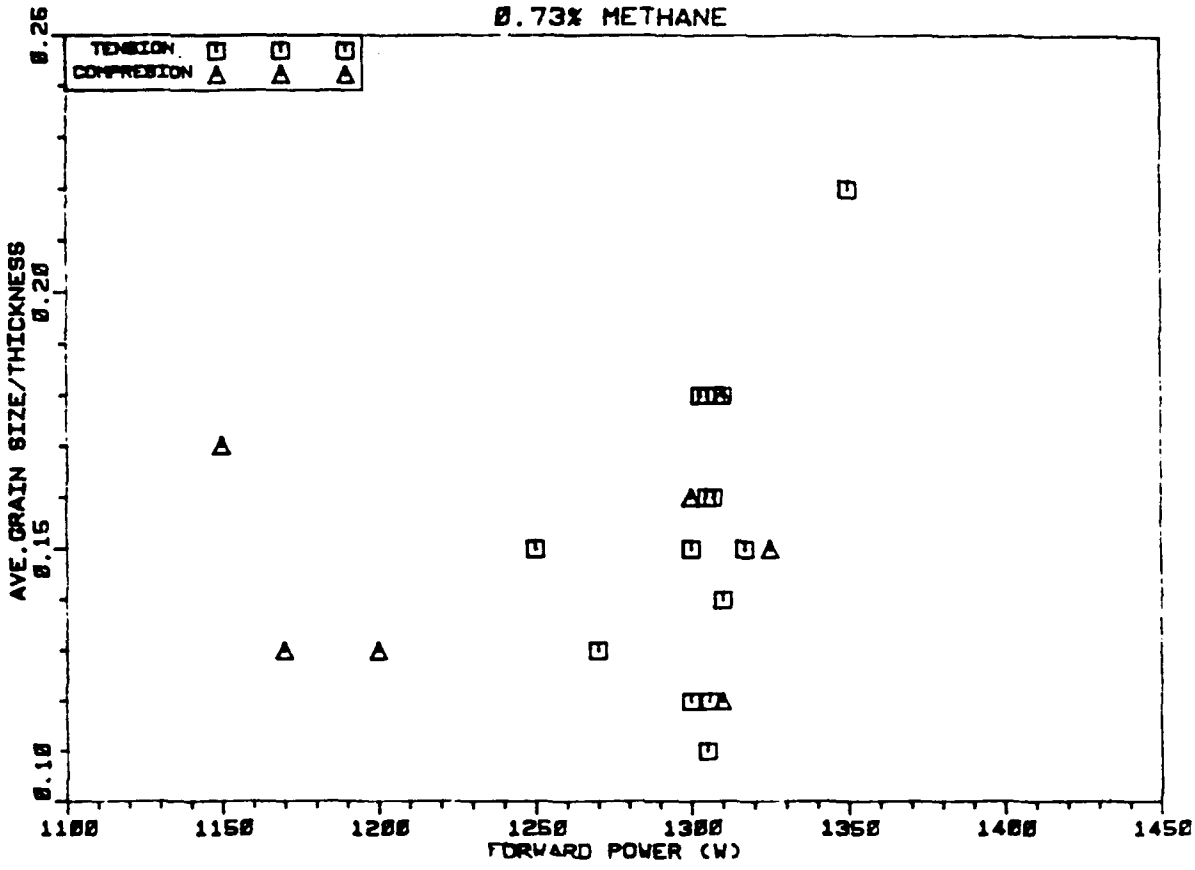

Figure 12 Average grain size/thickness vs. power (which correlates strongly with wafer temperature) for membranes grown in 0.73 percent methane. The rectangular "points" represent membranes found to be in tension. This data illustrates that tensile membranes are priduced at wafer temperatures somewhat higher than those that produce the minimum size grain.

3.3 Grain Size, Surface Roughness and Optical Scattering

A major issue of diamond membrane growth is the necessity of holding the grain size to the smallest value to assure the best possible surface smoothness and minimum optical scattering. Figure 13 shows a SEM photograph of a typical membrane grown in a Crystallume reactor. Figure. 14 shows a SEM photograph of a membrane grown in an Astex reactor. A number of factors that effect grain size can be listed from our observations These are:

- Nucleation density
- Film thickness
- Film growth temperature
- Chamber pressure
- Methane concentration

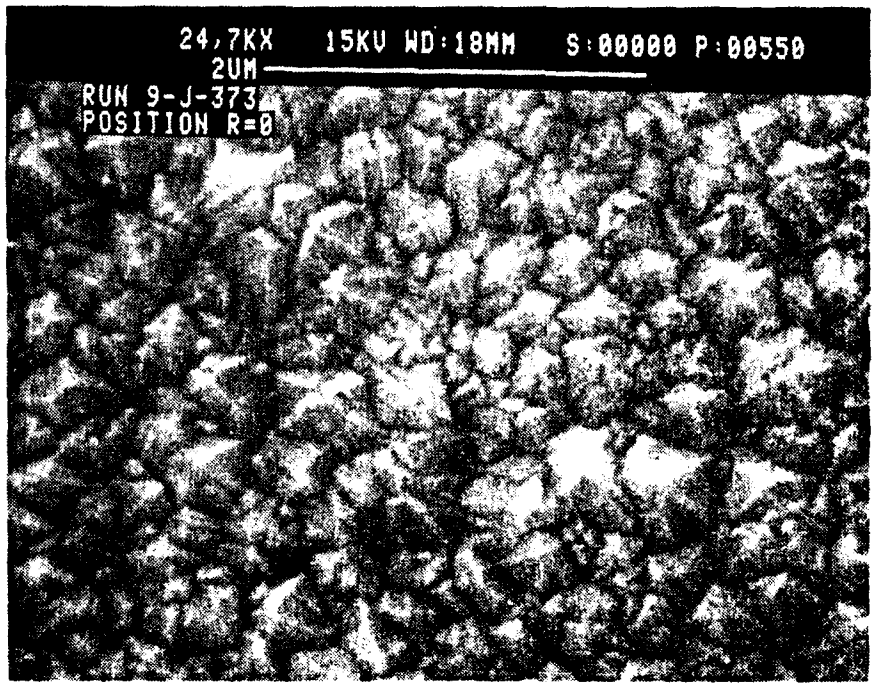

T= 2.6 um

M= 0.73%

PWR=1300 W

P= 60 Torr

TEMP+720 C

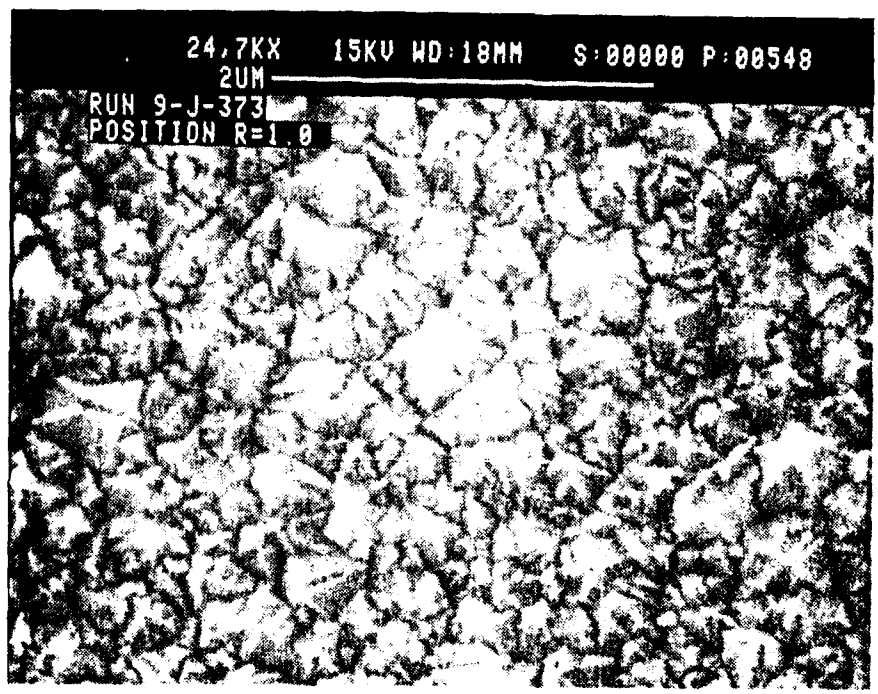

Figure 13 SEM photographs of a typical membrane grown in a Crystallume reactor.

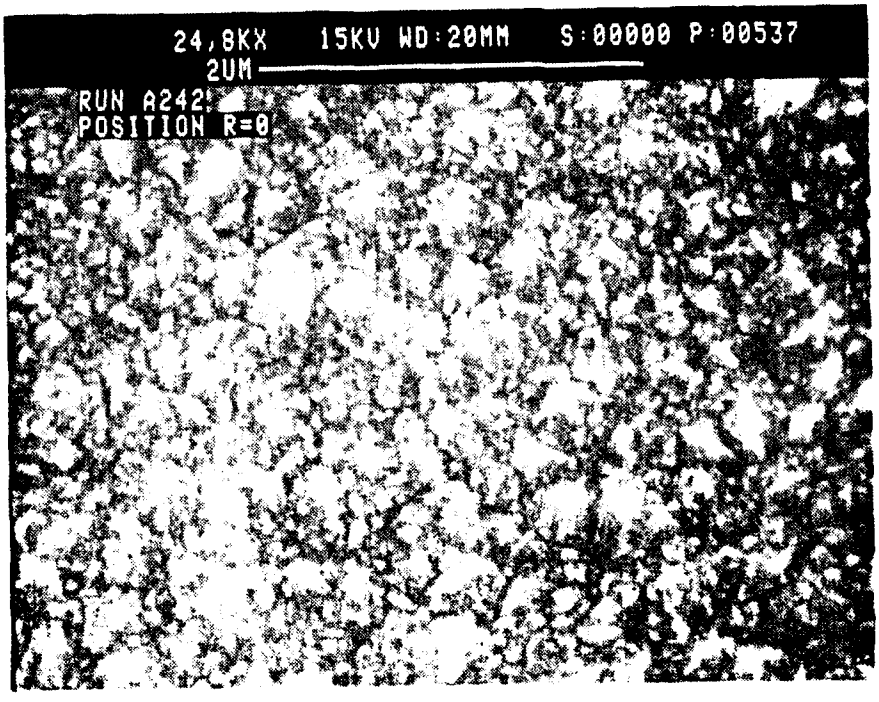

T=4.1 um

M=1.00%

PWR=550 W

P =10 torr

TEMP=825 C

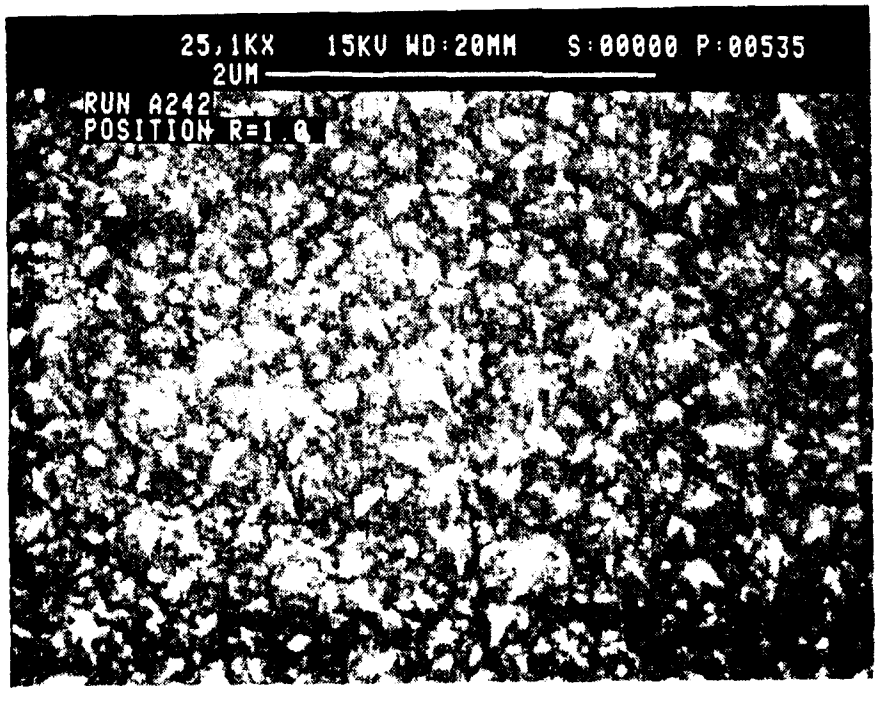

Figure 14. SEM photographs of a membrane grown under low pressure conditions in an Astex reactor.

Nucleation density: The role of seeding and nucleation density on subsequent film grain size was discussed in the nucleation section.

Film thickness : The growth of grain size with increasing film thickness is almost universally observed in diamond film growth. Because most of our film growth was targeted at 3 micron film thickness we did not accumulate data on grain size of intermediate thickness membranes for the purpose of quantifying the relation between grain size and film thickness. The little data we have for a specified set of reactor conditions displayed in Figure 15. This supports the observation that grain size is an increasing function of film thickness. The best membrane optical quality, from the standpoint of absorption as well as scattering, will be obtained with the thinnest films.

Film growth temperature: In order to examine the role of temperature in determining grain size it is useful to assume that grain size has a linear dependence on film thickness. In Figure 12 we show normalized grain size (average grain dimension divided by film thickness) as a function of forward power in the microwave reactor, which strongly correlates to the wafer temperature. Figure 12 demonstrates a trend toward larger grain size at higher microwave power, independent of film thickness. On the other hand films in tension are produced at the higher temperatures. Therefore the optimum temperature to produce small grain size membranes in tension is a compromise between the competing demands of high temperatures to increase residual stress, and lower temperatures to limit grain growth.

Chamber pressure: The role of chamber pressure in determining grain size can be inferred from the best results we obtained in the Crystallume reactor, which was typically run at 50 torr, compared with the best results in the Astex reactor which we ran at 10 torr. These results are summarized in Table 2.

Reactor	Pressure	Grain size	Methane conc.
Crystallume	50 torr	0.4 mm	0.73 %
Astex	10 torr	0.2 mm	0.75 %

Table 3: Grain size obtained at different pressures

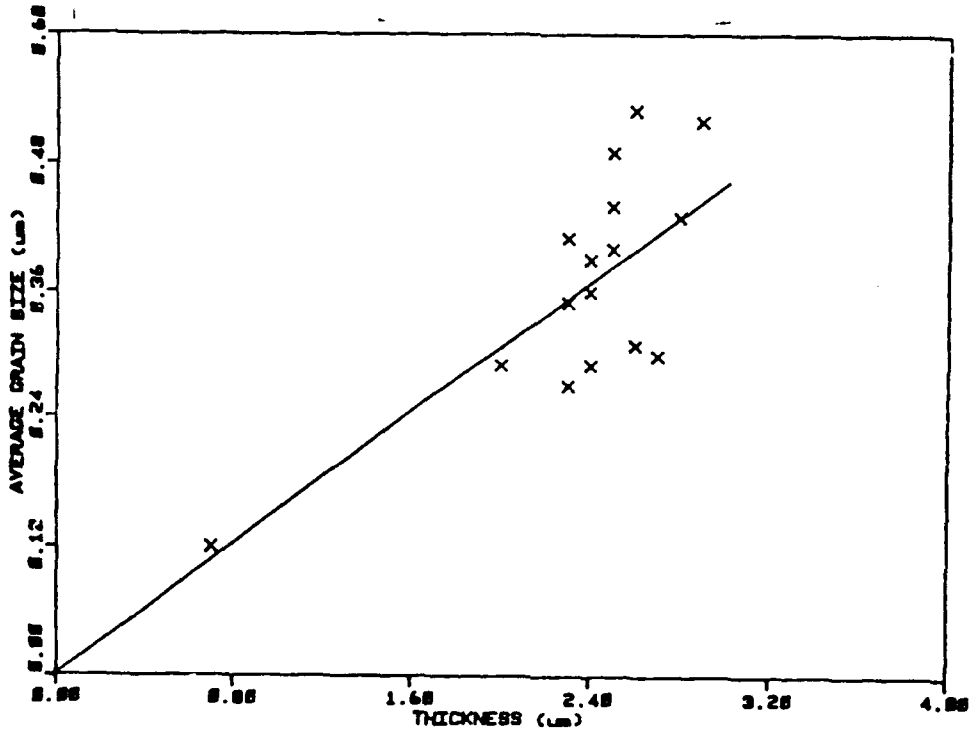

Figure 15 Average grain size versus thickness for membranes grown at 1300 watts in 0.73 percent methane. Average grain size is observed to increase roughly linearly with thickness. This allows us to use grain size/thickness as a measurement of film quality in Figures 12 and 16.

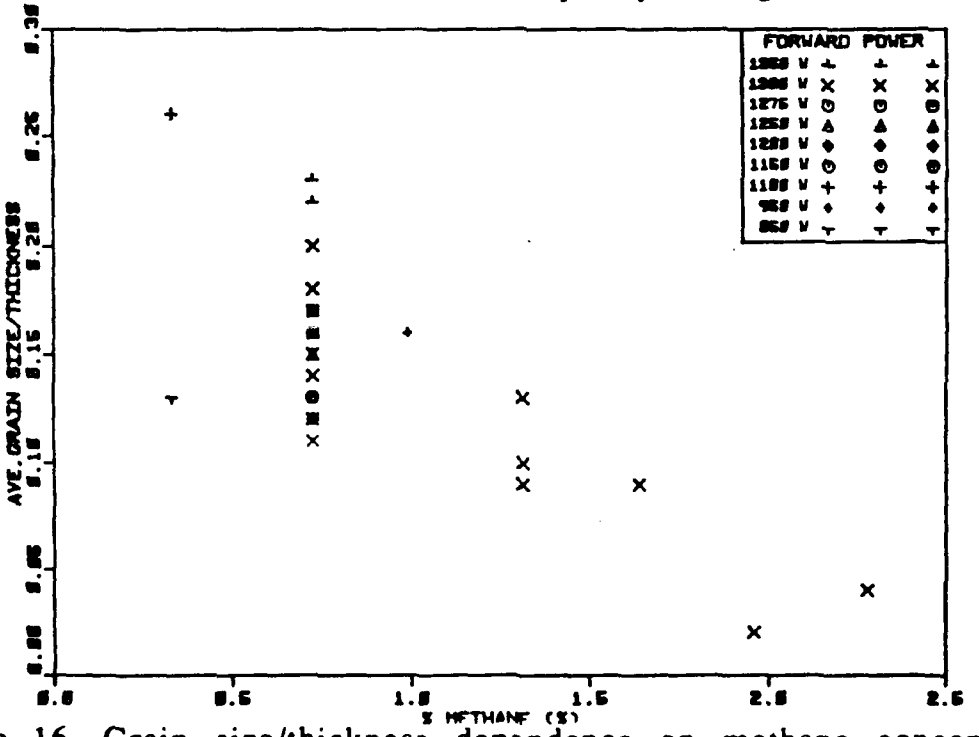

Figure 16 Grain size/thickness dependence on methane concentration.

Methane Concentration: The dependence of grain size on methane concentration is very clear from Figure 16, which shows normalized grain size as a function of methane concentration for wafers produced under a great range of conditions, including those prevailing in the Astex reactor. It is very clear that the methane concentration is an unequivocal determinant of grain size. The reason we emphasized growth in 0.75 % methane was the fact that higher concentrations led to the formation of graphite in the reactor, and to high optical absorption. Therefore the yield of cosmetically acceptable membranes was highest at the lower methane concentrations.

Surface roughness measurements: Surface roughness measurements were performed by Zygo Corp. utilizing their newly introduced interferometric microscope equipment. Their results are summarized in Appendix C. Unfortunately the results are inconsistent (a factor of 10 or so too smooth) with expectations from SEM observations of our films and from data reported for other diamond membranes. (Windischmann and Epps, J. Appl. Phys. (1990))

Optical Scattering: Optical scattering measurements made by George Celler indicate that typical Phase 2 *diamond membranes* scatter light at 633 nm approximately 100 to 500 times more strongly than a polished silicon wafer.

3.4 OPTICAL ABSORPTION

Most membranes exhibit, to a greater or lesser degree, a brownish color when viewed in transmitted light. The transmittance spectrum of a typical film is shown in Figure 10. There is very little variation in the overall shape of the transmittance spectrum from one membrane to the next. Films with higher grain size (and consequently higher scattering) can be more nearly colorless, i.e. have less of the brownish color, but this is difficult to quantify because the transmission losses due to scattering have a wavelength dependence similar to the optical absorption (See Figure 17). In Figure 17 films with less scattering can be recognized because they have more oscillations due to successive constructive and destructive interference of the internally reflected light with the directly transmitted light. Films with higher surface scattering produce less pronounced squiggles. Additional absorption spectra are included in Appendix A.

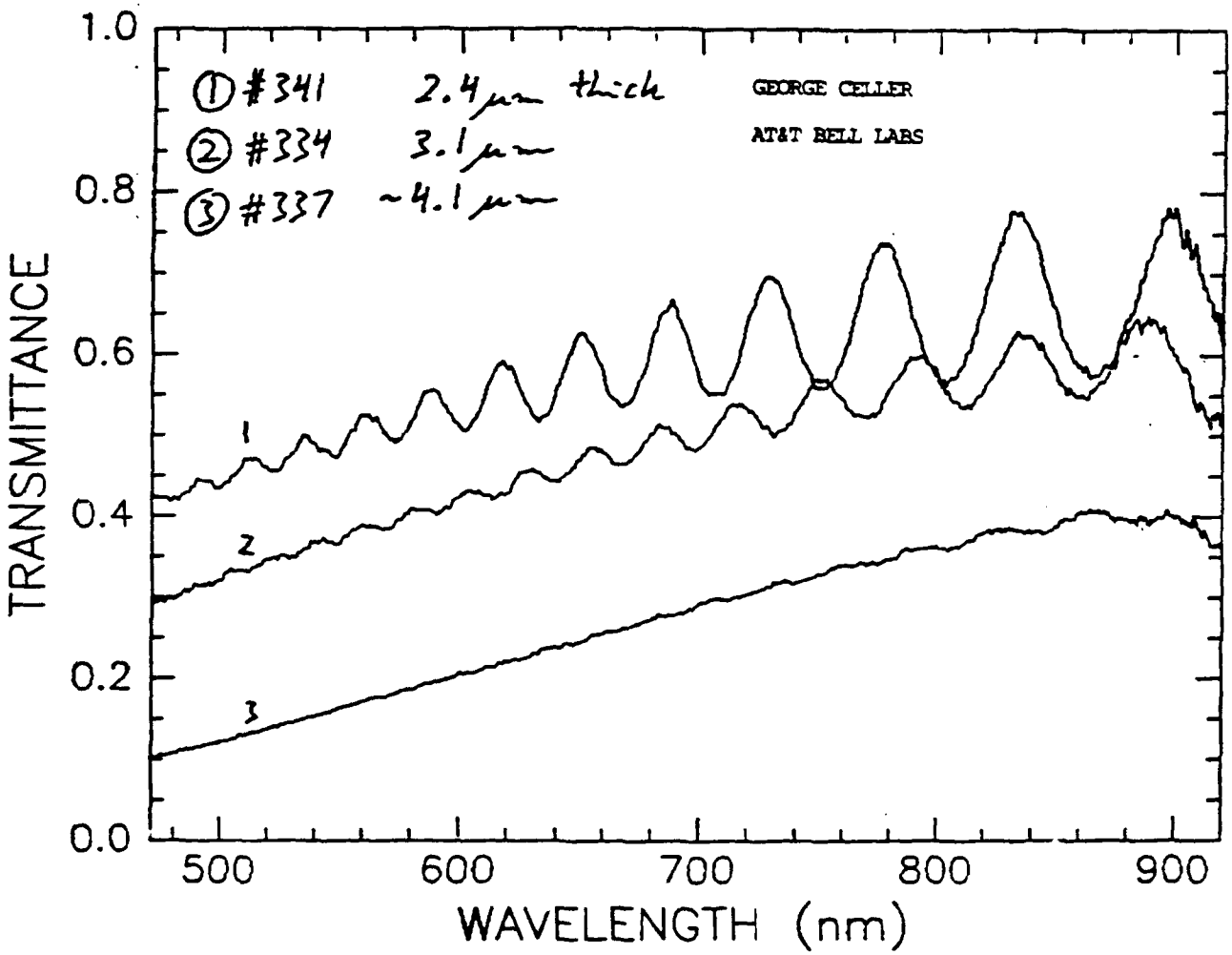

Figure 17 Visible transmission spectra for three different membranes. Curve number 3 shows the effect of strong surface scattering on the transmission curve. This figure was provided by Dr. George Celler, Bell Labs.

3.5 RAMAN SPECTRUM

Raman spectroscopy was used to characterize the diamond films. Raman spectra were obtained for all of the films produced in this program, using an excitation wavelength of 514.5 nm. The spectra obtained for different membranes all showed a strong diamond peak at 1332 cm^{-1}, but the ratio of the diamond peak to the non-diamond signal varied depending on the material preparation. The range of variation observed is shown in Figures 18a through 18c. The ratio of the height of the diamond peak to the non-diamond peak was recorded for the films. In Figure 19 this ratio is plotted against absorption coefficient at 600 nm. The positive correlation suggests that the optical absorption observed arises from the presence of non-diamond bonded carbon in the films.

We observe that the "better" Raman spectra, those with the highest and sharpest diamond peak, are associated with the membranes with the larger grain sizes. .Fine grain films have a strong non-diamond component. This is consistent with the model that associates the non-diamond bonded material with the surfaces of the individual grains. As the grain size gets smaller the surface to volume ratio increases, giving rise to the increased non-diamond peak.

3.6 X-RAY ABSORPTION AND DAMAGE

X-ray absorption of two membranes was measured by Greg Wells at CXrL, University of Wisconsin. Figure 20 shows the energy spectrum of the low intensity and high intensity beams at CXrL.. The low intensity beam was used for the absorption measurements. The high intensity beam was utilized for the X-ray damage studies to be reported below. Two measurements were made. One was a simple determination of the attenuation of the beam caused by the presence of the membrane. The second measurement was an absorption scan across a membrane, shown in Figure 21. Also plotted in Figure 21 is the thickness profile of the membrane..The absorption variation across the membrane is entirely consistent with the thickness profile.

Membranes exposed to the high energy beam at CXrL did not show any changes in optical absorption or in physical appearance after an accumulated exposure of 20 MJ/cm^3. The limit of the exposure completed during Phase 2.

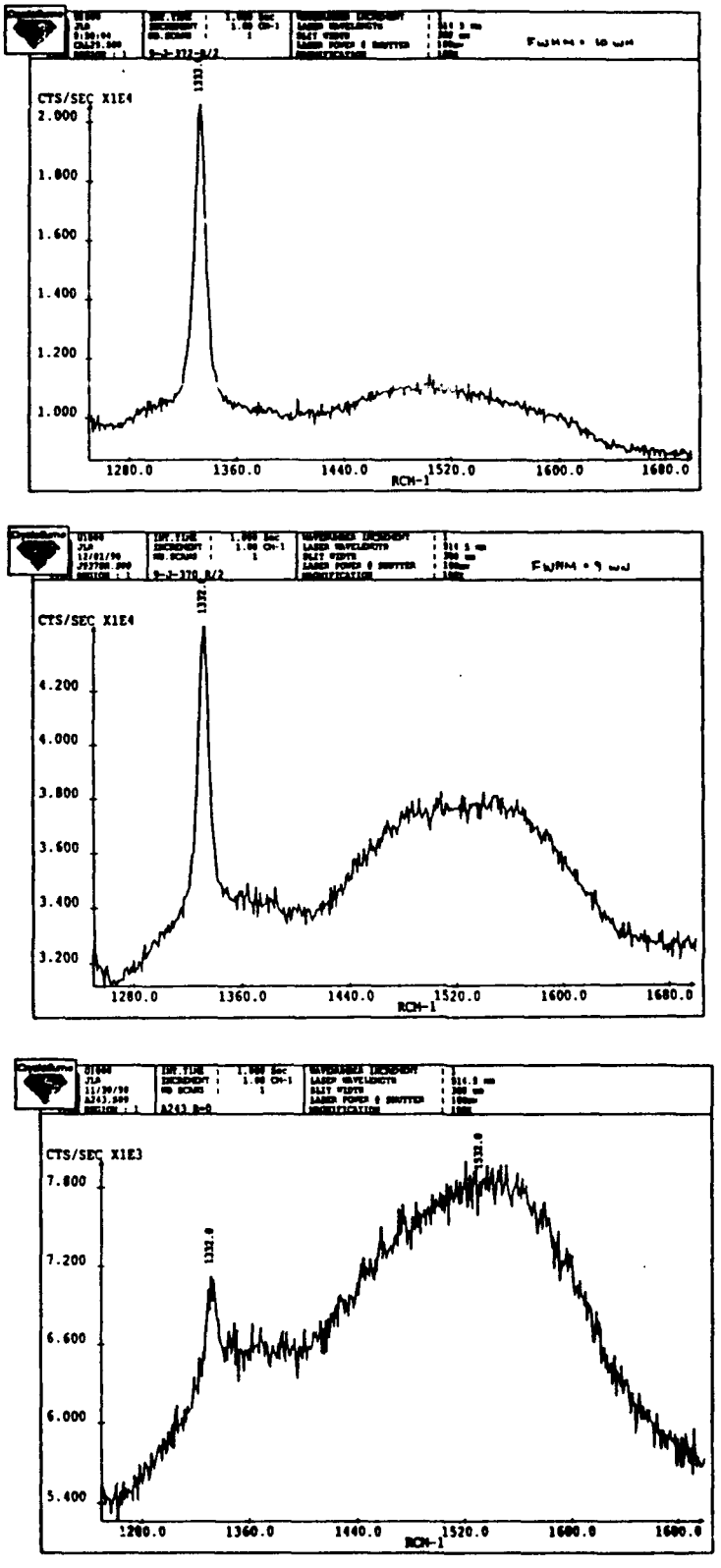

Figure 18a and b Typical Raman spectra for membranes grown at 1300 watts and 0.73 percent methane in the Crystallume reactors. Figure 18 c Raman spectrum for a wafer grown at 825 C. 1 percent methane in an Astex reactor.

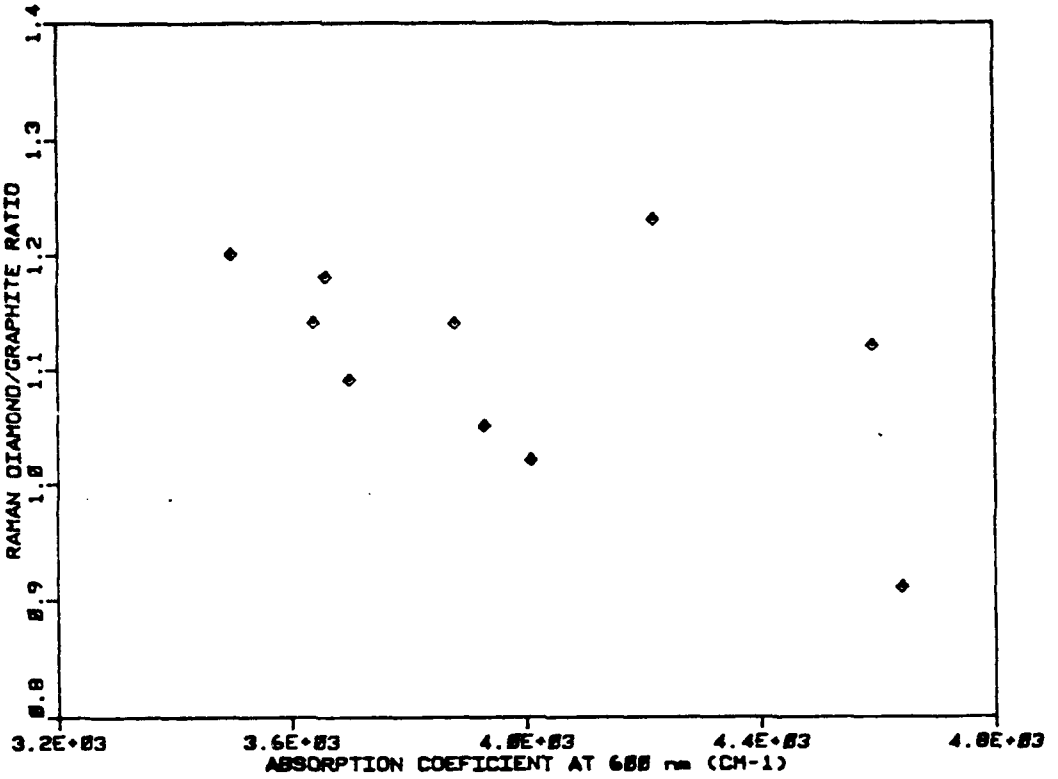

Figure 19 The ratio of diamond to non-diamond peak heights in the Raman spectra, compared with the absorption coefficient at 600nm. for membranes grown under a variety of conditions.

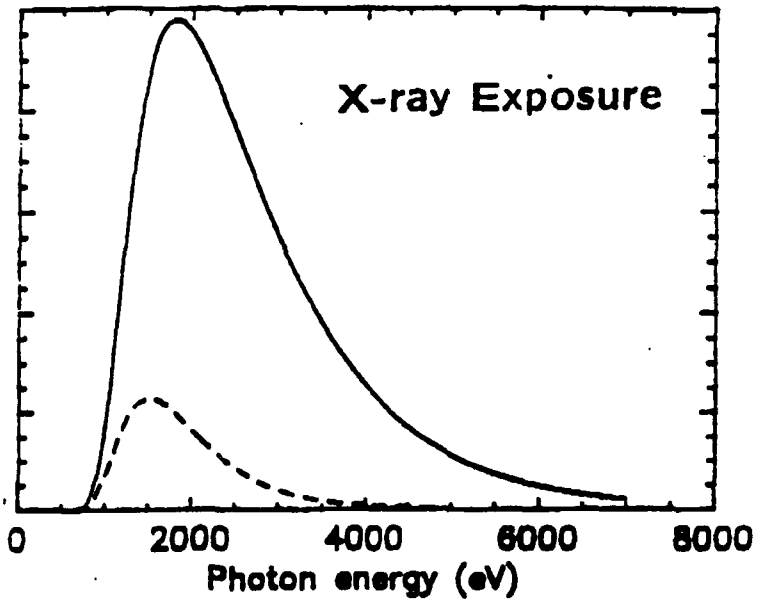

Figure 20 Energy Spectra of the X-ray source at University of Wisconson. The lower spectrum was used for absorption measurements and for some of the X-ray damage study exposures. The higher spectrum was used for most of the damage study exposure.

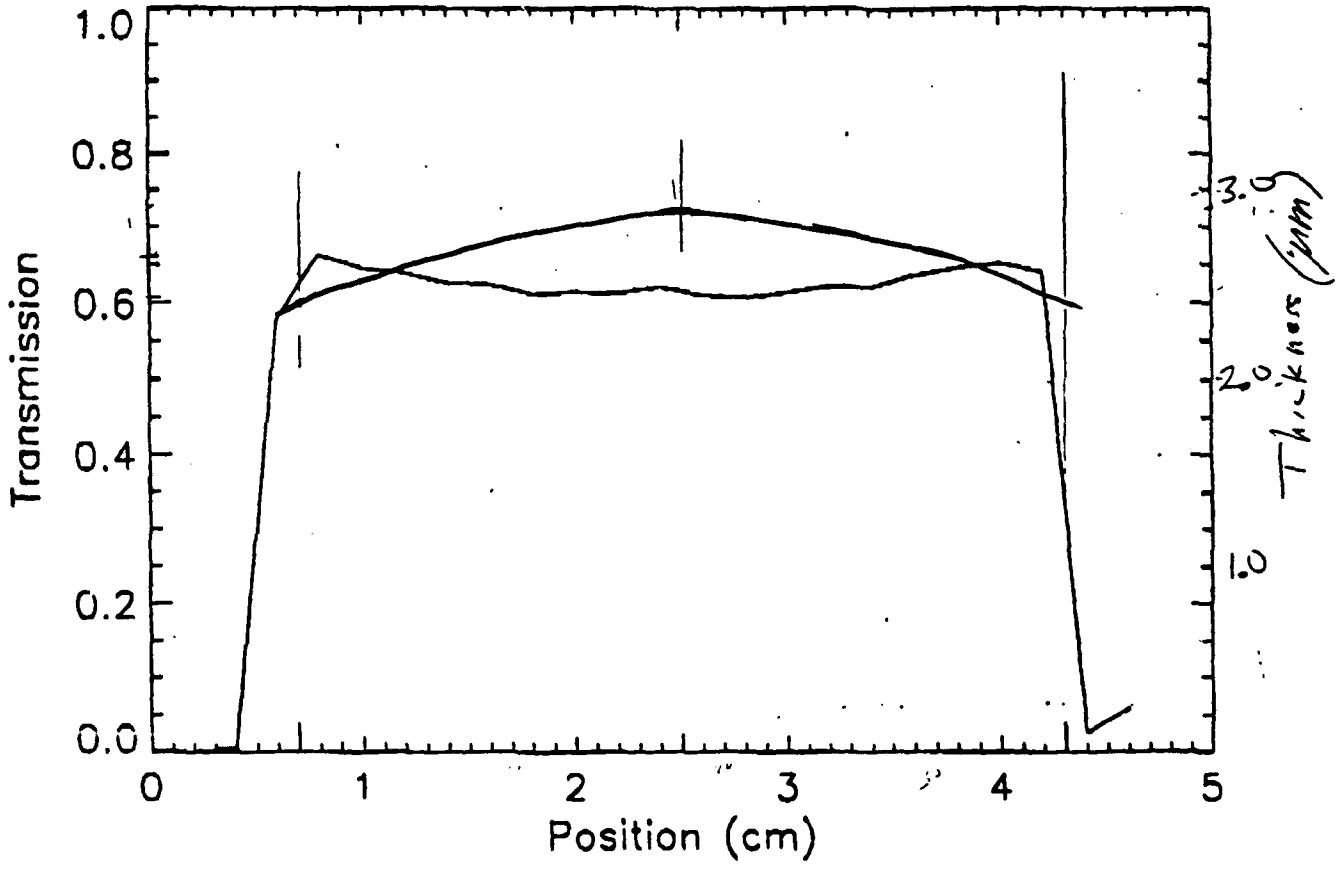

Figure 21 Lower curve: X-ray transmission through a membrane as a function of position. Upper curve: Thickness profile of the membrane determined from transmission measurements and interference ring count. The two are consistent within the experimental accuracy. The implied absorption coefficient is approx.$1.3X10^3\ cm^{-1}$. Data Provided by Greg Wells, CXrL.

X-ray damage studies had been planned initially in collaboration with P. Pianatta at the Stanford Synchrotron Radiation Laboratory. This work could not be undertaken at Stanford, but Redaelli and Piannata conducted damage studies of a variety of potential membrane materials at Brookhaven and LURE. They concluded that there was no change in the internal stress of a diamond film to an absorbed dose of 8 MJ/cm

3.7 HYDROGEN CONCENTRATION

Hydrogen concentration in ten membranes was measured by Charles Evans Associates using the hydrogen forward scattering method (See Appendix 2). In this method an energetic helium beam impinges in the surface of the membrane at a shallow angle, knocking forward hydrogen atoms, which are detected. Quantitative information is obtained by reference to known standards, such as polyethylene foil. The energy distribution of the hydrogen atoms correlates to the depth from which they originate. The results of this measurement are summarized in Table 3. Figure 22 shows the hydrogen concentration in the membranes versus the methane percentage during membrane growth. The correlation is very strong, suggesting that methane percentage during membrane growth is the determining factor for hydrogen incorporation.

3.8 ABSORBER COMPATIBILITY

To investigate compatibility with metal absorber systems, wafers were covered with a dot pattern sputtered through a metal mask. The wafers were then masked and etched to form membranes. The metals used were gold and tungsten. Coating thickness was 500 nm. In each case a 20 nm titanium layer was applied first to promote adhesion.

No problems were noted with adhesion of gold or tungsten. A gold-patterned membrane is shown in Figure 23.

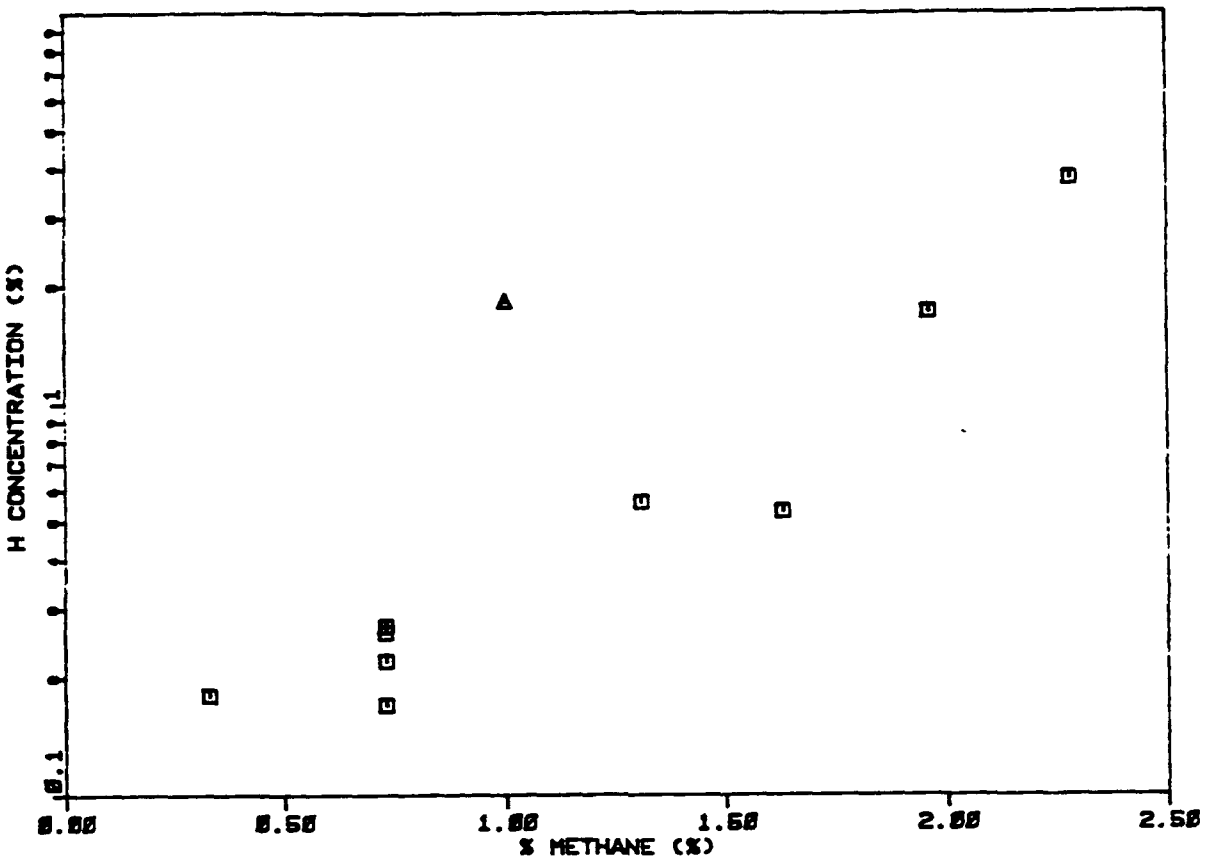

Figure 22 Hydrogen concentration in the membranes (determined by He forward scattering) vs. methane percentage utilized during membrane growth.

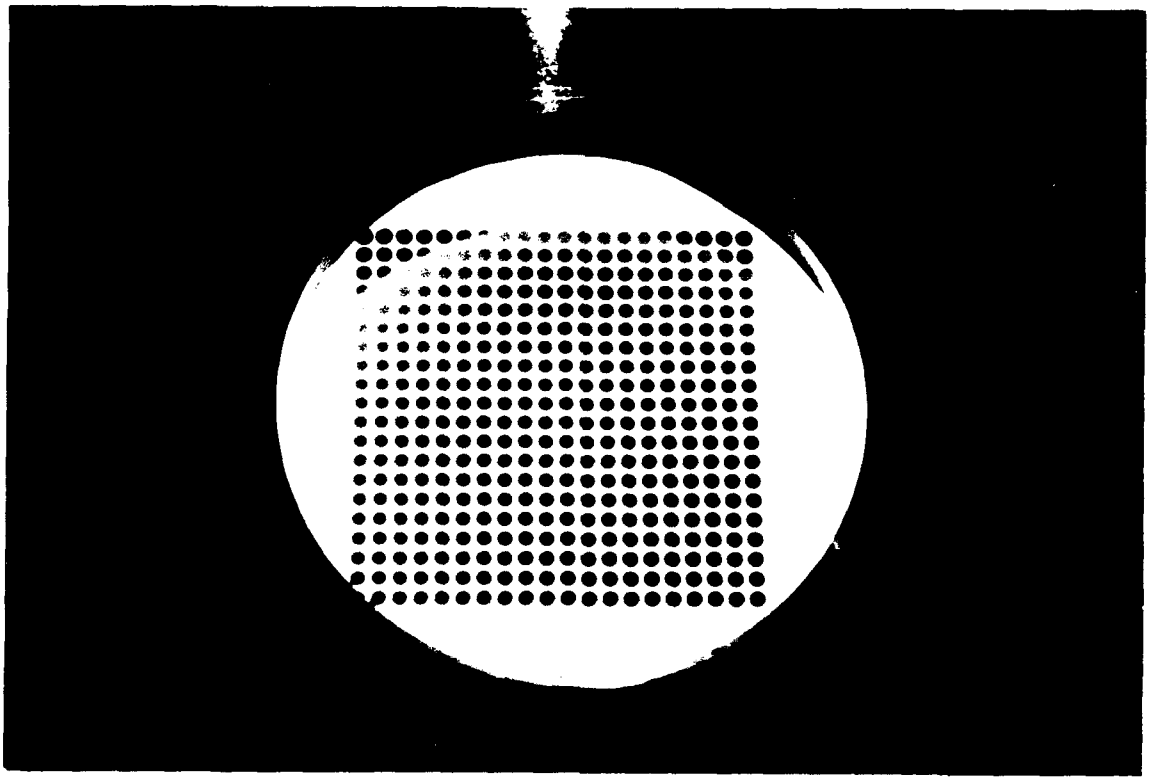

Figure 23 Photograph of membrane patterned with gold asbsorber.

4.0 SUMMARY AND CONCLUSIONS

The following is a summary of the achievements of this portion of the program:

The two-stage nucleation/growth routine first discussed in Phase I was perfected.

We improved membrane thickness uniformity by controlling the shape and position of the plasma, and by installing a wafer stage with tailored heat loss profile.

We performed comparative evaluation of different silicon wafer surface seeding treatments, arriving at a reproducible procedure to produce high density nucleation.

The role of process parameters including wafer temperature, plasma input power, methane concentration, and chamber pressure on tensile stress, grain size and optical absorption was investigated.

The residual stress and bi-axial modulus were determined for four membranes.

We obtained X-ray transmission data and an absorption map for representative membranes.

Two items have been omitted from the report:

Gas mixtures including CO and O_2 were attempted during Phase 2, but the results of these experiments were difficult to interpret at the time. The judgement was made that more rapid progress in understanding the role of process variables would be made by limiting the gas mixture components to hydrogen and methane.

An extensive set of surface profile measurements was made by Zygo using interferometric surface profiling equipment. The data from these measurements was inconsistent with the known grain sizes of the membranes investigated, and with reported data on similar membranes. This data has been eliminated.

RECOMMENDATIONS FOR FUTURE WORK

Base on the results of our work in this program and our perceptions of the needs of the industry, the following is a list of requirements for the successful development of diamond membranes for X-ray lithography masks:

Membranes should be grown on 4 inch wafers for consistency with emerging practices and to allow larger membrane diameters.

Thickness uniformity to within 5% over a 60 mm diameter should be sought.

Surface roughness should be compatible with pattern definition needs and optical scattering criteria. Smoothness criteria and specifications have to be developed.

Membranes have to be free of surface or bulk defects that would lead to physical defects in the mask metallization or to X-ray transparency inhomogenieties.

Optical absorption and scattering properties should be determined.

A residual stress specification needs to be developed and the tensile stress of the membranes controlled to within this specification.

X-ray damage resistance studies have to be extended to megadoses consistent with intended mask lifetimes.

Absorber patterning techniques have to be investigated and perfected.

Membrane failure (breakage) mechanisms should be investigated.

Manufacturing costs of diamond membranes have to be evaluated.

PHASE 3 GOALS

The following goals, selected from the list above, are recommended for Phase 3 of this program.

- Grow membranes on 4" wafers.

- Obtain uniform thickness within 5% over a 60 mm diameter

- Obtain surface roughness compatible with pattern definition and optical scattering requirements.

- Obtain membrane homogeniety/freedom from defects compatible with pattern definition requirements.

- Determine optical absorption and scattering properties of selected membranes.

FIGURE CAPTIONS

Figure 1 SEM's showing 0.1 μm diamond grit air-brushed on a silicon wafer (above), and then grown on for fourteen hours at 1.0 percent methane concentration.

Figure 2 Photograph showing two half wafers seeded by different techniques but grown side by side. The half wafer showing less growth was scratched with wet 0.1 μm diamond powder. The other was scratched with dry 0.1 μm diamond powder imbedded in a cloth lap.

Figure 3 SEM photographs comparing the edge regions of the two half-wafers shown in Figure 2.

Figure 5 Schematic drawing of the Crystallume microwave plasma deposition system.

Figure 6 Drawing of the substrate stage utilized to control the temperature profile of the wafers during depositions.

Figure 7 Approximate boundaries of the parameter space utilized for membrane depositions in the Crystallume reactors.

Figure 8 Temperature - pressure range of interest for membrane growth. The portion studied with the Crystallume reactors is enclosed in the solid lines. The points represent membranes grown for Phase 2 in an Astex reactor.

Figure 9 SEM photographs of the fractured edges of two membranes. These provide an indication of the film morphology and facilitate a precise thickness determination.

Figure 10 Typical visible - IR transmission curve for membranes produced in this program. The oscillations make possible a determination of thickness to within the accuracy that the refractive index is known.

Figure 11 Experimental determination of growth rate for two different methane concenratrations.

Figure 12 Average grain size/thickness vs. power (which correlates strongly with wafer temperature) for membranes grown in 0.73 percent methane. The rectangular "points" represent membranes found to be in

tension. This data illustrates that tensile membranes are produced at wafer temperatures somewhat higher than those that produce the minimum grain size.

Figure 13 SEM photographs of a typical membrane grown in a Crystallume reactor.

Figure 14 SEM photographs of a membrane grown under low pressure conditions in an Astex reactor.

Figure 15 Average grain size vs. thickness for membranes grown at 1300 watts in 0.73 percent methane. Average grain size is observed to increase roughly linearly with thickness. This allows us to use grain size/thickness as a measure of film quality in figures 12 and 16.

Figure 16 Grain size/thickness dependence on methane concentration.

Figure 17 Visible transmission spectra for three different membranes. Curve number 3 shows the effect of strong surface scattering on the transmission curve. This figure was provided by Dr. George Celler, Bell Labs.

Figure 18a and 18b. Typical Raman spectra for membranes grown at 1300 watts and 0.73 percent methane in the Crystallume reactors. Figure 18c. Raman spectrum for a wafer grown at 825 C, 1 percent methane in an Astex reactor.

Figure 19 The ratio of diamond to non-diamond peak heights in the Raman spectra, compared with the absorption coefficient at 600 nm, for membranes grown under a variety of conditions.

Figure 20 Energy spectra of the X-ray source at University of Wisconson. The lower spectrum was used for absorption measurements and for some of the X-ray damage study exposures. The higher spectrum was used for most of the damage study exposure.

Figure 21 Lower curve: X-ray transmission through a membrane as a function of position. Upper curve: Thickness profile of the membrane estimated from transmission measurements and interference ring count. The two are consisitent within the experimental accuracy. The implied absorption coefficient is approx. $1.3 \times 10^3 cm^{-1}$. Data provided by Greg Wells, CXrL.

Figure 22 Hydrogen concentration in the membranes (determined by He forward scattering) vs. methane percentage utilized during membrane growth.

Figure 23 Photograph of a membrane patterned with gold absorber.

APPENDIX A

RESIDUAL STRESS AND BI-AXIAL MODULUS MEASUREMENTS

NANOSTRUCTURES

Report to: Bill Phillips
Crystallume

Report on: Membrane Bulge and Scanning Optical Transmittance Measurements

P. O. No.: 2954 BP

Date: December 3, 1990

PURPOSE

The purpose of this report is to present the results of scanning optical transmittance and membrane bulge measurements of Crystallume diamond membranes. The scanning optical transmittance measurements are used to determine the thickness of the membranes. The bulge measurements give the residual stress, σ_0, and bi-axial modulus, $E/(1 - \nu)$, of the membranes. (E is the Young's modulus and ν is the Poisson's ratio).

RESULTS AND DISCUSSION

1. General

The transmittance of 11 membranes was measured. Membranes 310, 368, and 373 were classified as "light"; 356, 370, A244, and 371 as "medium"; and A242 and A243 as "dark". 349 and 369 were not classified, but their transmittance was measured for the purpose of calculating their thicknesses. Membranes 349, 369, A243, and 368 were measured on the bulge chamber. Membranes 310, 370, 371, and 373 were in compression while the others were in tension. They were approximately 1.5" in diameter.

2. Transmittance Measurements

The membranes were measured on a Perkin-Elmer Lambda 9 Scanning Spectrophotometer. The wavelength range was 400 to 2,600 nm. The measurement spot size was approximately 2 mm x 4 mm.

Thirteen spectrophotometric scans were made. The measurements were made at the centers of the membrane, near their thickest points. Two of the thirteen scans were repeats made at a lower scan speed. The transmittance at 600 nm varied between 20% and 40%. In general the hazier membranes showed smaller peak-to-peak variations. We decided to scan out to 2,600 nm in order to resolve enough peaks on the particularly hazy membranes to calculate their thicknesses. Some atmospheric absorption bands can be seen in the scans.

The membrane thickness was determined from the wavenumber intervals between adjacent maxima or minima. We used a refractive index dispersion formula derived from data compiled in E. A. Palik, Handbook of Optical Constants. We calculated the thickness from both maxima and minima, and we calculated the 1σ value for each set of measurements. The 1σ values depend on the precision with which the peak centers can be located. The precision decreases when a peak coincides with an extraneous absorption band. The results are shown in Table 1.

3. Bulge Measurements

The bulge measurement technique was described in Nanostructures' report to John Herb dated 4-2-90 (P. O. No. JH 2541).

In order to minimize the risk of breaking the membranes during the measurements, only moderate pressure differentials were applied to the membranes. The attached figure shows the

deflection of the four membranes as a function of differential pressure.

The membranes had to be mounted with the backside facing the laser beam in order to get a reflected image on the screen. The frontside of the membranes had too much surface roughness to be used as a reflecting surface.

The membrane bulge equation was derived for uniform membranes. Since the diamond membranes are not uniform, the stress and modulus calculations are likely to be in error. To minimize this error, we estimated the radial non-uniformity of the membranes from fringe counts. From these fringe counts, we then estimated the radial line average thickness and area average thickness (see Table 2). We then calculated the stress and bi-axial modulus of the four membranes (Tables 3 and 4, respectively) for each of the following three cases: (1) measured center thickness, (2) calculated line average thickness, and (3) calculated area average thickness.

We expect that the area average case is more suitable for the bulge equation than the other two models. The calculated results show that there is less than an order of magnitude stress variation among the four membranes. As may be expected there is less variation in the modulus results. The area-average results show that the bi-axial modulus is comparable to the "theoretical" diamond value of 1.3×10^{13} dyn/cm^2. The measured diamond modulus is about two times that of silicon carbide and about six times that of (100) silicon. As more uniform diamond membranes are developed, we anticipate that the reliability of the stress and modulus measurements will improve.

TABLE 1. Diamond Membrane Thickness (measured at center of membrane)

Sample	Minima		Maxima		Value for reporting purposes
	t (μm)	1Sigma (μm)	t (μm)	1Sigma (μm)	t (μm)
A242	4.09	0.32	4.10	0.27	4.1
A242 - repeated	4.09	0.32	4.14	0.34	4.1
A243	3.15	0.09	3.18	0.07	3.2
A243 - repeated	3.15	0.12	3.19	0.07	3.2
A244	2.75	0.07	2.78	0.16	2.8
9-J-310	2.70	0.10	2.74	0.06	2.7
9-J-349	4.03	0.12	4.33	0.73	4
9-J-356	3.42	0.45	3.42	0.20	3.4
9-J-368	3.02	0.14	3.05	0.10	3.1
9-J-369	2.79	0.13	2.83	0.13	2.8
9-J-370	2.70	0.10	2.74	0.06	2.7
9-J-371	2.28	0.04	2.31	0.07	2.3
9-J-373	2.78	0.08	2.90	0.09	2.8

TABLE 2. Estimates of Average Membrane Thickness

Sample	No. of fringes across wafer	No. of fringes across membrane	Measured Membrane Thickness at center of membrane	Calculated Membrane Thickness Variation	Calculated Membrane Thickness at edge of membrane	Line Average Thickness (Radial)	Area Average Thickness
	nw	nm	tc (μm)	$\Delta t = tc*nm/nw$ (μm)	$te = tc - \Delta t$ (μm)	$(tc+te)/2$ (μm)	$tc - \Delta t/\sqrt{2}$ (μm)
A243	28	8	3.2	0.90	2.30	2.80	2.60
9-J-349	39	12	4	1.20	2.80	3.40	3.20
9-J-368	28	8	3.1	0.90	2.20	2.70	2.50
9-J-369	23	7	2.8	0.90	1.90	2.40	2.20

TABLE 3. Estimates of Membrane Stress

Sample	Center Thickness (μm)	Tensile Stress dyn/cm2	Line Average Thickness (μm)	Tensile Stress dyn/cm2	Area Average Thickness (μm)	Tensile Stress dyn/cm2
A243	3.2	1.3E+09	2.8	1.5E+09	2.6	1.6E+09
9-J-349	4	1.9E+09	3.4	2.3E+09	3.2	2.4E+09
9-J-368	3.1	3.1E+08	2.7	3.6E+08	2.5	3.8E+08
9-J-369	2.8	4.5E+08	2.4	5.3E+08	2.2	5.7E+08

TABLE 4. Estimates of Membrane Bi-Axial Modulus

Sample	Center Thickness (μm)	Bi-Axial Modulus E/(1 - v) dyn/cm2	Line Average Thickness (μm)	Bi-Axial Modulus E/(1 - v) dyn/cm2	Area Average Thickness (μm)	Bi-Axial Modulus E/(1 - v) dyn/cm2
A243	3.2	6.7E+12	2.8	7.6E+12	2.6	8.2E+12
9-J-349	4	8.9E+12	3.4	1.1E+13	3.2	1.1E+13
9-J-368	3.1	7.5E+12	2.7	8.6E+12	2.5	9.3E+12
9-J-369	2.8	8.4E+12	2.4	9.8E+12	2.2	1.1E+13

MEMBRANE BULGE

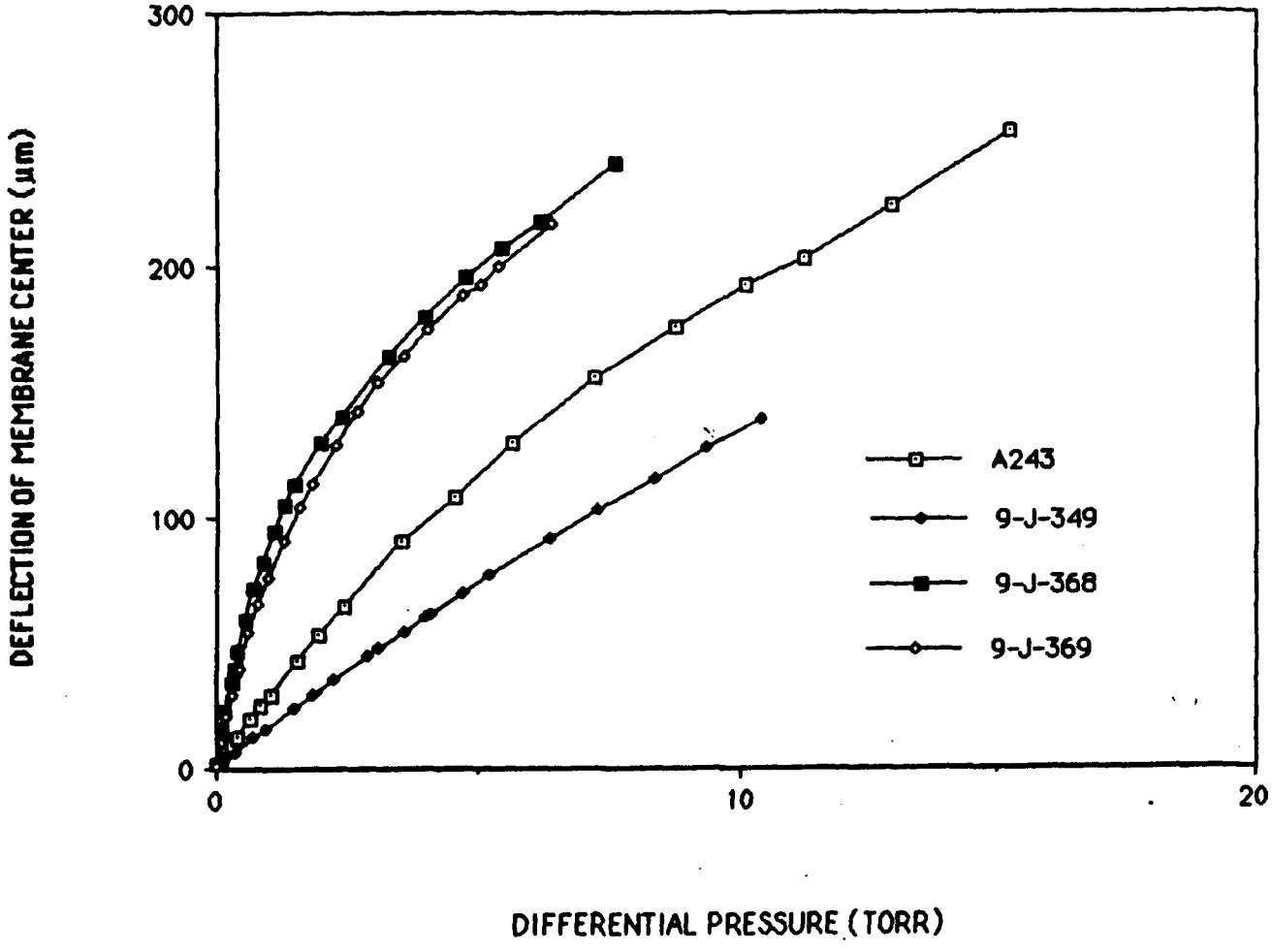

X: USER009 ; absc 2600.0- 400.0; pts 2201; int 1.00; ord 3.1250-250.00; T
inf: 05:14:10 90/11/28

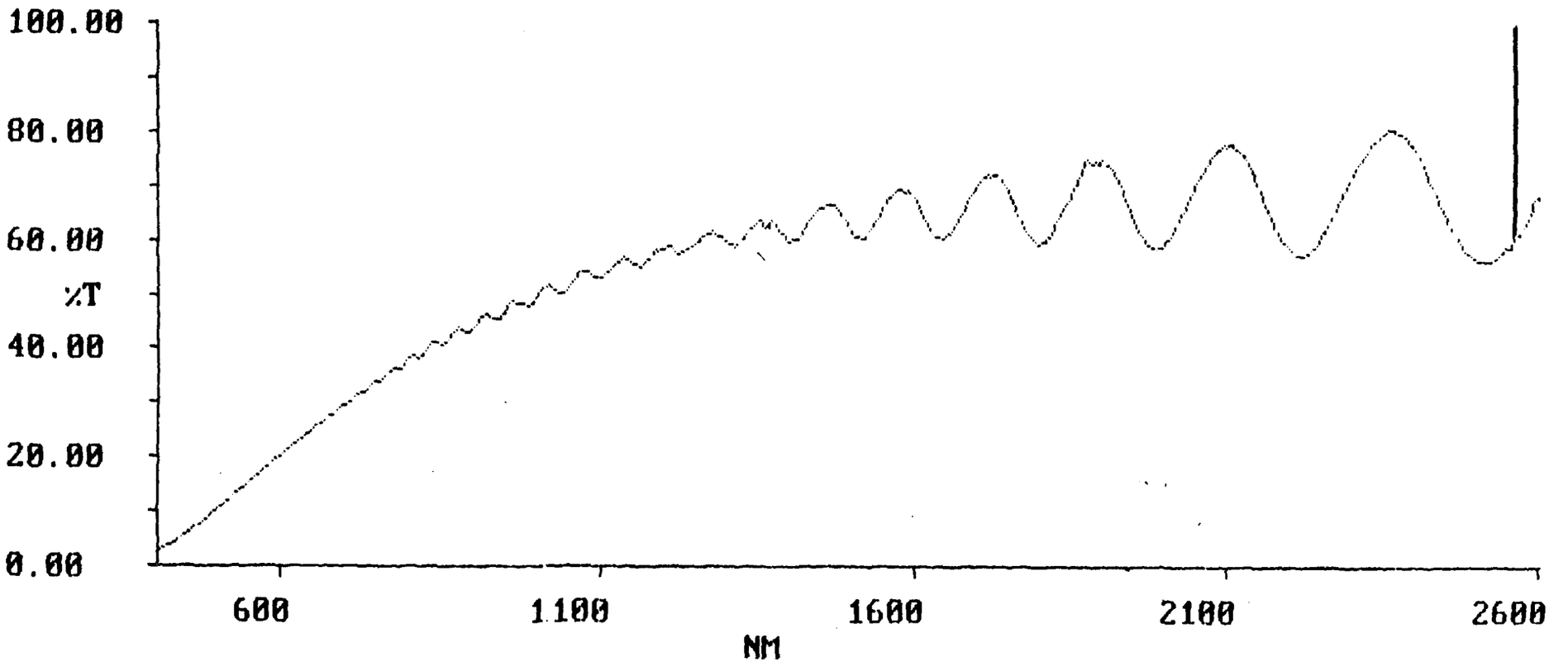

X: USER015 ; absc 2600.0- 400.0; pts 2201; int 1.00; ord 3.0450-250.00; T
inf: 06:21:22 90/11/28

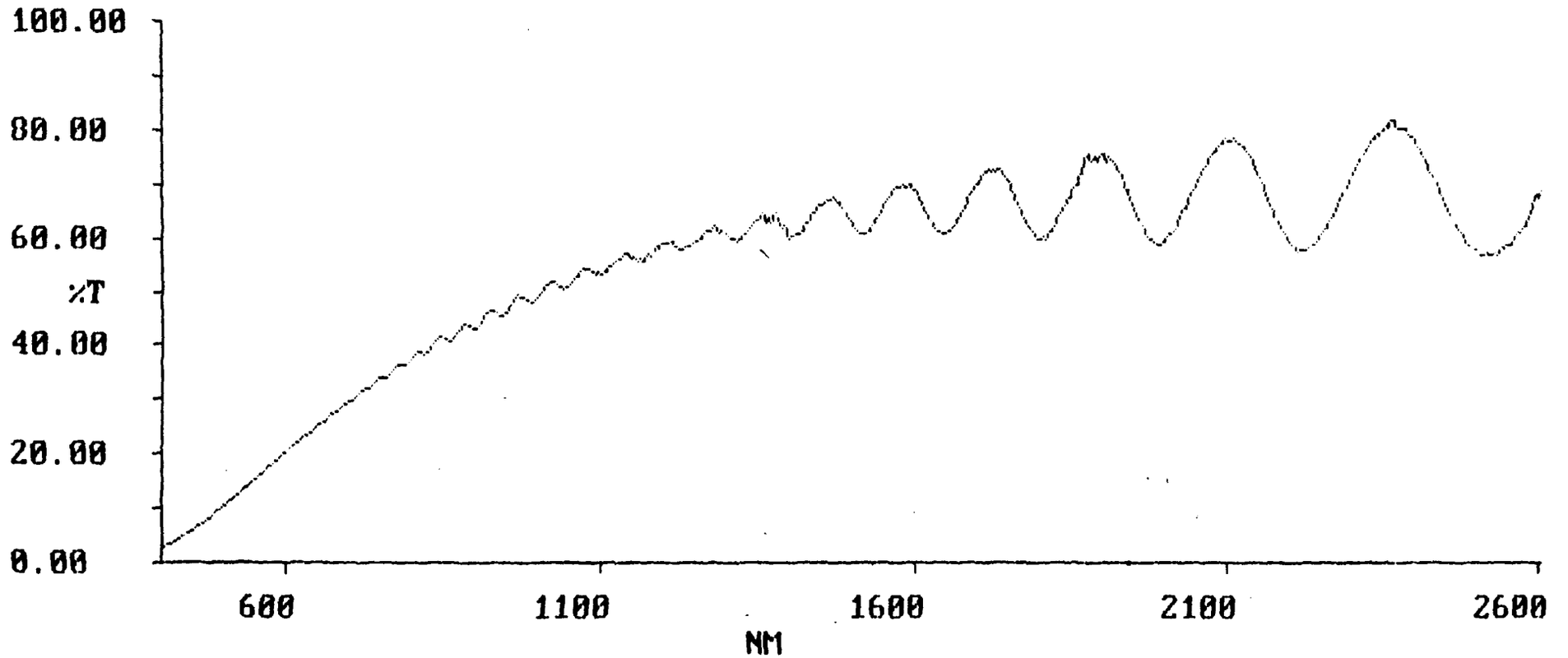

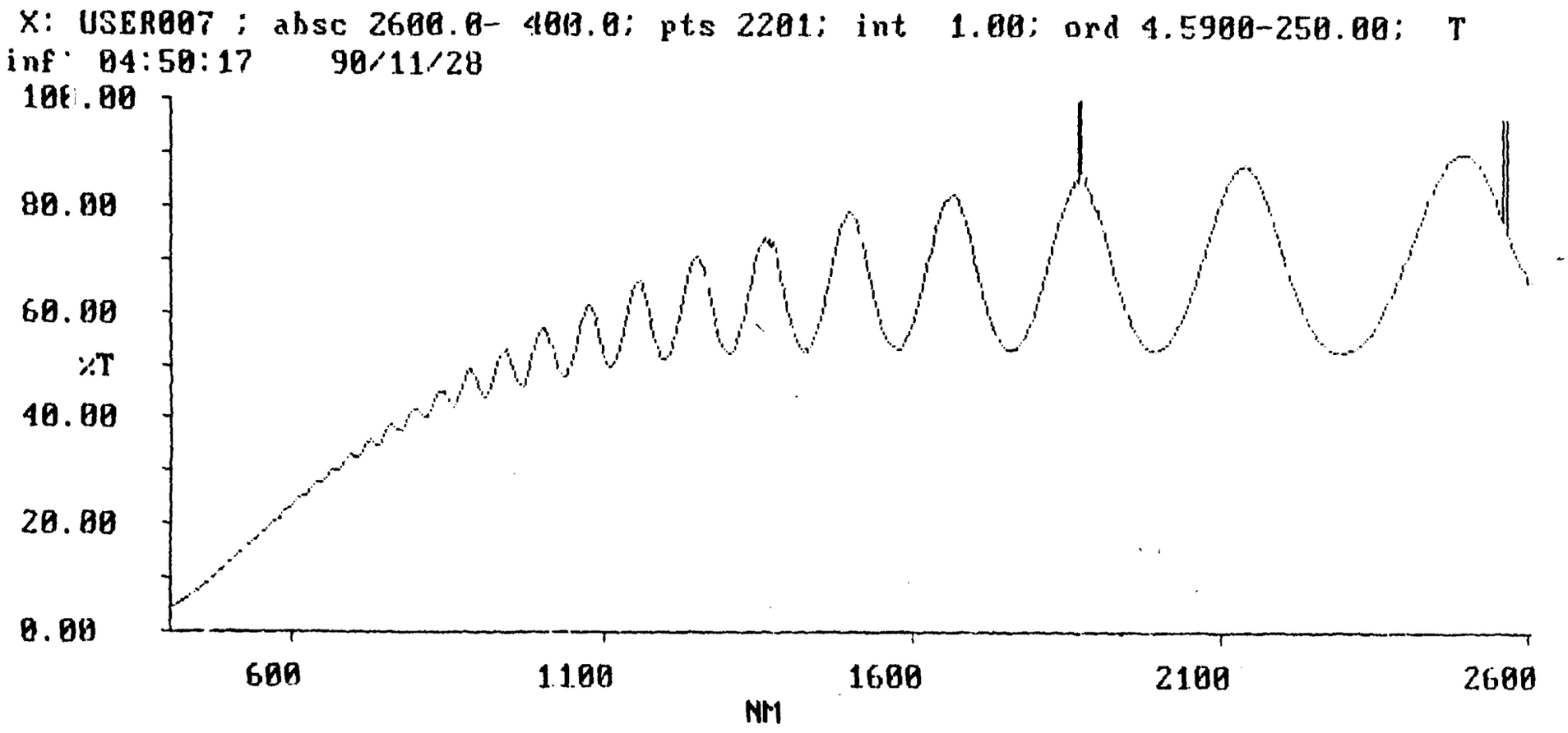
X: USER007 ; absc 2600.0- 400.0; pts 2201; int 1.00; ord 4.5900-250.00; T
inf 04:50:17 90/11/28
100.00
80.00
60.00
%T
40.00
20.00
0.00
600
1100
1600
2100
2600
NM

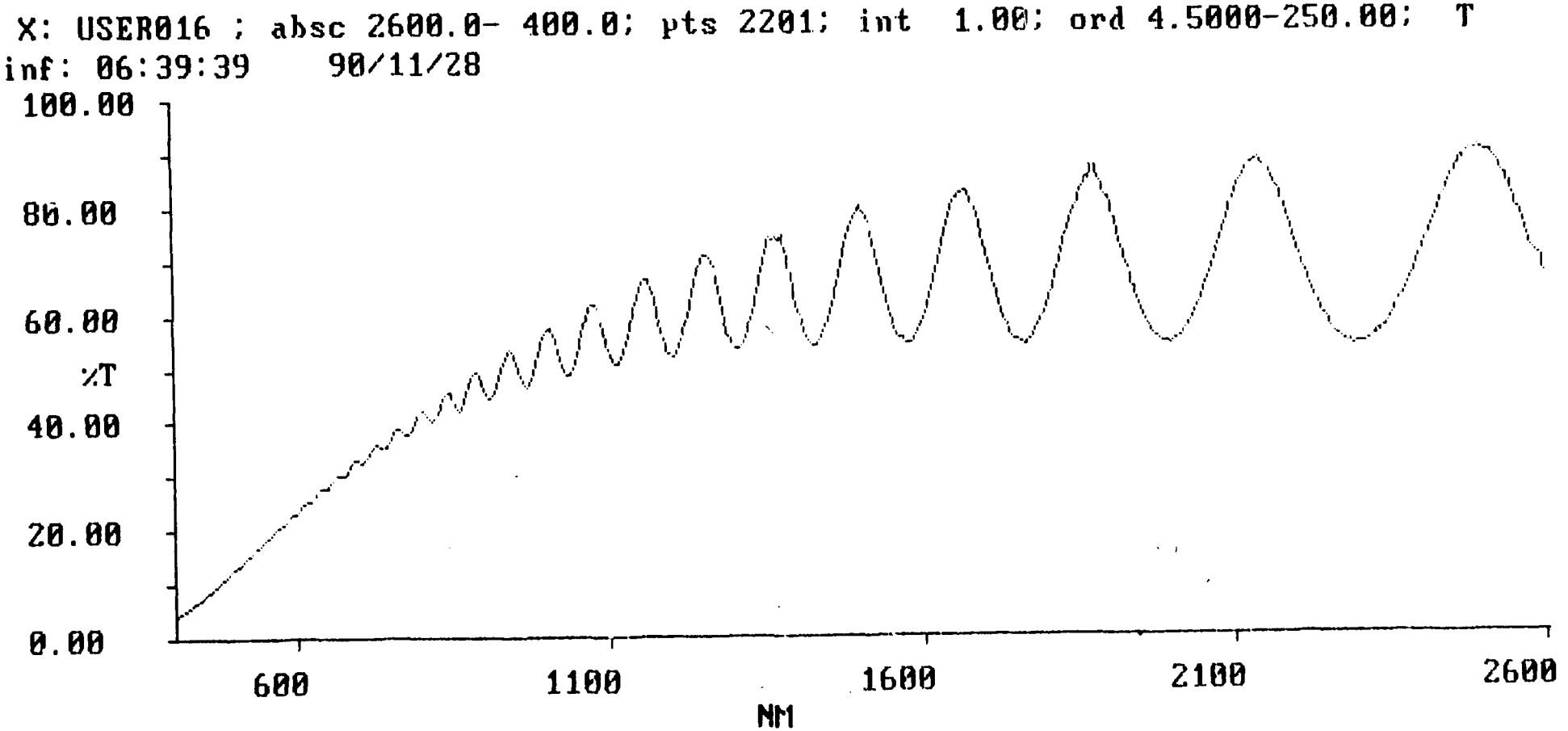
X: USER016 ; absc 2600.0- 400.0; pts 2201; int 1.00; ord 4.5000-250.00; T
inf: 06:39:39 90/11/28
100.00
80.00
60.00
%T
40.00
20.00
0.00
600
1100
1600
2100
2600
NM

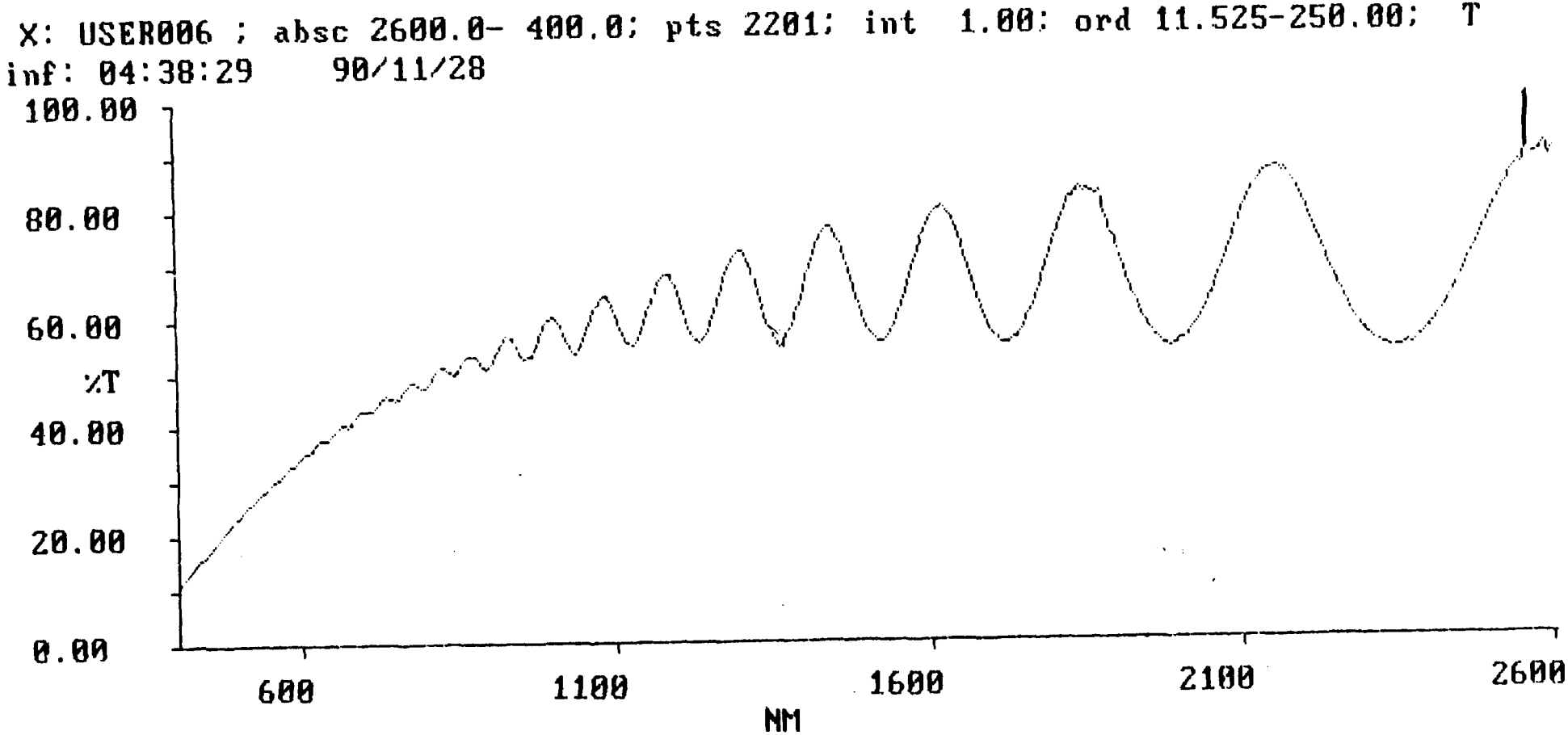
X: USER006 ; absc 2600.0- 400.0; pts 2201; int 1.00: ord 11.525-250.00; T
inf: 04:38:29 90/11/28
100.00
80.00
60.00
%T
40.00
20.00
0.00
600
1100
1600
2100
2600
NM

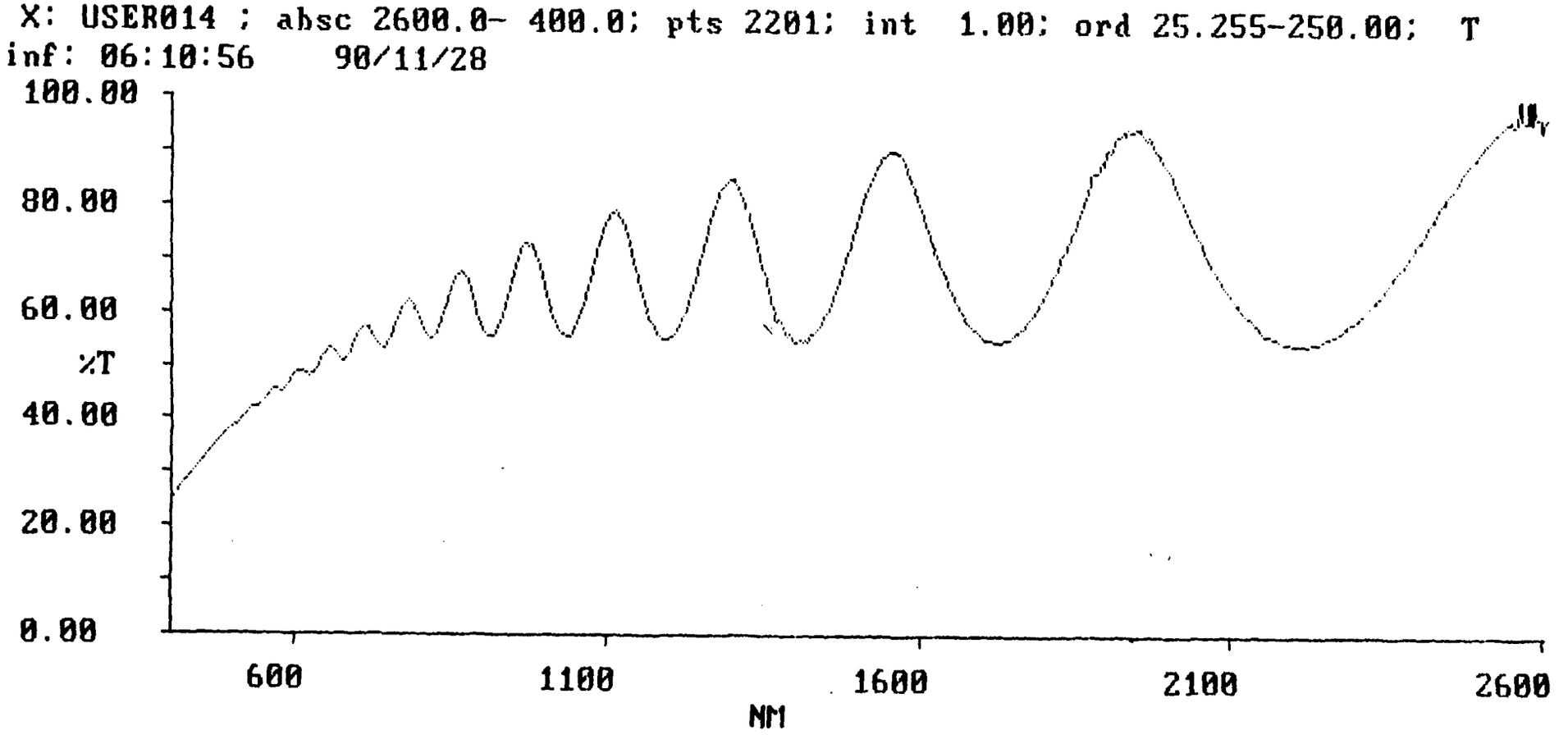
X: USER014 ; absc 2600.0- 400.0; pts 2201; int 1.00; ord 25.255-250.00; T
inf: 06:10:56 90/11/28
100.00
80.00
60.00
%T
40.00
20.00
0.00
600
1100
1600
2100
2600
NM

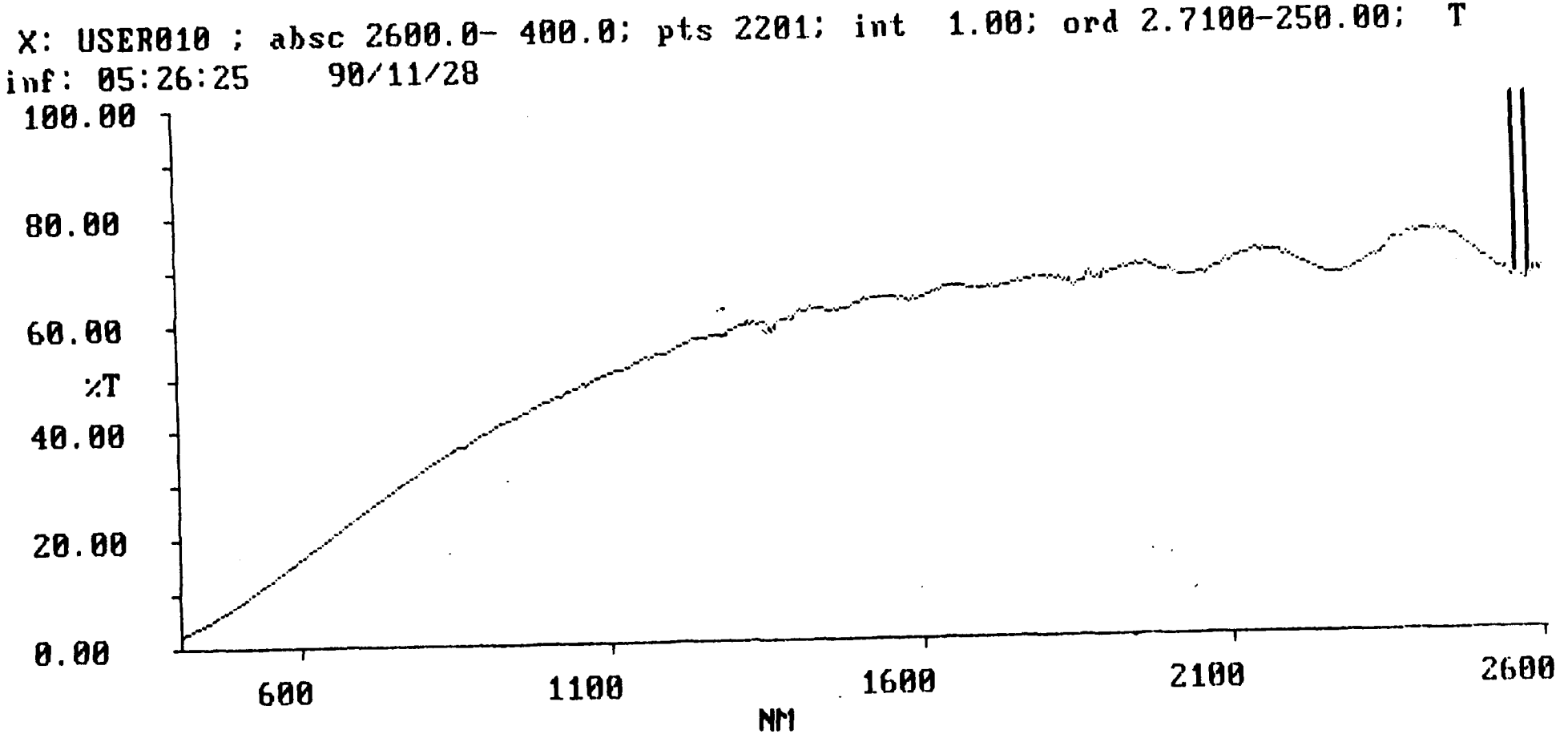
X: USER010 ; absc 2600.0- 400.0; pts 2201; int 1.00; ord 2.7100-250.00; T
inf: 05:26:25 90/11/28
100.00
80.00
60.00
%T
40.00
20.00
0.00
600
1100
1600
2100
2600
NM

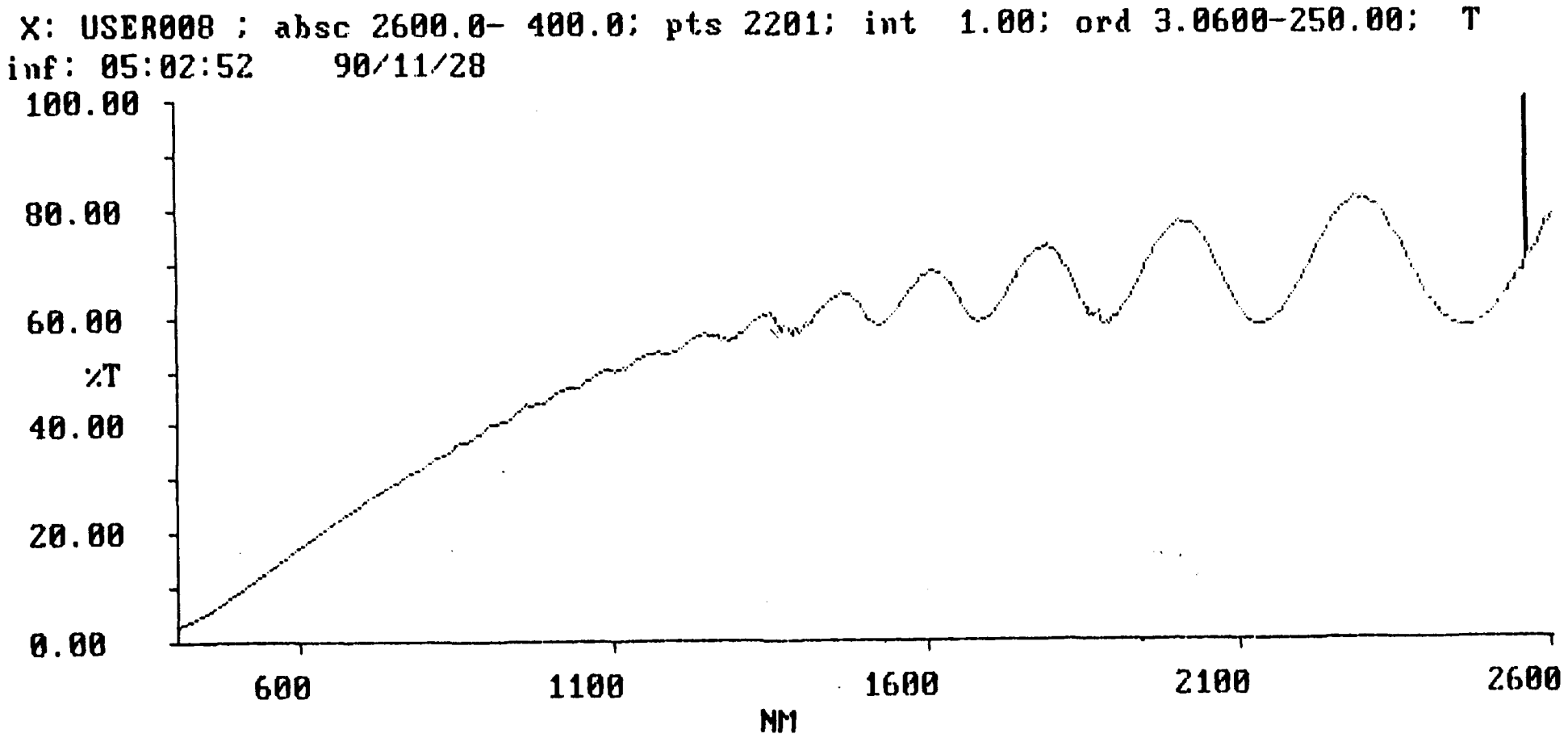
X: USER008 ; absc 2600.0- 400.0; pts 2201; int 1.00; ord 3.0600-250.00; T
inf: 05:02:52 90/11/28
100.00
80.00
60.00
%T
40.00
20.00
0.00
600
1100
1600
2100
2600
NM

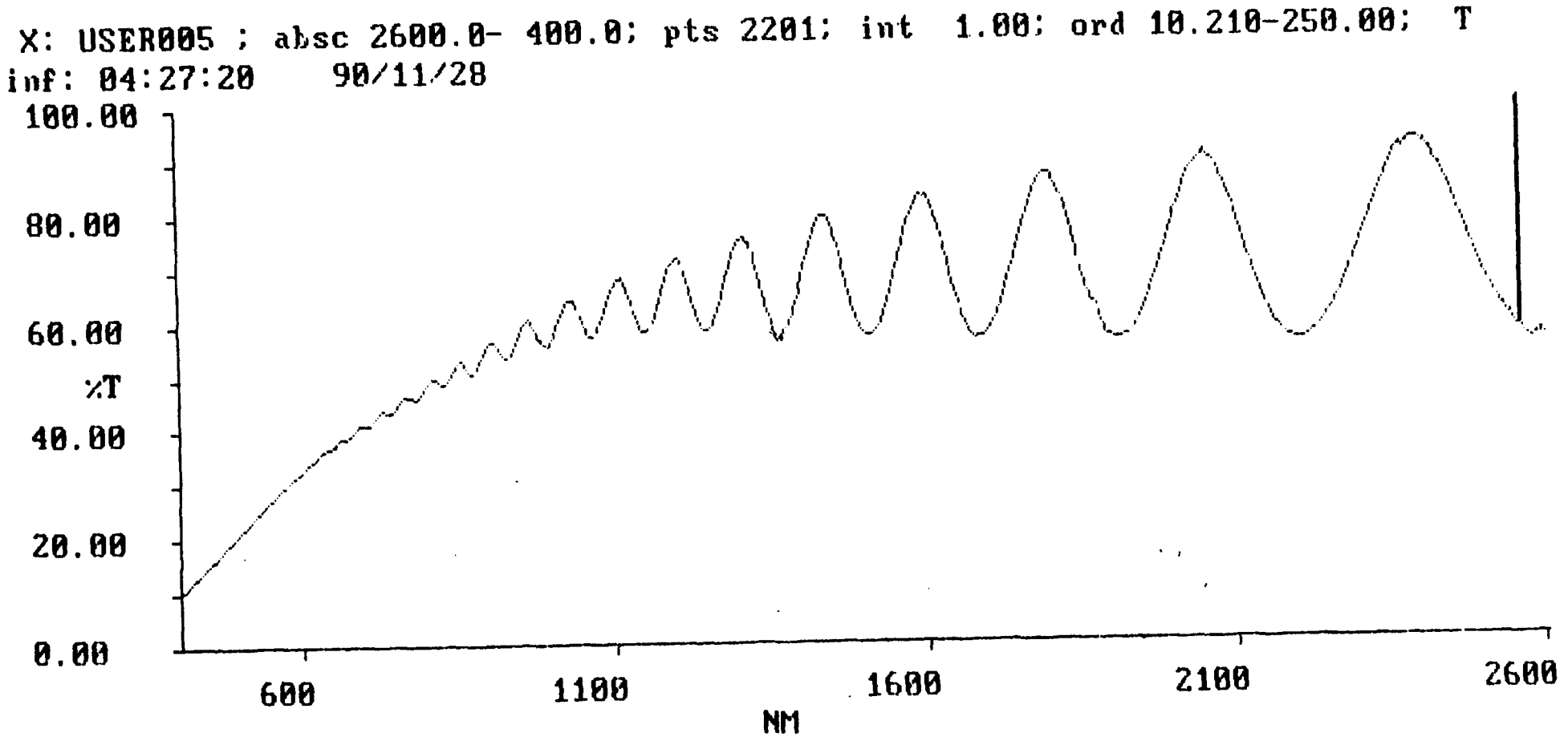
X: USER005 ; absc 2600.0- 400.0; pts 2201; int 1.00; ord 10.210-250.00; T
inf: 04:27:20 90/11/28
100.00
80.00
60.00
%T
40.00
20.00
0.00
600
1100
1600
2100
2600
NM

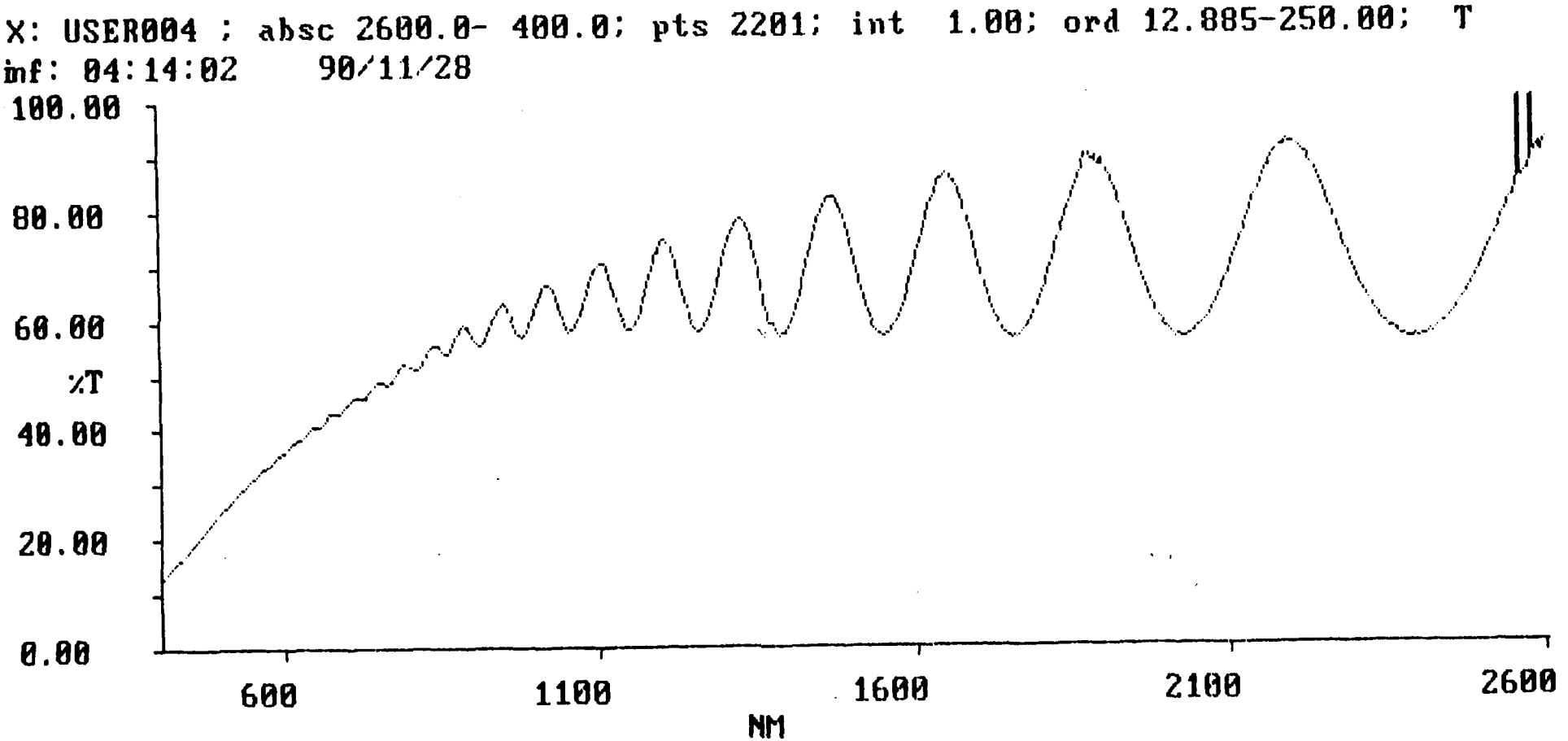
X: USER004 ; absc 2600.0- 400.0; pts 2201; int 1.00; ord 12.885-250.00; T
inf: 04:14:02 90/11/28
100.00
80.00
60.00
%T
40.00
20.00
0.00
600
1100
1600
2100
2600
NM

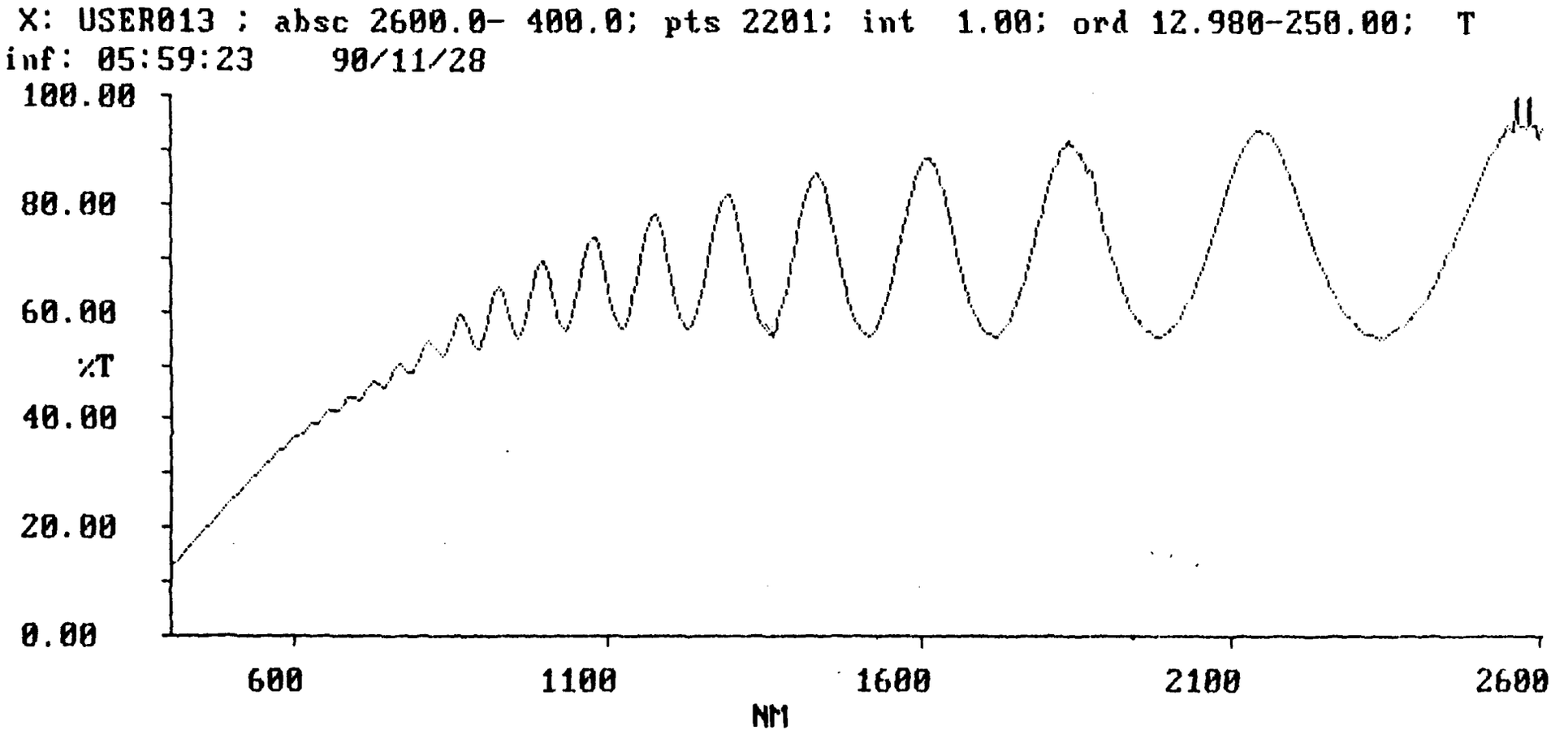
X: USER013 ; absc 2600.0- 400.0; pts 2201; int 1.00; ord 12.980-250.00; T
inf: 05:59:23 90/11/28
100.00
80.00
60.00
%T
40.00
20.00
0.00
600
1100
1600
2100
2600
NM

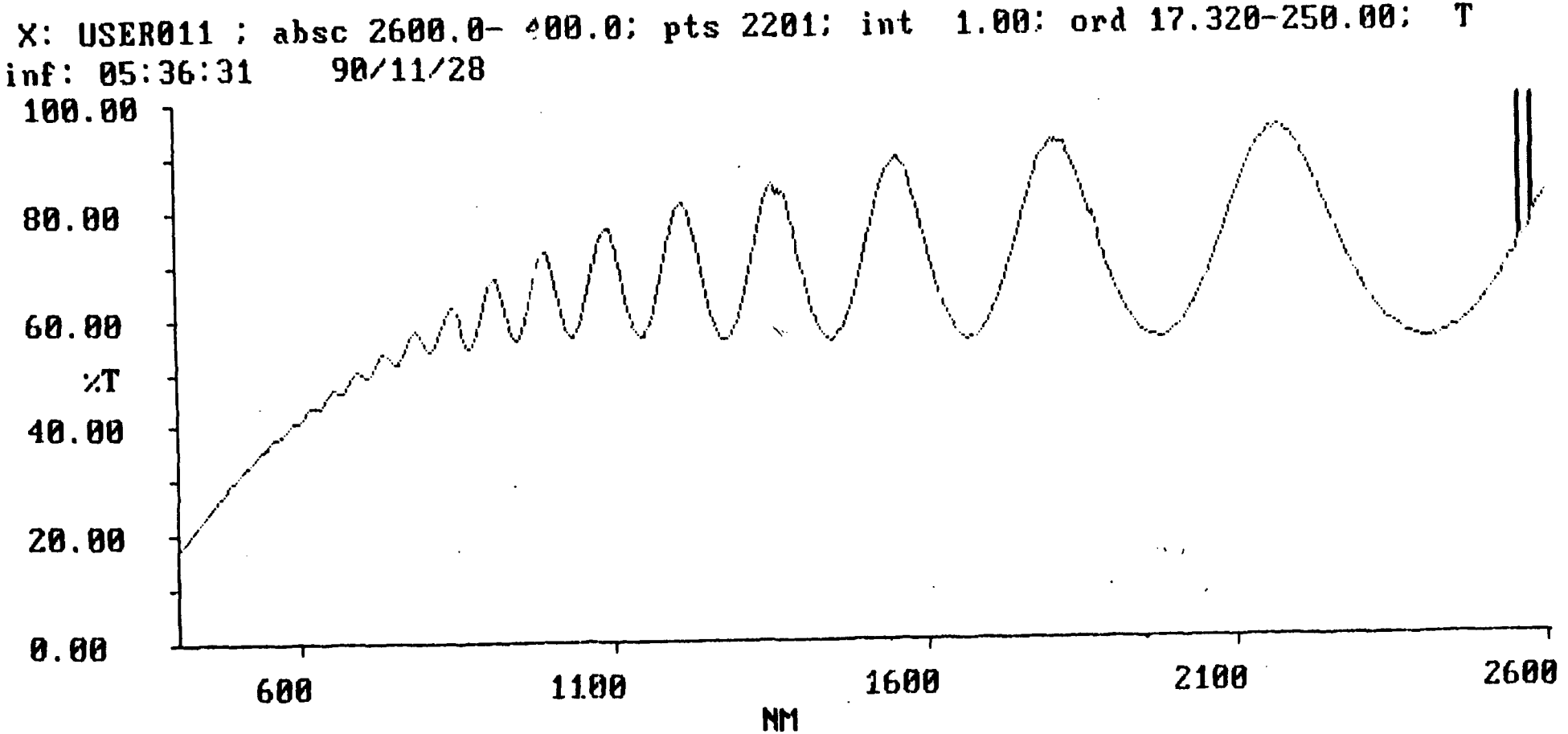
X: USER011 ; absc 2600.0- 400.0; pts 2201; int 1.00: ord 17.320-250.00; T
inf: 05:36:31 90/11/28
100.00
80.00
60.00
%T
40.00
20.00
0.00
600
1100
1600
2100
2600
NM

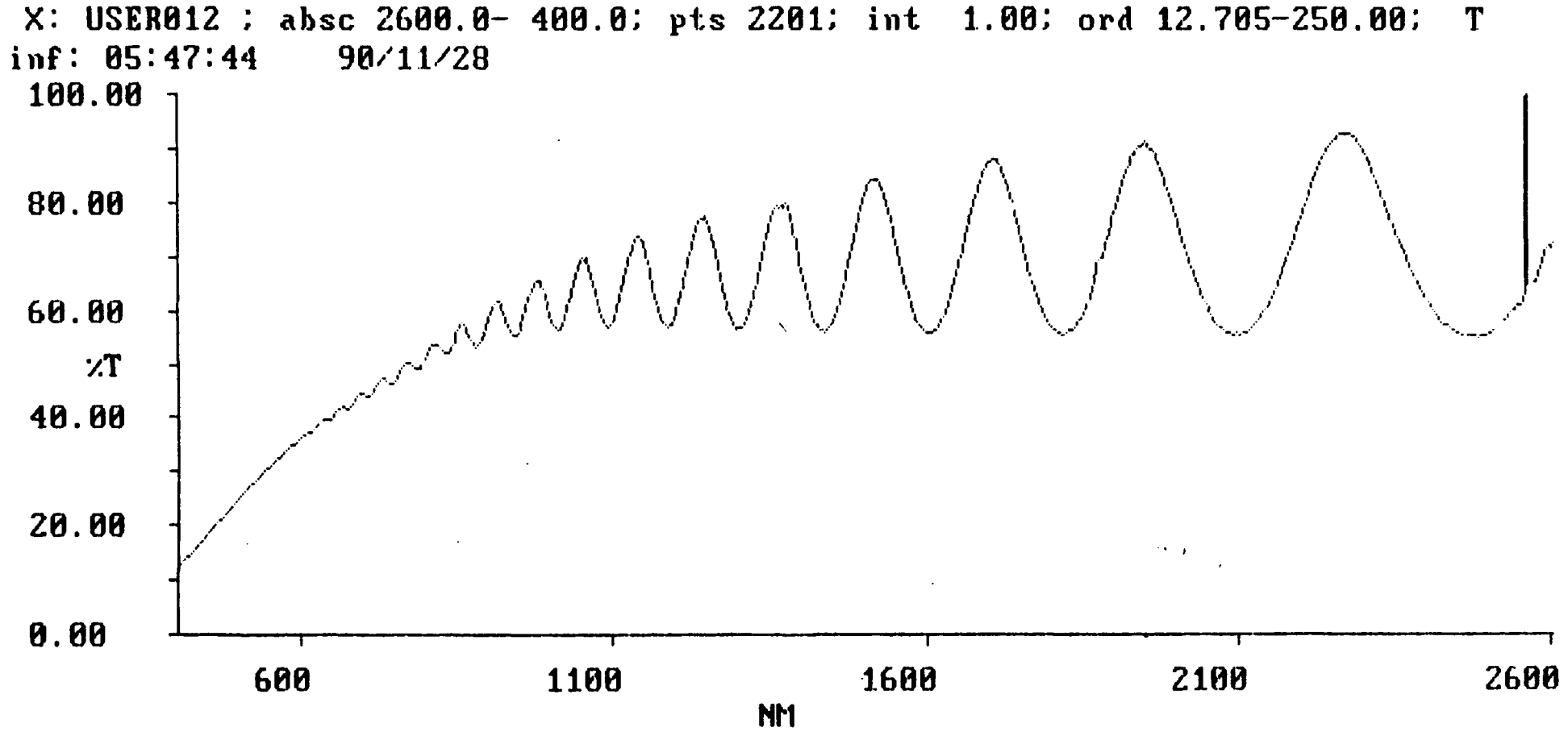
X: USER012 ; absc 2600.0- 400.0; pts 2201; int 1.00; ord 12.705-250.00; T
inf: 05:47:44 90/11/28
100.00
80.00
60.00
%T
40.00
20.00
0.00
600
1100
1600
2100
2600
NM

APPENDIX B

HYDROGEN ANALYSIS

CHARLES EVANS AND ASSOCIATES

CHARLES EVANS & ASSOCIATES

SPECIALISTS IN MATERIALS CHARACTERIZATION

December 11, 1990

Bill Phillips
Crystallume
125 Constitution Drive
Menlo Park, CA 94025

Subject: RBS ANALYSIS
CE&A Number: 21485
Your Purchase Order No.: 3144BP

Dear Dr. Phillips:

Enclosed are the results of Hydrogen Forward Scattering analysis of ten samples. Also enclosed is a packing slip which should be forwarded to your accounts payable department. If there are any questions concerning this report, or if I can assist you in any way, please contact me.

Sincerely,

Scott Baumann
Manager, RBS Services

enclosures

301 Chesapeake Drive • Redwood City • CA • 94063 • (415) 369-4567 • Telex 172747 • Fax (415) 369-7921

RUTHERFORD BACKSCATTERING LABORATORY REPORT

Requestor:	Bill Phillips
Purchase Order No:	3144BP
CE&A Job No:	214857
Analysis Date:	December 6, 1990

Purpose: The purpose of this analysis was to determine the hydrogen concentration in carbon films on ten samples.

Analytical Conditions:

He^{++} *ion beam energy*	2.275 MeV
RBS Detector Angle	160°
HFS Detector Angle	30°

General: Included are HFS spectra which have been plotted full scale and overlaid in order to allow comparison between the samples. Also included are the unprocessed HFS and RBS data which were numerically listed and plotted on two scales.

Results: The results of this analysis are presented in the attached figures listed below and in Table 1 which lists the H concentration in each sample at two depths. There is an uncertainty of ±10% in the H concentrations, except for the samples with H concentrations below 0.5 atom percent. Since the H detection limit is approximately 0.05 atom percent for these samples, there is an uncertainty ±0.05 atom percent for the H concentrations which are below 0.5 atom percent.

Discussion: In order to obtain the most accurate results for HFS analyses it is necessary to know the concentrations of other elements which are present in the sample. In this case the samples were assumed to consist of C and H only. Inspection of the RBS spectra obtained from these samples shows that no elements heavier than C are present at concentrations above 0.1 atom percent in the bulk of the C films. S and Si were detected on the surfaces of samples 373, 306, 356, and 243 at trace concentrations (approximately 5×10^{14} atoms/cm^2).

Shown in Figure A is a schematic showing the experimental arrangement for the HFS measurement. By placing a detector such that it is located 30 degrees from the forward trajectory of the He^{++} ion beam, and by rotating the samples so that their planer surfaces are 15 degrees from the forward beam, it is possible to collect hydrogen which is scattered forward out of the samples after collisions with the probing He^{++} ion beam. A thin aluminum foil is placed over the detector to filter out He atoms which are also scattered from the sample. Presently hydrogen concentrations are determined by comparing the number of hydrogen counts obtained from the sample of interest to the number of hydrogen counts

obtained from a reference sample after normalizing by the stopping powers of the different films. The reference sample is a mineralogical sample called phlogopite which has had its hydrogen concentration measured by the United States Geological Survey. Also analyzed as a reference was a polyethylene sample which has a nominal stoichiometry of CH_2. Using the phlogopite sample as a reference produces calculated H concentrations of 69% H at 3,300 Angstroms in depth and 66% H at 4,500 Angstroms in depth in the polyethylene sample. This indicates that the phlogopite does serve as an accurate reference.

Since the compositions of samples vary, it follows that the stopping powers for He and H atoms in different films will also vary, and thus the depth which is sampled in a given film will vary from sample to sample. This relates directly to the number of hydrogen counts which will be accumulated for each sample. In order to correct for this effect, the number of hydrogen counts obtained from each sample can be normalized by the estimated stopping power for its respective film. A film consisting of heavy elements will have greater stopping power than a film made of light elements. Thus the thickness which is sampled for the film made of heavy elements will be less than for the film made of light elements. For two films with equal hydrogen concentrations the film containing light elements will produce more hydrogen forward scattering events per channel than a film consisting of heavy elements. Normalizing by the stopping power (referred to as ϵ_B or epsilon) for each film compensates for this effect. The method used to calculate the hydrogen content in the film is listed in appendix A. In this case ϵ_B (epsilon) values corresponding to carbon C were used for each sample, except the phlogopite reference sample. In the case of the phlogopite sample the stoichiometry listed in Table 2 was used to determine its ϵ_R (epsilon) value.

Shown in Figure 1 are the overlaid HFS spectra from the five samples having bulk H concentrations above 0.5 atom percent. Shown in Figures 2 and 3 are the overlaid HFS spectra from the five samples having bulk H concentrations below 1 atom percent with the exception of sample 359. This shows the relatively wide range of H concentrations found in these samples. Similar to RBS, counts at higher channels correspond to hydrogen scattered from the surface of the samples, while counts at lower energies correspond to hydrogen scattered from greater depths in the samples. In this case the hydrogen counts are present down to channel 50 where they are suppressed by the detector discrimination system. This indicates that less than the entire film thickness is being probed for all of these samples. It should be noted that data collected from untreated samples indicate the presence of hydrogen on the surface of the samples. This hydrogen apparently comes from a thin organic layer deposited on the surface of each sample during the analysis in the turbo-pumped vacuum chamber. In order to avoid these surface H counts the average heights of the HFS spectra for these samples were measured over channels 200-300 and 100-200 which

corresponds to a depths of roughly 3,300 and 4,500 Angstroms in the carbon films.

Shown in Figures 4 through 15 are the 40 microCoulomb spectra from each sample including the two reference samples (Figures 4 and 5). Listed in each figure are the H concentrations calculated at depths of approximately 3,300 and 4,500 Angstroms in each sample. In some cases Slightly lower H concentrations were obtained at greater depths in the films. This may be due to a slight contribution of the surface H on these samples to the calculated bulk H concentrations. In order to calculate the approximate depths which are listed in Table 1 it was necessary to assume a density for each sample. In this case a density of 1.12×10^{23} atoms/cm^3 was used. For more information regarding RBS density assumptions please see the enclosed note titled "The Effect of Sample Density on Thicknesses Obtained by RBS".

Shown in Figures 16-25 are the HFS spectra which were obtained from each sample using 1, 5, and 40 microCoulombs of incident He^{+2} ions. The 1, and 5 microCoulomb spectra have been smoothed using a 7-point smoothing routine in order to reduce the noise in the spectra. Inspection of these spectra shows that for samples 348, 359, 361, 358, 360, and 378 there is a significant buildup of H on the surfaces of the samples (above channel 300) during the 40 microCoulomb and 5 microCoulomb analyses. Below channel 300 the 1, 5, and 40 microCoulomb spectra are basically identical. In the case of samples 373, 306, 356, and 243 there is a significant enrichment of the surface H, even in the 1 microCoulomb spectra. This appears to indicate that there was some surface enrichment of H on these samples, prior to the HFS analysis. These four samples all have suspended C films, and have had the Si substrates etched from beneath the C films. The etching process or other processing of these samples may be related to this surface H enrichment, or the fact that there is no Si substrate beneath these films may affect the deposition of hydrocarbon on the films during the HFS analysis.

Table 1: The H concentration in each sample at approximate depths of 3,300 and 4,500 Angstroms.

Table 2: Composition of the phlogopite reference sample that was used as a hydrogen reference (composition provided by United States Geological Survey).

Appendix 1: The formula used to obtain the hydrogen concentrations for these samples.

Figure A: Schematic showing the sample and detector arrangement for HFS analysis.

Figure 1: The overlaid 40 microCoulomb HFS spectra from the samples with bulk H concentration above 0.5 atom percent.

Figures 2-3: The overlaid 40 microCoulomb HFS spectra from the samples with bulk H concentration below 1 atom percent (sample 359 is omitted).

Figures 4-5: The 40 microCoulomb HFS spectra from the phlogopite and polyethylene reference samples.

Figures 5-15: The 40 microCoulomb HFS spectra from each sample.

Figure 16-25: The overlaid 1, 5, and 40 microCoulomb HFS spectra from each sample.

Figure 26-37: The unprocessed 40 microCoulomb HFS data from each sample.

Figure 38-47: The unprocessed 1 microCoulomb HFS data from each sample.

Figure 48-57: The unprocessed 5 microCoulomb HFS data from each sample.

Figure 58-67: The unprocessed RBS data acquired from each sample at a detector angle of 160°.

Table 1

Sample	H concentration at 3,300 Angstroms	H concentration at 4,500 Angstroms
348	0.22%	0.16%
359	0.53%	0.50%
361	0.56%	0.52%
358	1.71%	1.72%
360	3.75%	3.79%
378	0.27%	0.27%
373	0.26%	0.26%
306	0.18%	0.14%
356	0.17%	0.16%
243	1.83%	1.82%
Polyethylene	69%	66%

Table 2
Elemental Composition of Phlogopite

element	atomic %
O	54.0
Si	13.2
Mg	12.9
Al	5.5
H	5.8
K	4.2
F	3.3
Fe	0.5
Na	0.3
Ti	0.3

Characterized samples provided by United States Geological Survey.

Appendix 1
Hydrogen Calculation Method

$H_R = C * m_R/\varepsilon_R$ (eqn. 1)

$m = \varepsilon_B / (C/H_A - \varepsilon_H + \varepsilon_B)$ (eqn. 2)

Where:

H_R = Height of the hydrogen signal of the reference material.

m_R = Hydrogen concentration for the reference sample.

ε_R = Stopping cross-section of the reference material.

H_A = Height of the hydrogen signal for the sample of interest.

C = Proportionality constant (this assumes that the scattering angle, hydrogen cross section, detector solid angle, ion dose, and KeV/channel are fixed).

m = Hydrogen concentration for the sample of interest.

ε_H = Stopping cross-section of hydrogen.

ε_B = Stopping cross-section computed from the remaining elements in the matrix for the sample of interest.

As derived using equations 3.70, 3.57 and 2.50 from BACKSCATTERING SPECTROMETRY by Chu, Mayer, and Nicolet.

FIGURE 1

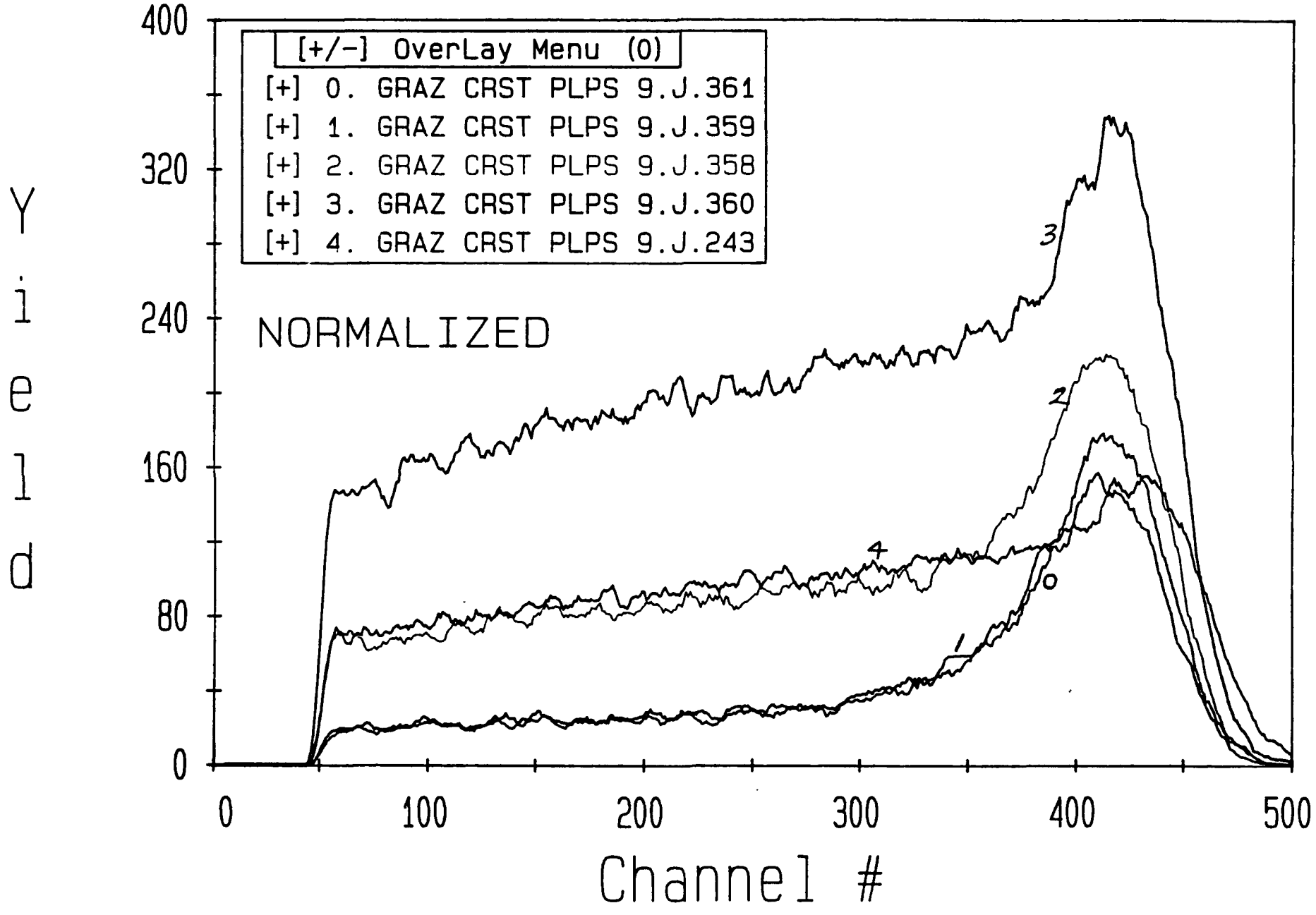
[+/-] OverLay Menu (0)
[+] 0. GRAZ CRST PLPS 9.J.361
[+] 1. GRAZ CRST PLPS 9.J.359
[+] 2. GRAZ CRST PLPS 9.J.358
[+] 3. GRAZ CRST PLPS 9.J.360
[+] 4. GRAZ CRST PLPS 9.J.243
NORMALIZED
Yield
400
320
240
160
80
0
0
100
200
300
400
500
Channel #
3
2
4
0
1

FIGURE 2

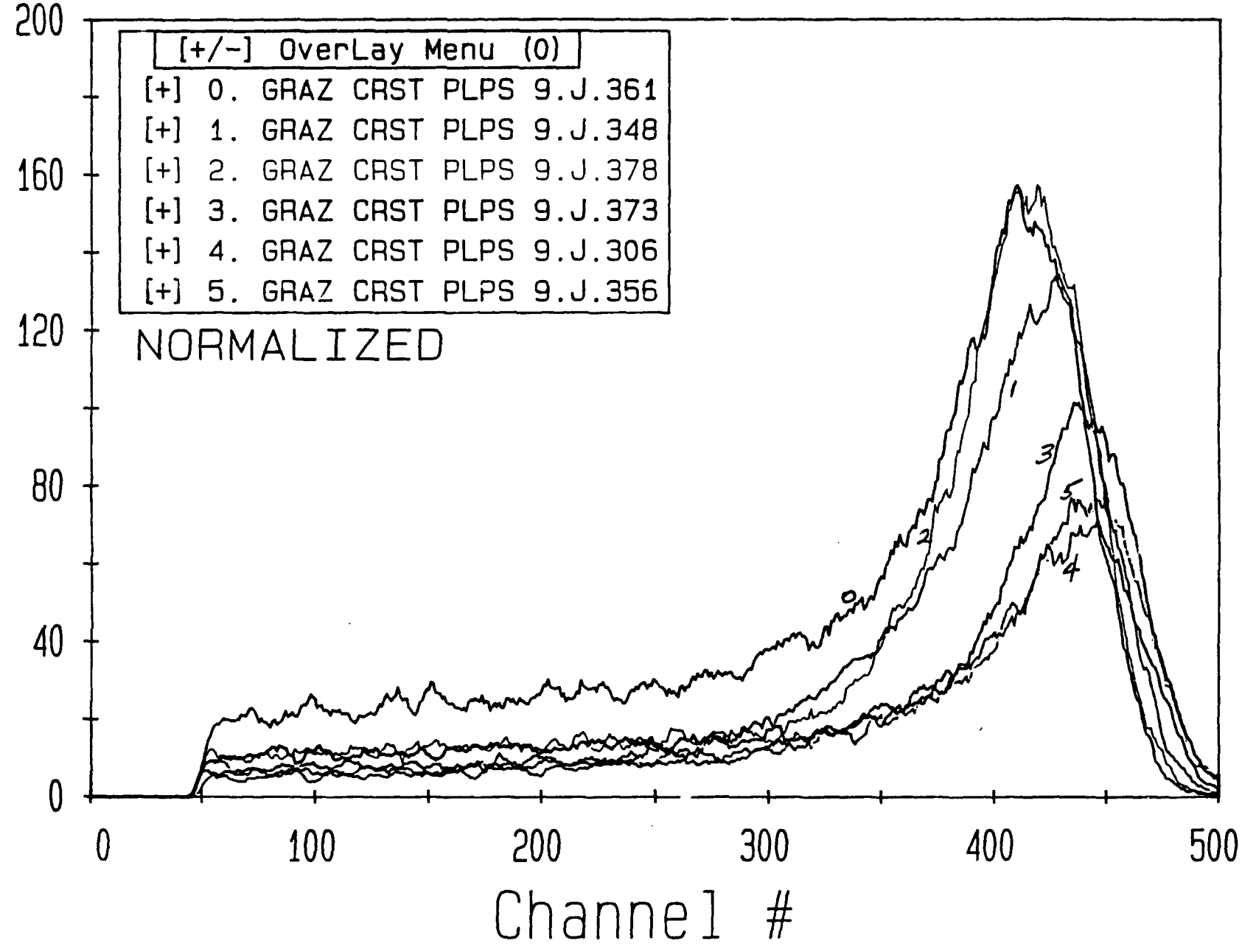
[+/-] OverLay Menu (0)
[+] 0. GRAZ CRST PLPS 9.J.361
[+] 1. GRAZ CRST PLPS 9.J.348
[+] 2. GRAZ CRST PLPS 9.J.378
[+] 3. GRAZ CRST PLPS 9.J.373
[+] 4. GRAZ CRST PLPS 9.J.306
[+] 5. GRAZ CRST PLPS 9.J.356
NORMALIZED
Yield
200
160
120
80
40
0
0
100
200
300
400
500
Channel #

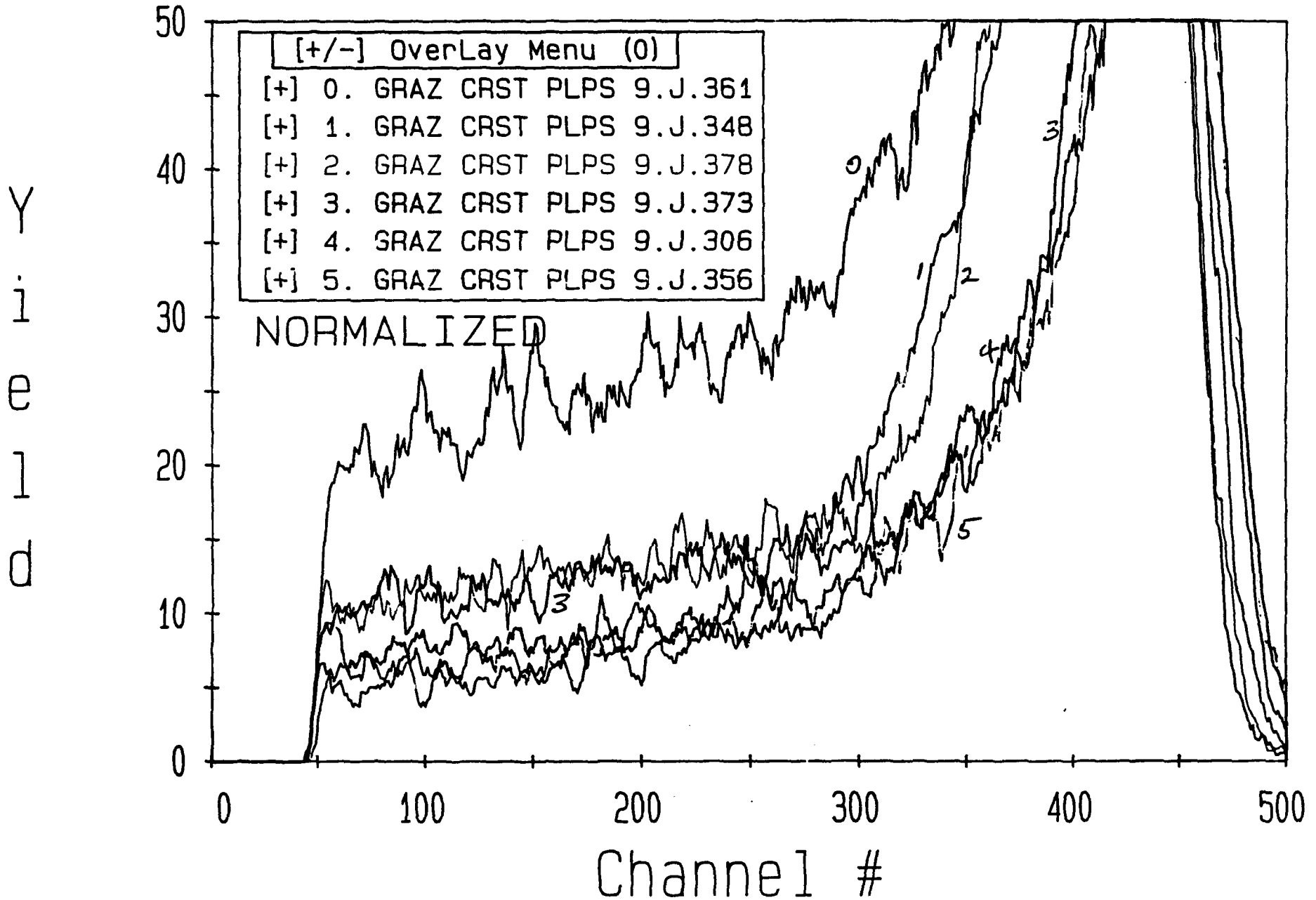
[+/-] OverLay Menu (0)
[+] 0. GRAZ CRST PLPS 9.J.361
[+] 1. GRAZ CRST PLPS 9.J.348
[+] 2. GRAZ CRST PLPS 9.J.378
[+] 3. GRAZ CRST PLPS 9.J.373
[+] 4. GRAZ CRST PLPS 9.J.306
[+] 5. GRAZ CRST PLPS 9.J.356
NORMALIZED
Yield
Channel #
0
10
20
30
40
50
0
100
200
300
400
500

APPENDIX C

SURFACE ROUGHNESS DETERMINATIONS

ZYGO CORPORATION

CRYSTALLUME

Test Report

Five ~~Three~~ Diamond Film Samples

December 10, 1990

ZYGO MEASUREMENT AND TESTING SERVICE
TEST REPORT

December 10, 1990

Objective

To determine the surface roughness of the film samples provided.

Test Plan

EQUIPMENT USED:

A Zygo Maxim-3D Laser interferometric microscope was used to make the measurements on the parts supplied.

The Maxim-3D uses a non-contact method with the wavelength of a laser light source (6328A) as the measurement standard. It incorporates phase measuring interferometry which measures the phase difference between the two wavefronts of the interferometer, a high quality reference surface and the surface of the test piece. A CID (charge-injection device) array camera measures light level changes of the resulting interference wavefront as it is scanned across the detector and the phase is calculated. Repeatability of the Maxim 3-D is better than 0.001 lambda or 0.4 uinches.

CONDITIONS:

The parts were thermally stabilized at room temperature for 24 hours before testing and were tested as received. Room temperature was 71° F during the test. Humidity was maintained at 27%.

PROCEDURE:

The following were done in addition to our standard testing procedures:

1. Due to the information required, the following objectives were used:

   - 1X Fizeau - This has a maximum field of view of 6.9 mm and a lateral resolution (the smallest feature that can be resolved) of 19.3 umeters.

   - 20X Mirau - This has a maximum field of view of 480 um and a lateral resolution of 0.96 um.

- 40X Mirau - This has a maximum field of view of 245 um and a lateral resolution of 0.77 um.

- 100X Mirau - This has a maximum field of view of 95 um and a lateral resolution of 0.48 um.

2. The parts were identified as 9-J-381, ZZ, A242, A243 and 9-J-378.

3. Two sets of measurements were made on each part, one set at the center and one set approximately 16 mm from the center.

4. Color printouts of the test results were made showing a filled plot, a 3-D plot, and a profile plot of each part. Along with the plots, values for the following were determined:

   Peak to Valley (P-V) - This is the absolute value sum of the highest and lowest points of a surface relative to the best fit of a plane. In this application, it is the measure of the part's flatness.

   RMS - This is the root-mean-square deviation from a best fit surface (plane) through the data.

   Rz - This is the average absolute value of the 5 highest peaks and the 5 lowest valleys.

5. A known reference was measured to ensure calibration of the system.

RESULTS:

Printouts for the part showing the RMS, P-V and Ra all in terms of nanometers are attached.

Along with the data, the printouts have:

- An intensity display. This is a single frame of the interference pattern. It serves as a reference of the actual sample image without the need of a separate video monitor print.

FIGURE 1

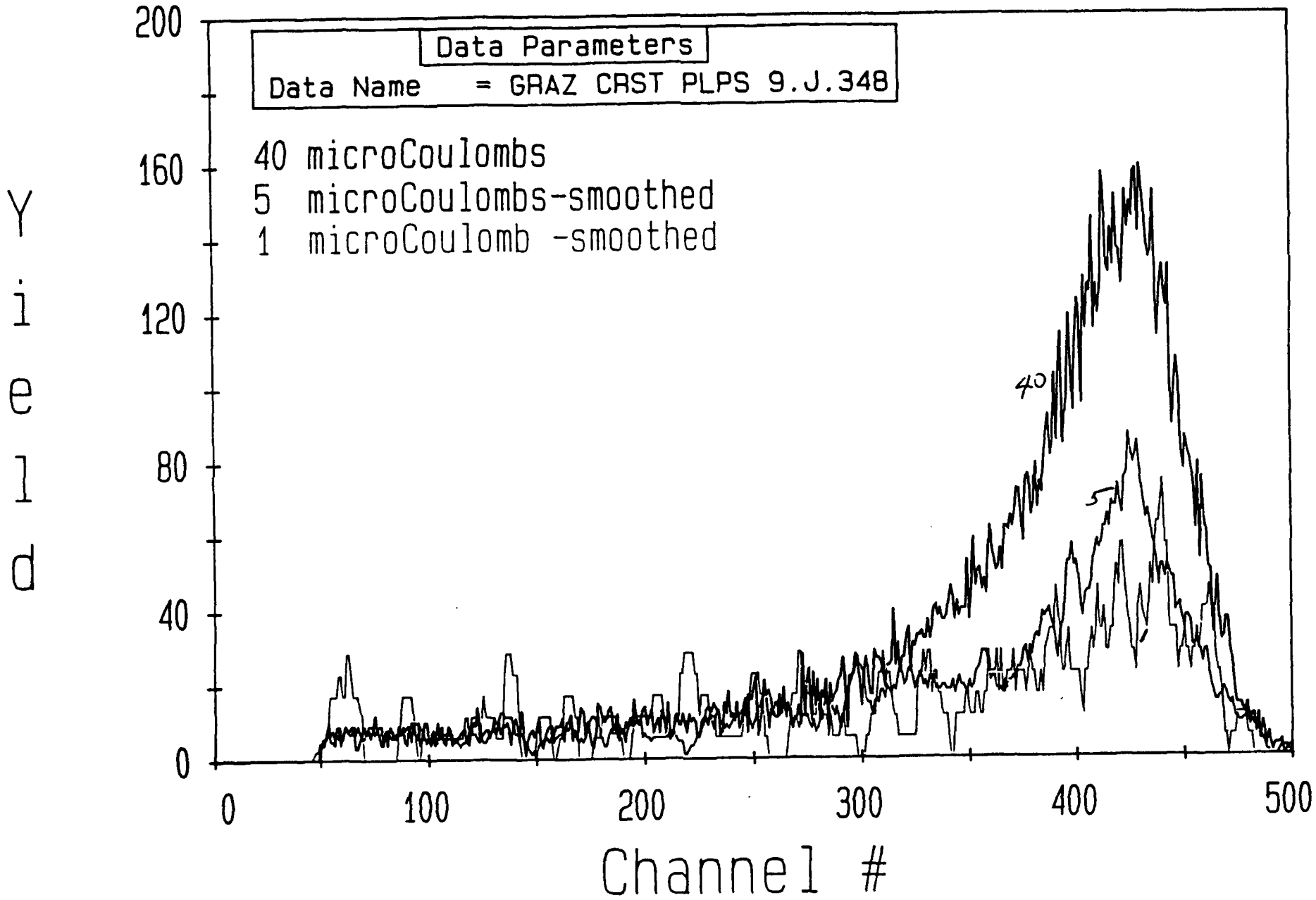
Data Parameters
Data Name = GRAZ CRST PLPS 9.J.348
40 microCoulombs
5 microCoulombs-smoothed
1 microCoulomb -smoothed
40
5
1
Yield
200
160
120
80
40
0
0
100
200
300
400
500
Channel #

- A filled plot. This is color contour plot of the surface.

- A linear profile. The profile is shown as a colored line through the filled plot. Linear profiles can be provided in any orientation. The one that was chosen was done so to show some surface features that looked interesting.

- A 3D plot.

The following summarizes our results:

Part	Location	Ra (20X)	Ra (40X)	Ra (100X)
9-J-381	Center	19.8A	77.3A	78.7A
	16 mm from center	19.2A	22.7A	25.8A
A242	Center	23.0A	21.9A	29.0A
	16 mm from center	53.0A	23.3A	21.8A
ZZ	Center	54.7A	23.2A	30.1A
	16 mm from center	28.9A	25.7A	30 6A
A243	Center	79.6A	36.6A	19.8A
	16 mm from center	16.5A	18.8A	36.0A
9-J-378	Center	26.6A	41.9A	
	16 mm from center	32.9A	ɔ.7A	22.7A

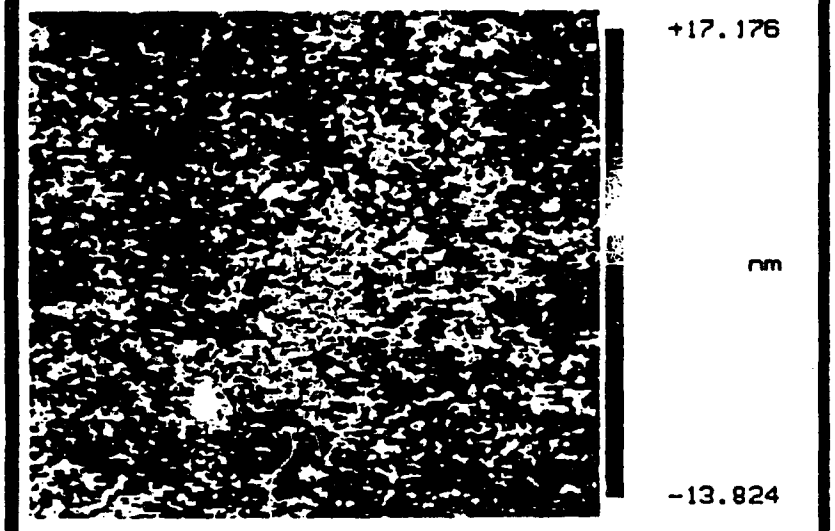

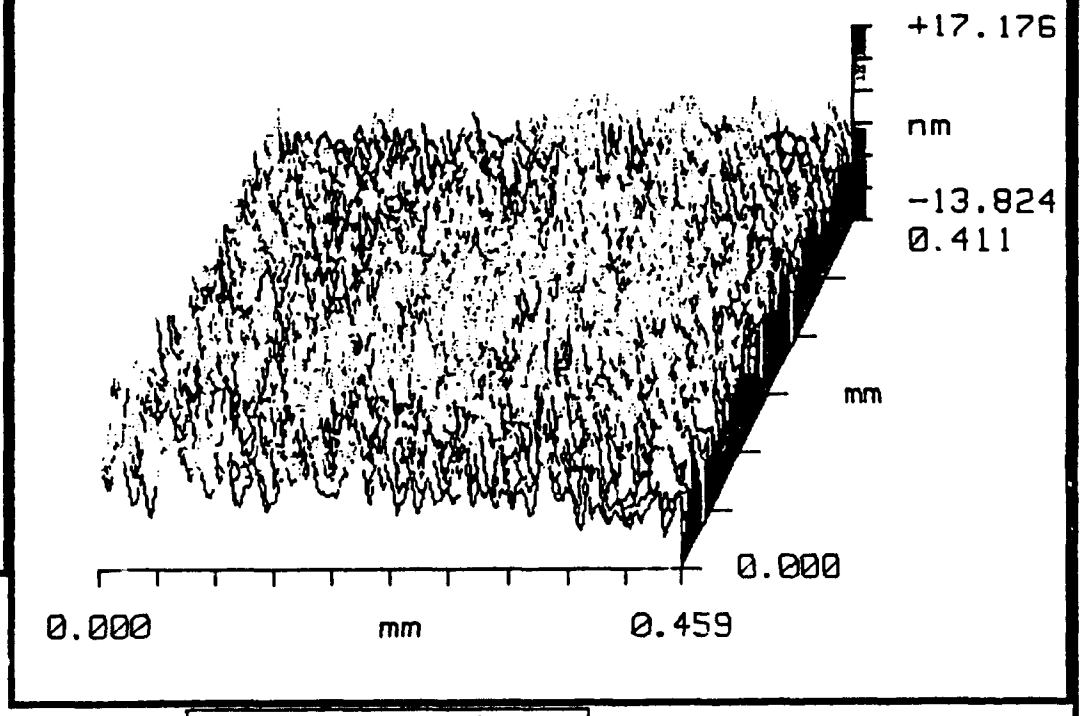

PV	309.9992	A
rms	33.7788	A
Ra	26.6896	A

Removed: Plane

zygo 2D Profile

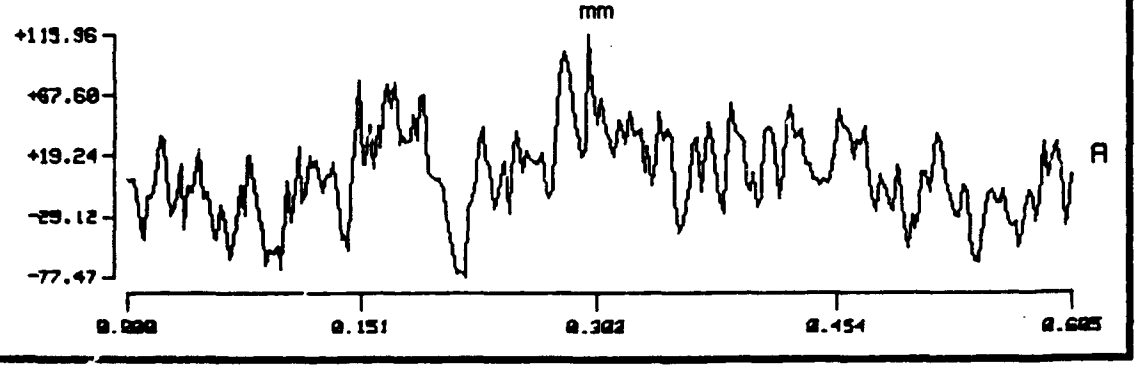

PV	193.4387	A
Rz	140.6682	A

rms	34.69	A
Ra	27.66	A

zygo Intensity Map

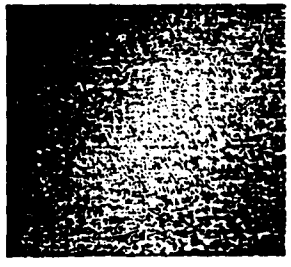

Time Fri Dec 7 16:51:05 1990

P/N: 9-J-378

CRYSTALLUME near center

Objective 20X Mirau

zygo

Maxim-3D Surface Data

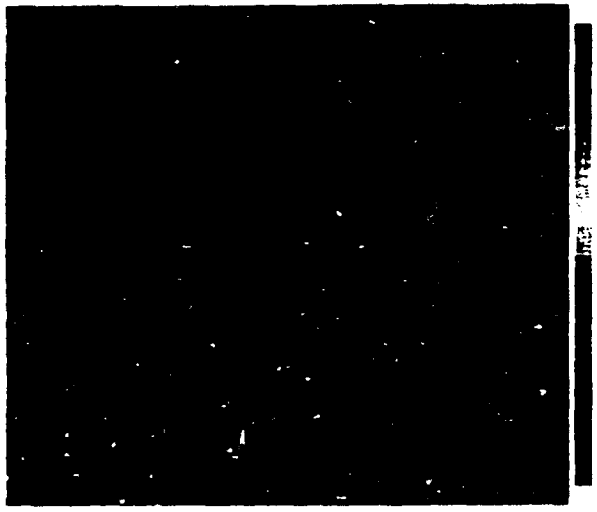

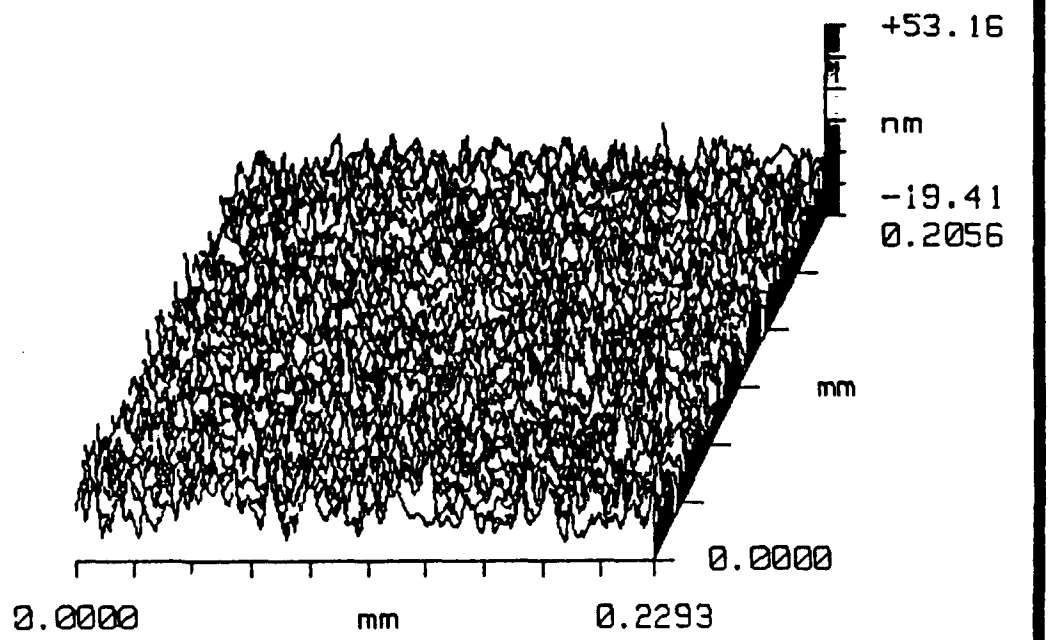

PV	725.6160	A
rms	52.8205	A
Ra	41.9061	A

Removed: Plane

zygo

2D Profile

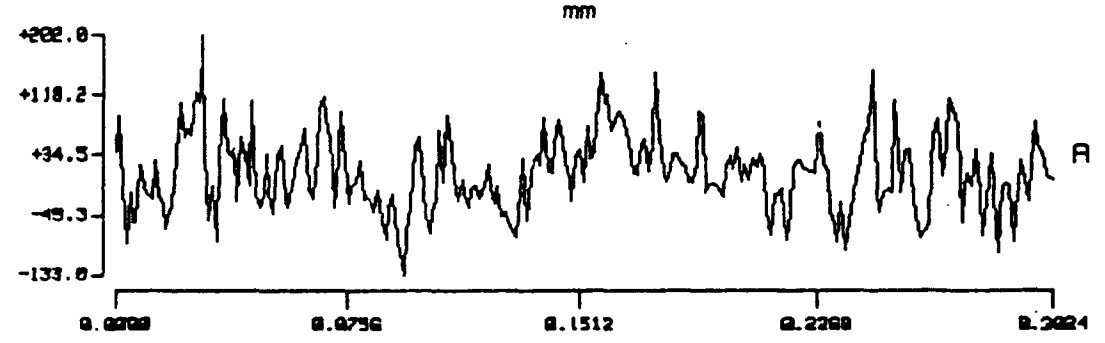

PV	334.9777	A
Rz	255.9173	A

rms	54.01	A
Ra	42.99	A

zygo

Intensity Map

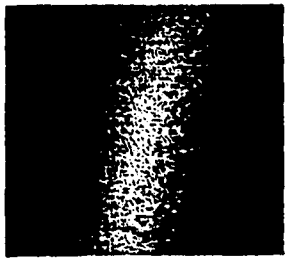

Time Fri Dec 7 16:46:50 1990

P/N: 9-J-378

CRYSTALLUME near center

Objective 40X Mirau

zygo Maxim-3D Surface Data

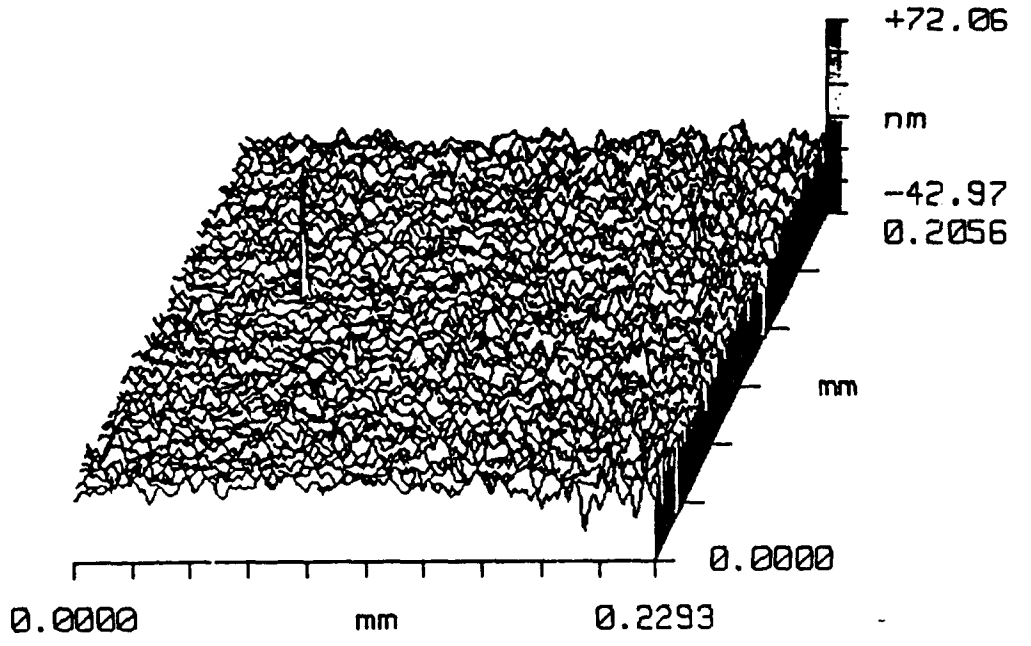

PV	1150.3198	A
rms	45.5900	A
Ra	35.7519	A

Removed: Plane

zygo 2D Profile

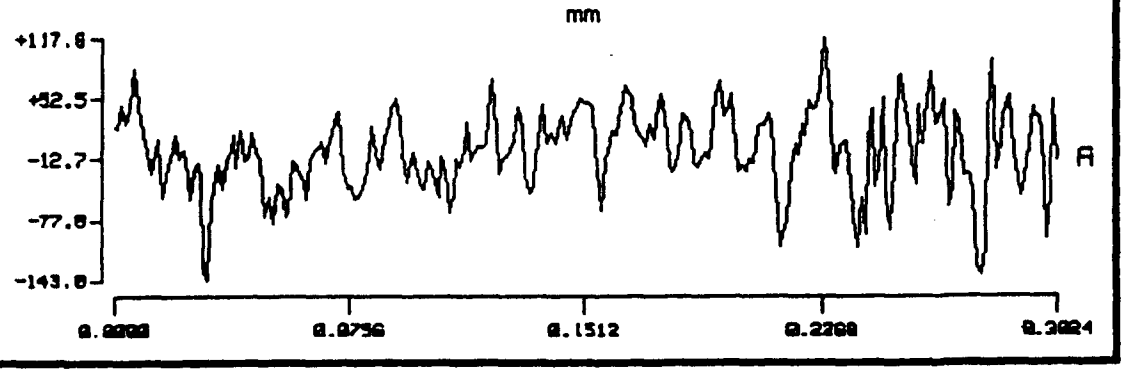

zygo Intensity Map

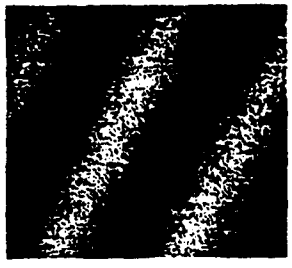

PV	260.5607	A	rms	43.46	A
Rz	208.9352	A	Ra	34.28	A

Time Fri Dec 7 17:01:22 1990

P/N: 9-J-378

CRYSTALLUME 16mm radius

Objective 40X Mirau

zygo

Maxim-3D Surface Data

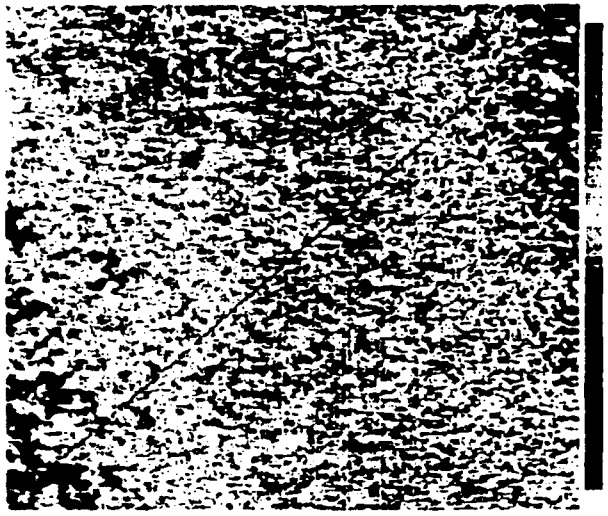

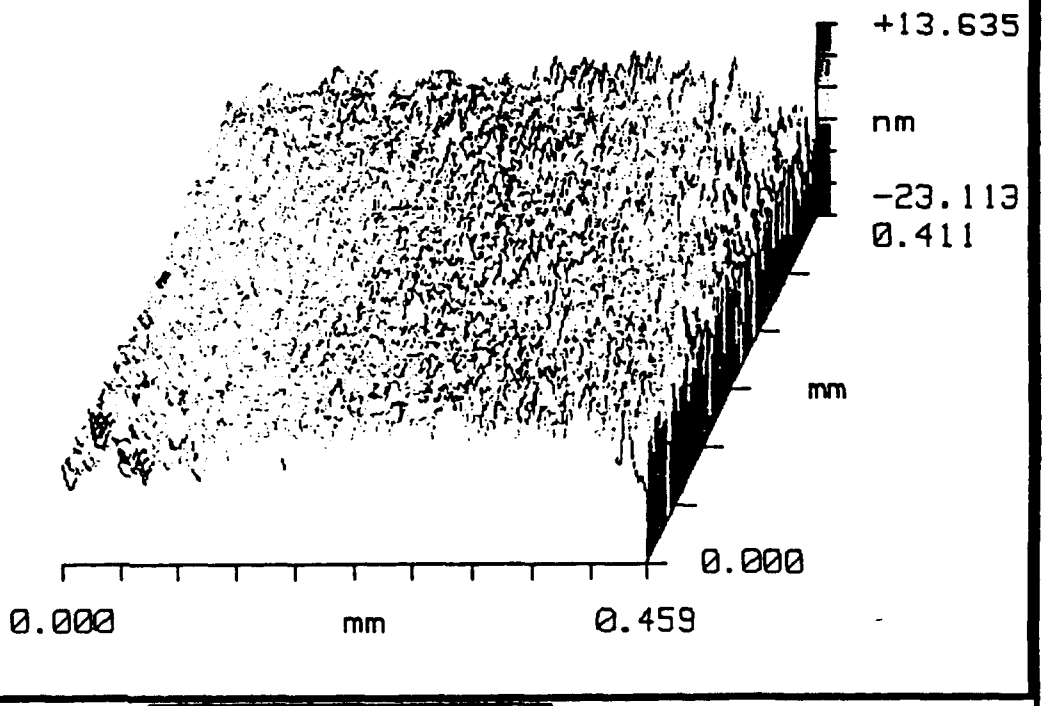

PV	367.4838	A
rms	41.8922	A
Ra	32.9585	A

Removed: Plane

zygo

2D Profile

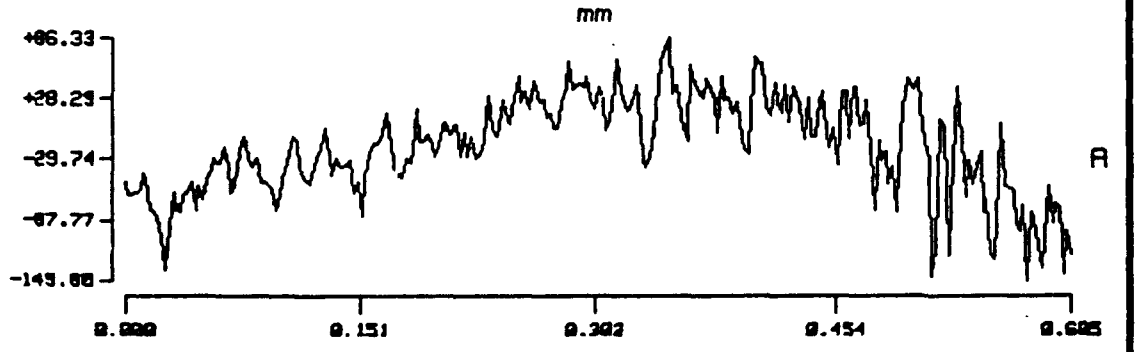

PV	232.1264	A
Rz	196.0842	A

rms	47.08	A
Ra	38.35	A

zygo

Intensity Map

Time Fri Dec 7 17:03:49 1990

P/N: 9-J-378

CRYSTALLUME 16mm radius

Objective 20X Mirau

zygo

Maxim-3D Surface Data

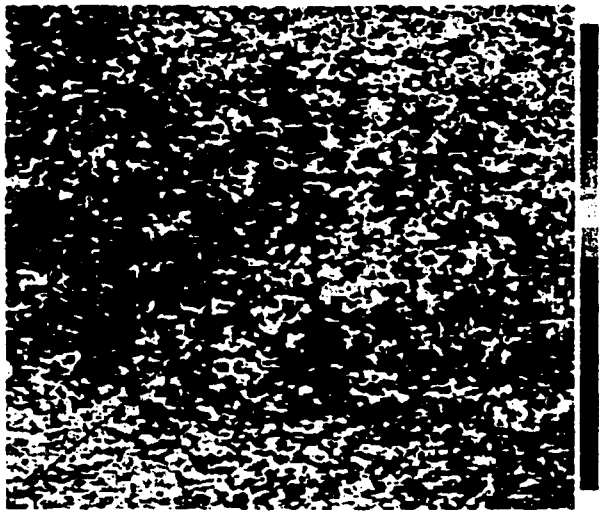

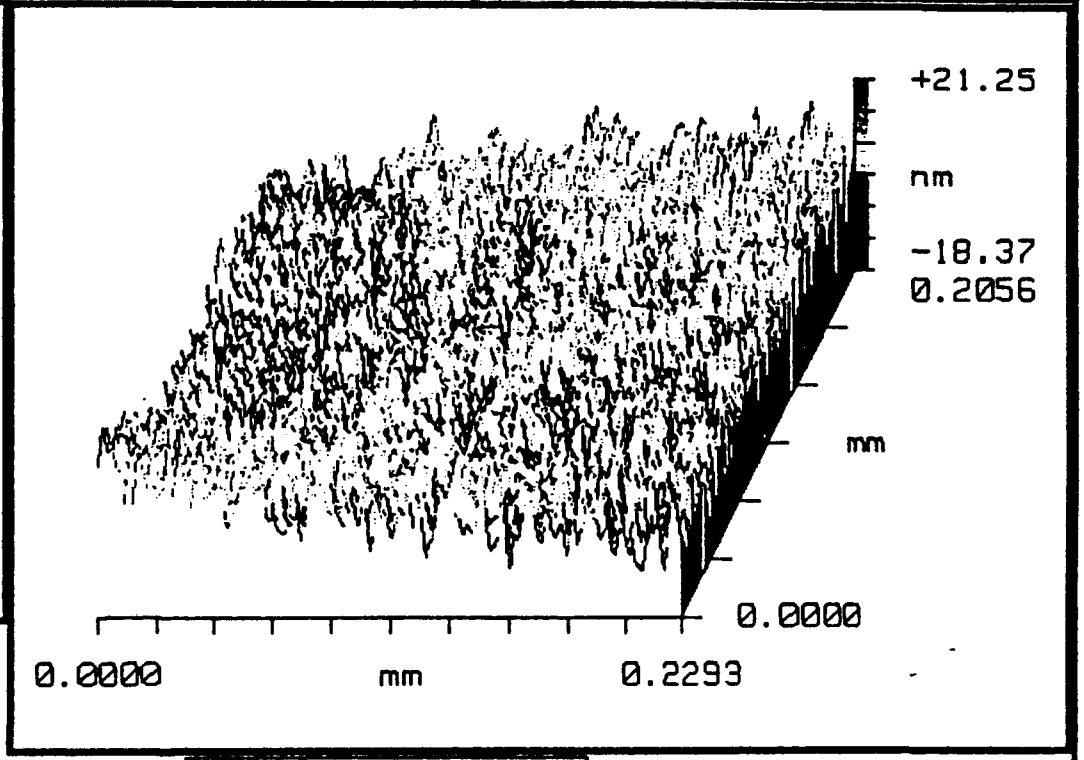

PV	396.2145	A
rms	46.5370	A
Ra	36.6226	A

Removed: Plane

zygo

2D Profile

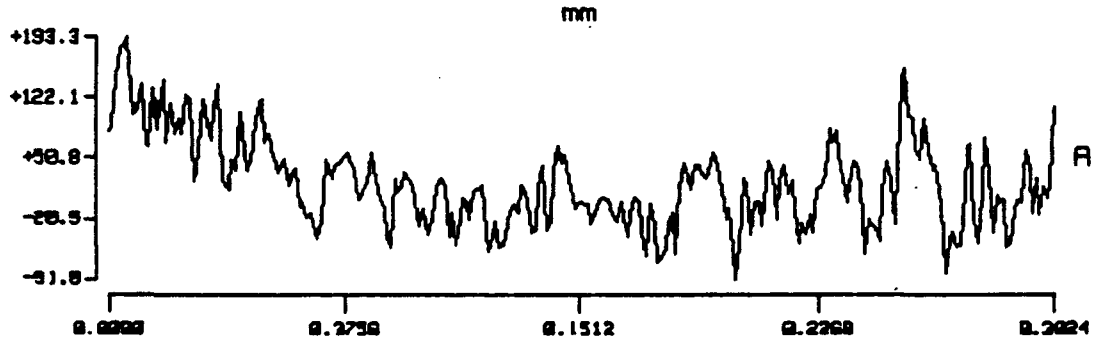

PV	285.0960	A
Rz	206.7047	A

rms	52.90	A
Ra	41.27	A

zygo

Intensity Map

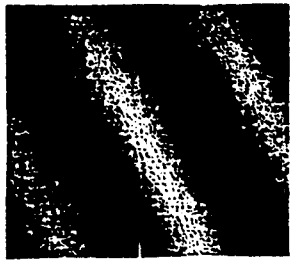

Time Fri Dec 7 16:26:54 1990

P/N: A243

CRYSTALLUME near center

Objective 40X Mirau

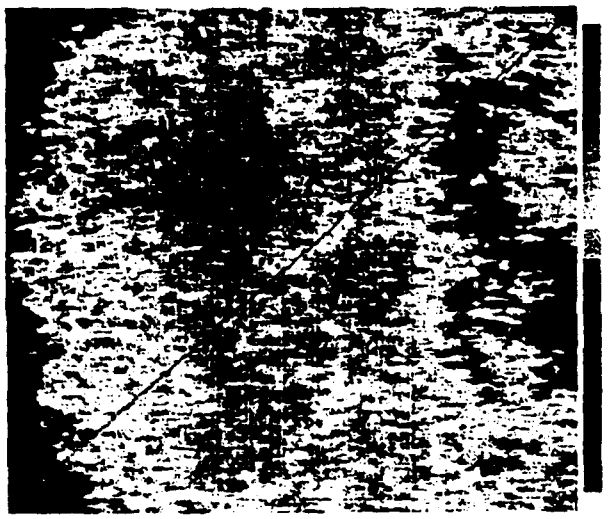

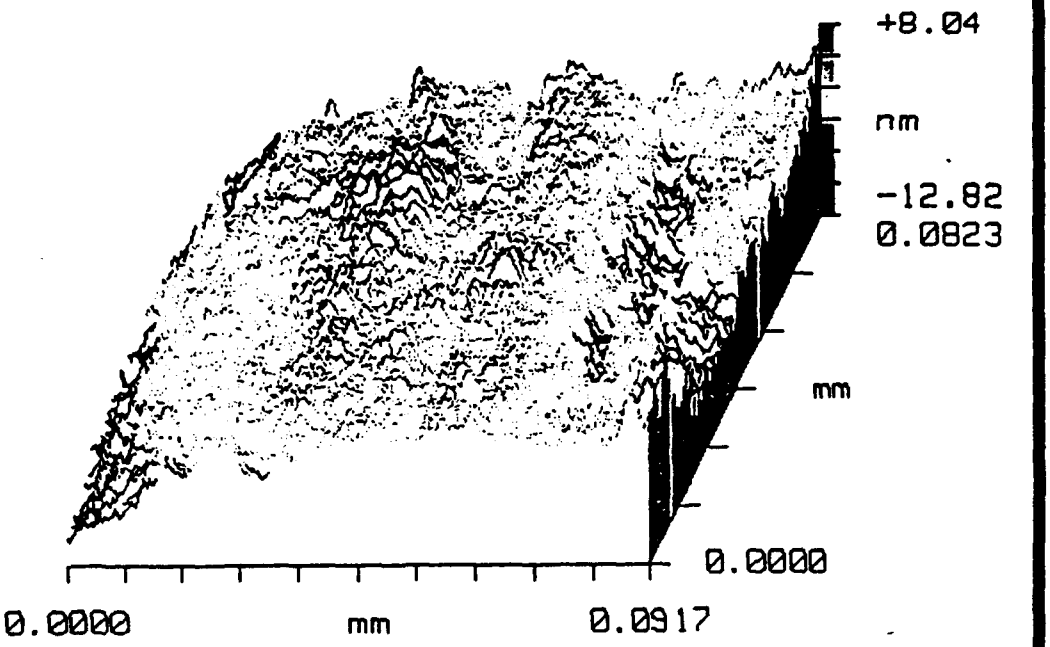

PV	208.6600	A
rms	28.7288	A
Ra	22.7830	A

Removed: Plane

zygo 2D Profile

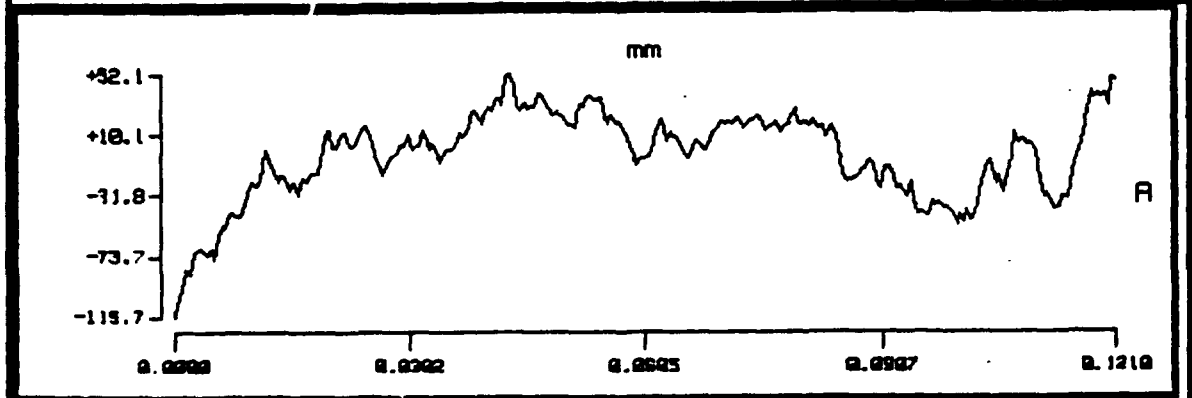

PV	167.7640	A
Rz	84.6841	A

rms	30.09	A
Ra	24.00	A

zygo Intensity Map

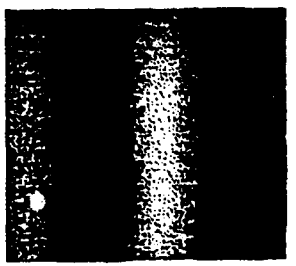

Time Fri Dec 7 16:58:26 1990

P/N: 9-J-378

CRYSTALLUME 16mm radius

Objective 100X Mirau